Technische Universität München
Max-Planck-Institut für Psychiatrie

Manganese-enhanced MRI as an *in vivo* functional imaging tool in mice

Barbara Grünecker

Vollständiger Abdruck der von der Fakultät für Medizin der Technischen Universität München zur Erlangung des akademischen Grades eines

Doctor of Philosophy (Ph.D)

genehmigten Dissertation.

Vorsitzender: Univ.-Prof. Dr. C. Zimmer

Prüfer der Dissertation:

1. apl. Prof. Dr. S. Ziegler
2. Priv.-Doz. Dr. C.T. Wotjak
   Ludwig-Maximilians-Universität München

Die Dissertation wurde am 09.09.2011 bei der Technischen Universität München eingereicht und durch die Fakultät für Medizin am 21.10.2011 angenommen.

Contents

List of Figures

List of Tables

So eine Arbeit wird eigentlich nie fertig, man muss sie für fertig erklären, wenn man nach Zeit und Umständen das Mögliche getan hat.

Johann Wolfgang von Goethe, Italienische Reise, 1787

Abstract

Manganese-enhanced magnetic resonance imaging (MEMRI) is an increasingly used imaging technique in preclinical MR research. The paramagnetic property of the manganese ion (Mn^{2+}) results in improved T_1-weighted tissue contrast. Its chemical similarity to Calcium leads to accumulation of Mn^{2+} in excited neurons and thus allows visualization of neuronal activity *in vivo*. However, at higher concentrations Mn^{2+} exhibits toxic side effects that interfere with the animals' behavior and well-being.

Thus, the first aim of the presented doctoral thesis was to find an experimental protocol for minimizing side effects and intensifying image contrast. This was realized through the application of Mn^{2+} in a fractionated manner. The effects of different fractionated Mn^{2+} application schemes on vegetative, behavioral and endocrine markers have been investigated in C57BL/6N mice, a mouse strain fairly sensitive to Mn^{2+}. An application protocol of 8 injections of 30 mg/kg of $MnCl_2 \cdot 4H_2O$ ($8 \times 30/24$) was found to balance side effects and satisfying image contrast best of all investigated protocols.

To determine the temporal evolution of the MEMRI-contrast during the application phase and after termination of the $8 \times 30/24$ injection protocol a study with repeated MRI readouts was performed. Knowledge of contrast dynamics is necessary to optimize the timing of the application of physiological and psychological stressors in functional MEMRI experiments. Furthermore, in longitudinal studies sufficient time needs to be considered between succes-

sive Mn^{2+}-applications to allow for clearance of Mn^{2+} from the brain.

It was found, that the 8×30/24 injection protocol did not lead to saturation effects without application of a stressor. Mn^{2+} clearance from the brain indicated half-lives of 5.5 to 7.3 days, depending on the brain region. Thus, before performing a second measurement session in the same animals, a delay of at least 8 weeks should be considered to ensure total clearance of Mn^{2+} from the brain.

To examine the feasibility of fractionated MEMRI as functional imaging tool a mouse model of extremes in trait anxiety was treated with fractionated Mn^{2+} injections. The mouse model consists of animals bred for either high, normal, or low anxiety-related behavior (HAB, NAB, LAB respectively). A hypothesis-free whole brain approach identified the hyper-activation of an anxiety-related brain network in HAB animals under basal conditions as compared to LAB animals, with NAB animals showing intermediate activation. Results could be verified by histological staining for Cytochrome-oxidase activity, providing first evidence that trait anxiety activity can be reliably detected *in vivo* using MEMRI.

In conclusion, the accomplishment of these experiments add to todays knowledge of Mn^{2+} toxicity and temporal development of MEMRI contrast in the brain and thus contribute to the optimization of MEMRI applications. Further, this work provides a robust MEMRI method for *in vivo* quantification of trait specific alterations of the neurocircuitry of anxiety.

As longitudinal studies become possible neuronal activation patterns of trait anxiety can be modulated pharmacologically or psychologically and their alterations after the intervention can be assessed *in vivo*. The MEMRI method can readily be applied to other traits and diseases and thus opens up a great number of opportunities for future research in the living animal.

Zusammenfassung

Mangan-verstärkte Magnetresonanztomographie (MEMRI) ist eine Bildgebungsmethode, die in präklinischer MR-Forschung zunehmend Verwendung findet. MEMRI macht sich die paramagnetischen Eigenschaften des Mangan-Ions (Mn^{2+}) zu nutze, um den T_1-gewichteten Gewebekontrast zu verbessern. Die chemische Ähnlichkeit von Mn^{2+} zu Kalzium führt zu Anreicherung von Mn^{2+} in erregten Nervenzellen und erlaubt daher die Visualisierung neuronaler Aktivität *in vivo*. Die Verabreichung hoher Dosen von Mn^{2+} führt jedoch zu toxischen Nebenwirkungen, die sich negativ auf das Wohlergehen der Labortiere auswirken.

Daher bestand das erste Ziel der vorgelegten Dissertation darin, ein experimentelles Injektionsprotokoll zu finden, das sowohl Nebenwirkungen minimiert als auch den Bildkontrast verstärkt. Dies wurde durch die Einführung einer fraktionierten Mn^{2+}-Gabe verwirklicht. Untersucht wurden die Auswirkungen verschiedener fraktionierter Applikationsprotokolle auf physiologische, endokrine und verhaltensbedingte Parameter in C57BL/6 Mäusen, ein Mauslinie, die besonders sensitiv auf Mn^{2+} reagiert. Die fraktionierte Gabe von 30 mg/kg $MnCl_2{\cdot}4H_2O$ über 8 Tage ($8 \times 30/24$) stellte sich hierbei als das Injektionsprotokoll heraus, das von allen untersuchten Injektionsprotokollen toxische Nebenwirkungen und zufriedenstellenden Bildkontrast am besten in Einklang brachte.

Um die zeitliche Entwicklung des MEMRI-Kontrastes während der App-

likationsphase und nach der Beendigung des $8 \times 30/24$ Injektionsprotokolls zu bestimmen, wurde eine Studie mit wiederholten Messungen durchgeführt. Die Kenntnis der Kontrastdynamik ist notwendig, um die zeitliche Taktung zwischen Injektion und Anwendung eines Stressors in funktionellen MEMRI Experimenten zu optimieren. Außerdem muss bei longitudinalen Experimenten ausreichend Zeit zwischen aufeinanderfolgenden Mn^{2+} Applikationen eingerechnet werden, um vorherigen Abtransport von Mn^{2+} aus dem Gehirn zu ermöglichen.

Das Injektionsprotokoll führte nicht zur Sättigung. Weiterhin wurden Halbwertszeiten von 5.5 bis 7.3 Tagen, abhängig von der gemessenen Gehirnregion, bestimmt. Daher sollte vor nochmaliger Mn^{2+}-Gabe in longitudinalen Studien ein Zeitraum von acht Wochen eingehalten werden, um sicher zu gehen, dass das gesamte Mangan aus dem Gehirn abtransportiert wurde.

Um die Anwendbarkeit von MEMRI als funktionelles Bildgebungsverfahren zu untersuchen, wurde ein Mausmodell dispositioneller Ängslichkeit mit fraktionierter Mn^{2+}-Gabe behandelt. Dieses Mausmodell besteht aus Tieren, die selektiv auf hohes, normales sowie niedriges Angstverhalten (HAB, NAB bzw. LAB) gezüchtet wurden. Es wurde eine hypothesenfreie Analyse durchgeführt, die das gesamte Gehirn auf statistisch signifikante Unterschiede in Gehirnaktivierung, gemessen durch Signalintensitäten, untersuchte. Dabei wurde eine Hyperaktivierung von Gehirnregionen in HAB Mäusen unter basalen Bedingungen im Vergleich zu LAB Mäusen identifiziert, die dem Ängstlichkeitsnetzwerk zuzuordnen sind. NAB Mäuse zeigten dabei ausschließlich intermediäre Aktivierungen. Die Ergebnisse konnten mit einer unabhängigen, histologischen, funktionellen Färbungsmethode (Cytochrome-Oxidase Aktivität) verifiziert werden. Die Studie liefert erste Hinweise, dass Unterschiede der Gehirnaktivität dispositioneller Ängstlichkeit *in vivo* mit MEMRI zuverlässig nachgewiesen werden kann.

Die in dieser Arbeit durchgeführten Experimente leisten einen Beitrag zum heutigen Kenntnisstand über Mn^{2+} Toxizität wie auch der temporalen Entwicklung des MEMRI Kontrates und können daher zur Optimierung von MEMRI Applikationen beitragen. Weiterhin konnte diese Arbeit zeigen, dass MEMRI eine robuste Methode zur *in vivo* Quantifizierung dispositioneller Änderungen des Ängstlichkeitsnetzwerkes ist.

Da die Durchführung longitudinaler Studien durch MEMRI ermöglicht wird, können neuronale Aktivitätsmuster dispositioneller Ängstlichkeit pharmakologisch oder psychologisch moduliert und *in vivo* ausgelesen werden. Dies erlaubt weiterhin die *in vivo* Untersuchung der Beiträge bestimmter Gehirnregionen zur Disposition Ängstlichkeit. Die MEMRI Methode kann leicht auf andere Dispositionen und Krankheitsmuster angewendet werden, und eröffnet daher eine große Anzahl von Möglichkeiten für zukünftige Forschung im lebenden Tier.

List of abbreviations

γ	gyromagnetic ratio
$\hbar$	Planck's constant
ω_0	Larmor frequency
%TOA	percentage of time spent on the open arm of the EPM
ANOVA	Analysis of variance
AVP	arginine vasopressin
BBB	blood-brain barrier
BLA	basolateral amygdala
BNST	bed nucleus of the stria terminalis
BNST vGP	bed nucleus of the stria terminalis and ventral pallidum
BOLD	blood oxygen level dependent
BS	brain stem
c+sc	cortical and subcortical
Ca^{2+}	Calcium
CBF	cerebral blood flow

CeA	central nucleus of the amygdala
CI	confidence interval
CN	cerebellar nucleus
CNS	central nervous system
CO	Cytochrome oxidase
COV	coefficient of variation
CP	choroid plexus
CPU	caudate putamen
CrB	cerebellum
CSF	cerebrospinal fluid
d	day
DG	dentate gyrus
dHB	deoxyhemoglobin
EC	entorhinal cortex
EPM	elevated plus maze
FDR	false discovery rate
fMRI	functional MRI
FOV	field of view
FT	Fourier transformation
FWE	family wise error

GEFI	gradient echo fast imaging
GLM	general linear model
Glu	Glutamate
GP	globus pallidus
GRE	gradient echo
h	hour
HAB	high anxiety-related behavior mouse
HPA axis	hypothalamic-pituitary-adrenal axis
HPC	hippocampus
HTh	Hypothalamus
IC	inferior colliculi
ip	intraperitoneal
LAB	low anxiety-related behavior mouse
LSD	least significant difference
MEMRI	manganese enhanced MRI
mM	millimolar
Mn^{2+}	manganese ion
mPFC	medial prefrontal cortex
MRI	magnetic resonance imaging
ms	milliseconds

NAB	normal anxiety-related behavior mouse
Nacc	nucleus accumbens
NMR	nuclear magnetic resonance
NoA	number of averages
OB	olfactory bulb
PAG	periaqueductal gray
PB	parabrachial nucleus
PBS	sodium phosphate buffer
PC	piriform cortex
PVN	paraventricular nucleus of the hypothalamus
RARE	rapid acquisition relaxation enhancement
RF	radiofrequency
RI	relative intensity
ROI	region of interest
RSG	retrosplenial granular cortex
SC	superior colliculi
SE	spin echo
SEM	standard error of the mean
SPM	statistical parametric mapping
sr	spatial resolution

ss	steady state
T	Tesla
T1w	T1 weighted
T2w	T2 weighted
TE	echo time
Th	Thalamus
TR	repetition time
wb	whole brain

Chapter 1

Introduction

The ability of magnetic resonance imaging (MRI) to create images with an outstanding soft tissue contrast render it an important diagnostic tool. Contrary to computed tomography (CT) and positron emission tomography (PET) it does not need ionizing radiation. Not only in clinical, but also in preclinical imaging, MRI is becoming more and more important due to the ability to perform longitudinal *in vivo* studies in the same animals. Especially the use of manganese ions (Mn^{2+}) as a paramagnetic contrast agent is becoming increasingly popular in MRI of the rodent brain as the low native contrast between different cerebral compartments hampers the delineation of cortical and subcortical regions. Furthermore, the difficulty of functional imaging in rodents lies in the need for anesthesia which alters oxygen levels in the blood and restricts the paradigms that can be applied. Manganese enhanced MRI (MEMRI) can be used as a functional imaging tool, which is independent of oxygen levels in the blood and, therefore, of anesthetic effects. However, at high concentrations Mn^{2+} exhibits toxic side effects that interfere with the animals' behavior and well-being. Therefore, it is necessary to find a balance between toxic side effects and satisfactory MRI contrast. In this work different MRI application protocols, the dynamics of Mn^{2+} accumulation in different brain structures as well as clearance from the brain and the application of

MEMRI in a mouse model of extremes in trait anxiety were investigated.

The following part of the introduction will explain all topics necessary to understand the performed experiments and their outcomes. First, the principles behind MRI will be explained, followed by a section about MRI data analysis. Furthermore, to understand the role of the chemical element manganese in the body and as MRI contrast agent will follow. Then, the possible applications of MEMRI derived from the properties of manganese will be explained. The last introductory part will give a short overview of anxiety disorders and mainly the mouse model of extremes in trait anxiety, which was used in one of the performed studies, as well as current knowledge of the neurocircuitry of anxiety. Chapter 2 will describe the methods used in this work and the experiments performed. The results of the experiments will be presented in chapter 3 and finally discussed in chapter 4. Chapter 5 will contain a summary, concluding remarks and future prospects.

1.1 MRI

1.1.1 History of MRI

The first successful nuclear magnetic resonance (NMR) experiment was conducted in 1946 by Felix Bloch and Edward Purcell, independent from one another. They found that certain nuclei, when placed into a magnetic field, absorb energy in the radio frequency range of the electromagnetic spectrum. The nuclei re-emit this energy when they transfer back to their original state. The frequency of the emitted energy is proportional to the magnetic field (Larmor frequency) [1, 2]. Furthermore, they developed instruments that were able to measure magnetic resonance in bulk material e.g. solids and liquids. Both were rewarded with the Nobel Prize for physics in 1952. A few years later Raymond Damadian (State University of New York) demon-

strated that T_1-relaxation times differ between normal and abnormal tissue (e.g. healthy tissue and cancerous tissue) as well as between different tissue types [3]. This finding was crucial for leading to the use of NMR as a medical imaging technique. In 1973 Paul Lauterbur invented an imaging technique that he named 'Zeugmatography'. Zeugmatography joined the external magnetic field with a magnetic gradient field enabling the spatial localization of two test tubes of water [4]. For image reconstruction he used a back projection method. This expanded the use of one dimensional MR spectroscopy to the second dimension and became the foundation of MR imaging. In the same year Sir Peter Mansfield further developed the use of gradient fields and the mathematical analysis of signals to a more useful technique. Both Lauterbur and Mansfield were rewarded with the Nobel Prize for medicine in 2003 for their contribution to the development of MRI. In 1975 Richard Ernst replaced Lauterbur's back projection method by the introduction of a phase encoding step by timely switching magnetic gradient fields (section 1.1.2.8) [5]. This image reconstruction method provides the basis of current MRI techniques.

1.1.2 Physical principles of MRI

1.1.2.1 Nuclear spin and magnetic moment

Many atomic nuclei possess a property called nuclear spin. One consequence of this property is a magnetic moment which is aligned along the axis of the spin. The spin is a quantized property and is characterized by the spin quantum number I, which is either integer or half integer. Spin is a type of angular momentum which is quantum-mechanically defined as:

$$p = \hbar I \tag{1.1}$$

where $\hbar$ is Planck's constant. The already mentioned magnetic moment is related to the angular momentum through a proportionality constant γ:

$$\mu = \gamma p \tag{1.2}$$

γ is called the gyromagnetic ratio and is a nucleus dependent constant. The hydrogen proton is most commonly used for MRI, as it possesses the highest value of γ [6] and is the most abundant proton in the human body (water content: $\sim$60%)[7].

The physical principles of MRI are based on the behavior of the spins of the hydrogen protons in an externally applied magnetic field B_0. The interaction of the hydrogen proton with B_0 results in a precession of the proton spin around the magnetic field direction (figure 1.1).

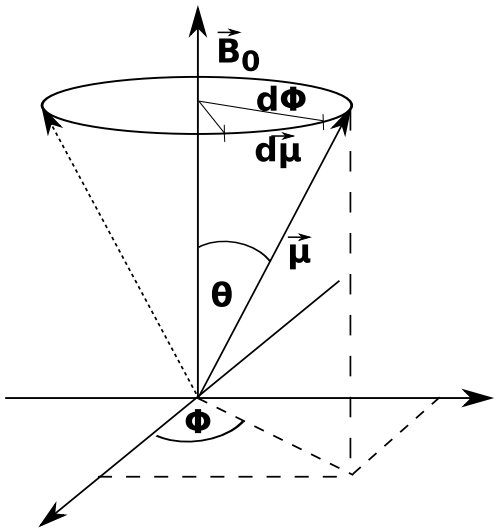

Figure 1.1: Precession. Precession of the magnetic moment vector $\vec{\mu}$ around the axis of an externally applied static magnetic field B_0 with the angle θ.

1.1.2.2 The formation of bulk magnetization in a magnetic field

Upon the application of B_0 the proton spins will attempt to align in the direction of the magnetic field. Quantum mechanically a proton with only

two quantum spin states has two possible alignments: parallel (spin quantum number m=1/2) or antiparallel (spin quantum number m=-1/2) to the field. Parallel alignment thereby corresponds to the low energy state and antiparallel alignment to the high energy state (figure 1.2). The energy difference ΔE between the two states is determined by the frequency of radiation required to induce transitions between the two states, which is $\Delta E = \hbar f = \hbar\gamma B_0$ [8].

The spins of a large number of nuclei in a sample will randomly align parallel or antiparallel to the direction of the field. However, the low energy state will be slightly favored. The spin excess in favor of parallel alignment can be calculated due to Boltzmann's equation:

$$\frac{N_{m=1/2}}{N_{m=-1/2}} = exp(-\frac{\gamma\hbar B_0}{kT}) \tag{1.3}$$

where k is Boltzmann's constant and T the temperature of the sample. kT then designates the thermal energy in the system. At room temperature and a magnetic field of 1 Tesla (T) parallel alignment predominates by only 7 parts per million. M_0, the longitudinal equilibrium magnetization is given by:

$$M_0 = \frac{\rho_0\gamma^2\hbar^2}{4kT}B_0 \tag{1.4}$$

with ρ_0 defined as number of protons per unit volume (spin density). This value gives measurable NMR signal at equilibrium [8].

1.1.2.3 Larmor frequency

The frequency at which transitions between the low and high energy state can be induced is known as the Larmor frequency. For a spin-1/2 system it can be derived from classical mechanics. When a classical spin is not aligned with the field a torque is applied. The spin, therefore, will move at right angles to the torque, which will induce a movement known as precession. The angular

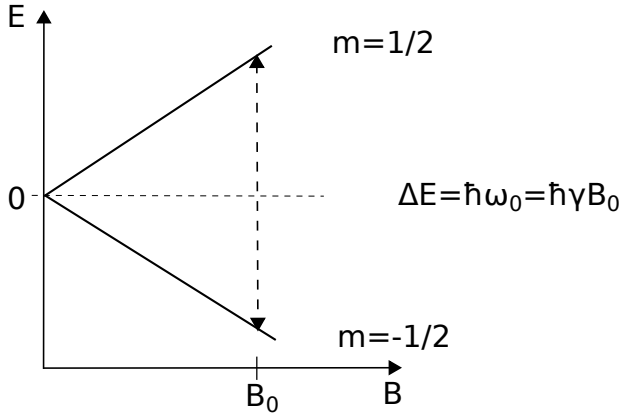

Figure 1.2: Possible energy states. A system with two possible quantum spin states (m=1/2, m=-1/2). Upon the irradiation of ΔE the spin changes from the low into the high energy state.

frequency of this precession is described by:

$$\omega = 2\pi f = \mu B/p = \gamma B \tag{1.5}$$

With an externally applied magnetic field B_0 the angular frequency becomes the Larmor frequency:

$$\omega_0 = -\gamma B_0 \tag{1.6}$$

ω_0 depends on the strength of the applied magnetic field and the gyromagnetic ratio γ. The minus sign in equation 1.6 means, that the Magnetization rotates clockwise, with time, in negative Φ-direction (figure 1.1). As mentioned before, the value of γ depends on the nucleus [6]. For the proton it is found to be 42.58 MHz. For a magnetic field of 7 Tesla the Larmor frequency is around 300 MHz.

1.1.2.4 The equation of motion

The equation of motion of the magnetization in a magnetic field B_0 is given by:

$$\frac{d\overrightarrow{\mathrm{M}}}{dt} = \gamma \overrightarrow{\mu} \times \overrightarrow{B_0} \tag{1.7}$$

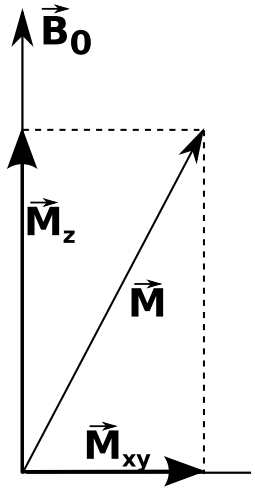

Figure 1.3: Magnetization. The magnetization vector can be split into two components, the longitudinal part M_z and the transversal part M_{xy}. In the equilibrium state M_{xy} is zero while M_z takes maximum value.

where both M and B_0 are treated as three dimensional vectors. This equation means that the spin will always move perpendicular to both its own and the magnetic field axis. This equation is a simple representation of the famous Bloch equation [9].

1.1.2.5 Detection of the magnetization of the system

In order to evoke a measurable signal the magnetization has to be tipped away from its equilibrium state. This is usually achieved by applying a radio frequency (RF) magnetic field B_1 for a short time at Larmor frequency. This so called RF pulse is produced by a transmit coil and causes a precession of M_0. The now emerging transversal magnetization M_{xy} (figure 1.3), which is 0 in the equilibrium state, precesses around the B_0 axis and this movement induces alternating voltage in nearby receiver coils. The alternating signal is called the free induction decay [8].

Consider a magnetization that has been tipped into the x-y-plane by a 90° angle ($\pi/2$-pulse). Right after the pulse the transverse magnetization has

a magnitude of $M_{xy} = M_0$. It starts to precess in the x-y-plane. Due to interactions of the spins with surrounding spins and the surrounding tissue the magnetization loses phase coherence and relaxes back to its equilibrium state [8].

1.1.2.6 Relaxation processes

The magnetization will eventually go back to its equilibrium state with initial magnitude M_0 due to different relaxation processes. These relaxation processes are mainly characterized by two different processes called T_1- and T_2-relaxation:

- The T_1-relaxation arises due to the interaction of the spin system with its surrounding and is also known as longitudinal or spin-lattice relaxation. The interactions with the molecular environment denotes an energy loss to the system, which is reflected by M_z, the longitudinal magnetization. Once out of equilibrium, M_z will exponentially grow back to its former strength M_0 with the time constant T_1 [6].
- T_2-relaxation is known as transverse or spin-spin relaxation. In this process the spin system does not lose energy but exchanges it among itself. The energy exchange results in a loss of phase coherence of the spins in the motion of precession and leads to a decay in the transverse magnetization M_{xy}. Transverse relaxation, however, is limited by the spin-lattice relaxation meaning that T_2 can never exceed T_1 [6].

Taking these two relaxation processes into account equation 1.7 becomes:

$$dM_x/dt = \gamma(M_y B_z - M_z B_y) - M_x/T_2 \tag{1.8}$$

$$dM_y/dt = \gamma(M_z B_x - M_x B_z) - M_y/T_2 \tag{1.9}$$

$$dM_z/dt = \gamma(M_x B_y - M_y B_x) - (M_z - M_0)/T_1 \tag{1.10}$$

These equations are known as the Bloch equations. Solving the equations for a static magnetic field $\overrightarrow{B} = B_0\overrightarrow{z}$ the Bloch equations become:

$$dM_x/dt = \omega_0 M_y - M_x/T_2 \tag{1.11}$$

$$dM_y/dt = -\omega_0 M_x - M_y/T_2 \tag{1.12}$$

$$dM_z/dt = (M_0 - M_z)/T_1 \tag{1.13}$$

Solving this set of differential equation the complete set of solutions is:

$$M_x(t) = exp(-t/T_2)(M_x(0)cos\omega_0 t + M_y(0)sin\omega_0 t) \tag{1.14}$$

$$M_y(t) = exp(-t/T_2)(M_y(0)cos\omega_0 t + M_x(0)sin\omega_0 t) \tag{1.15}$$

$$M_z(t) = M_z(0)exp(-t/T_1) + M_0(1 - exp(-t/T_1)) \tag{1.16}$$

For an initial situation where $M_z(0) = 0$ the regrowth of M_z is given by:

$$M_z(t) = M_0(1 - exp(-t/T_1)) \tag{1.17}$$

The T_2-decay is best explained by an experiment where a $\pi/2$ pulse is applied at a certain interval T_R (repetition time) (section 1.1.2.9). If, due to spin dephasing, all transverse magnetization has decayed away and only the remaining longitudinal magnetization can be turned into the transverse plane at the time of data sampling echo time (T_E) (section 1.1.2.9) the signal is proportional to the magnitude of the transverse magnetization:

$$M_{xy}(T_E) = M_0(1 - exp(-T_R/T_1))exp(-T_E/T_2) \tag{1.18}$$

The factor $\exp(-T_E/T_2)$ is called the spin-spin decay factor and is only dependent on T_2. Additionally, magnetic field inhomogeneities lead to further spin dephasing leading to an additional relaxation time T_2^*. Taking this source of dephasing into account one needs to replace T_2 by the smaller T_2^* in equation

1.18 [10].

1.1.2.7 Tissue contrast

MRI provides excellent soft tissue contrast which is based on three different parameters: the proton-spin density, and the two relaxation times T_1 and T_2 (equations 1.17 and 1.18). By varying the experimental sampling parameters T_R and T_E the images can be manipulated towards a weighting of proton density, T_1 or T_2 [8]. Since only T_1 and T_2 images are acquired in this work, proton density weighting will be neglected.

T_1-weighting

At 7T, T_1-times of different tissue types differ by hundreds of milliseconds. Acquiring T_1-weighted contrast is a powerful tool for the delineation of different tissue types. To obtain T_1-weighted contrast T_2 contributions to the signal have to be minimized. For $T_E << T_2$ the spin-spin decay factor approximates 1 and equation 1.18 becomes $M = M_0(1 - exp(-T_R/T_1))$. This results in:

$$M = M_0(T_R/T_1) \tag{1.19}$$

being independent of T_2 [8].

T_2-weighting

Compared to T_1-values, T_2-values are typically small and in the order of tens of milliseconds. T_2-values provide a sensitive indicator of pathological changes in tissue. To obtain T_2-weighted contrast T_1 contributions to the signal have to be minimized. This is obtained by using $T_R >> T_1$:

$$M = M_0(-T_E/T_2) \tag{1.20}$$

This equation is independent of T_1 and therefore by using long T_R and intermediate T_E one will gain T_2-weighted images [8].

1.1.2.8 From signal to image

For image reconstruction it is necessary to assign spatial locations to the signal measurements from various sources. The three different spatial directions x, y and z are encoded according to different methods. A homogeneous static magnetic field that is applied in z-direction is considered.

Slice selection

The function of the slice-selective RF pulse is the tipping of the magnetization in a particular desired slice [11]. This is achieved by applying a RF pulse that has a shape containing only a narrow band of frequencies centered on one particular frequency ω_0. Additionally, a gradient field is applied to the RF pulse along the slice selection axis (z-axis) to set the resonance frequency at the center of the selected slice to ω_0. The magnetic field gradient leads to a variation in the frequency along the z-axis, meaning that the RF pulse is on-resonance only for a small range of z. However, this means that only spins with a frequency within that narrow range are excited in the slice by the RF pulse [11].

The slice-selection procedure generates a precessing transverse magnetization at each point of the selected slice. The task of spatial encoding is to assign x- and y-positions of each signal such that the signal distribution in the x-y plane can be reconstructed.

Spatial encoding

To achieve spatial encoding within the selected slice two more encoding steps are necessary: frequency and phase encoding. Through the application of a

gradient field in x-direction every spin precesses with a different frequency. This gradient field is usually turned on during data collection. This results in precession frequencies that vary linearly along the x-axis. While this results in transformation from a sum of signals all at the same frequency to a sum of signals covering a whole range of frequencies, the separation of the signals corresponding to each frequency is enabled. By calculating the Fourier transform (FT) of any signal measured a series of amplitudes over time can be converted to a series of amplitudes corresponding to different frequencies ν. Therefore, the measured signal S(t) is easily converted to S(ν) [12].

Frequency encoding only allows for the separation of the sum of signals coming from the x-axis. However, each of these separated signals is still a sum of signals from different y-positions at one x-position. To be able to separate these signals, phase encoding is applied. Phase encoding is closely related to frequency encoding. Between the RF excitation pulse and the data acquisition a gradient field along the y-axis is turned on for a short interval. This y-gradient leads to a different precession rate of the transverse magnetization at different y-positions, resulting in a signal that increases linearly with time. After turning off the y-gradient, spins precess again at the same rate, however, without loosing their phase differences. The phase encoding step leads to a phase offset of each local precessing magnetization proportional to its y-position before frequency encoding and data acquisition is carried out [12]. Thus, application of frequency encoding leads to a further phase evolution of the signal from a voxel with the rate of change of the phase, which is proportional to the x-position. One phase encoding step is finalized by data acquisition. The acquisition of a complete image uses many numbers of phase encoding steps, typically 128 or 256. After each phase encoding step the pulse sequence is repeated with an increase in amplitude of the gradient. This leads to an increase in the phase of the magnetization at position y, resulting in

a phase increase which is proportional to y with each repetition of the pulse sequence.

The imaging process can be summarized as follows: The magnetization vector can be described by its magnitude, which is dependent on the local relaxation times and the parameters of the pulse sequence, as well as the phase angle which defines how much the vector has precessed up to the time of measurement. By applying gradient fields, the precession of the magnetization is either sped up or slowed down depending on its position. Then an image of the magnitudes of the local magnetization is created by frequency and phase encoding.

During this process a data matrix is created in which one line represents the signals measured during one phase encoding step. The sampled data matrix is called k-space as it is made up of different spatial frequencies called k. The final MR image is reconstructed by applying FT to the k-space data matrix [12].

1.1.2.9 Pulse sequences

A pulse sequence in MRI is the sequencing of RF pulses and magnetic field gradients to create measurable signal. Basic timing parameters of these pulse sequences are T_E, which denotes the time point of data sampling, and T_R, denoting the time point after which the pulse sequence is repeated. Choosing these two parameters causes different weighting of images (see section 1.1.2.7). As signal can only be measured when the magnetization is tipped into the transverse plane, every pulse sequence uses at least one excitation pulse. The excitation pulse is implemented by turning on the RF modulation field B_1 for a short amount of time (pulsing). The excitation pulse itself is characterized by the flip angle, meaning the angle between the direction of B_0, the magnetization vector directly after applying the excitation pulse and

	Short T_E ($\leq 20ms$)	Long T_E ($\geq 80ms$)
Short T_R ($< 700ms$)	T_1-weighting	not used
Long T_R ($> 2000ms$)	Proton density-weighted	T_2-weighted

Table 1.1: Possible combinations of T_E and T_R values to generate T_1-, T_2- and proton density weighting [15].

by its shape [13]. Since the variety of existing pulse sequences is very broad only pulse sequences which were used in this work will be explained.

Spin echo pulse sequence

The spin echo (SE) sequence is a fundamental pulse sequence in MRI. The SE is formed by refocusing the dephased spins through a refocusing pulse after excitation. The flip angles of excitation and refocusing pulse are usually set to 90° and 180°, respectively. One of the main advantages of SE imaging is the refocusing of magnetic field inhomogeneities, thus avoiding the loss of signal [14]. Different combinations of T_E and T_R produce specific weighting (table 1.1).

Figure 1.4 shows the development of a spin echo. The acquisition time of a SE pulse sequence is given by:

$$T_{scan} = T_R \times N_{phase} \times NEX \tag{1.21}$$

with N_{phase} denoting the number of phase encoding steps and NEX the number of excitations. For a T_2-weighted image with long T_R (see table 1.1) this results in extremely long scan times. Especially for T_2-weighted images the long acquisition times have led to the increased use of echo-train pulse sequences such as the rapid acquisition relaxation enhancement (RARE) sequence [15]. In this work the RARE sequence was used for acquiring T_2-weighted images. The following paragraph gives a brief overview of the functioning of the RARE sequence.

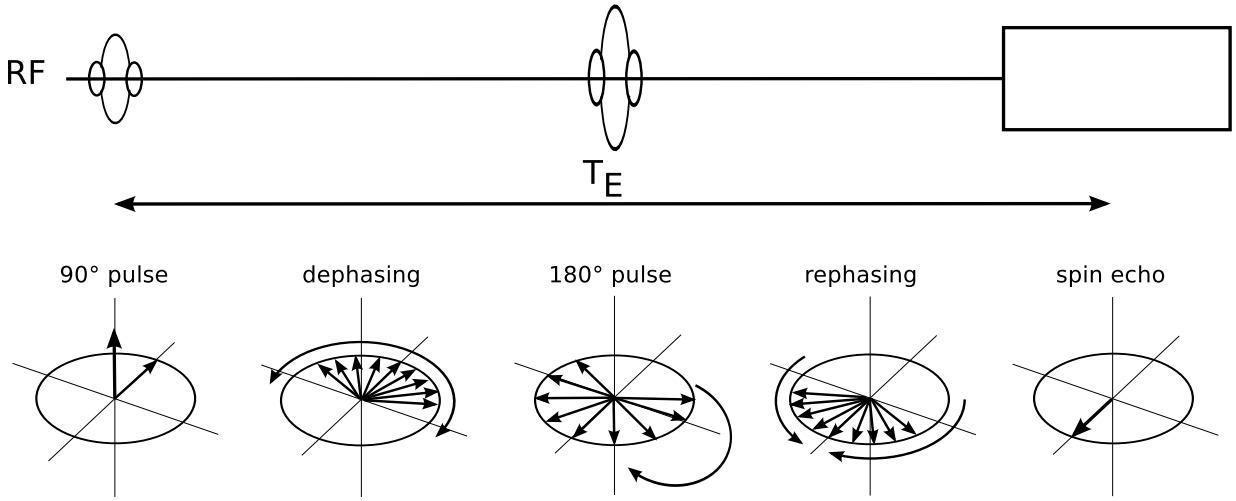

Figure 1.4: Spin echo. Shown is the formation of a spin echo. Magnetization that is tipped into the xy-plane by a 90° pulse begins to dephase. A 180° pulse turns the spins about the y-axis, where they rephase. After the time T_E spins are in phase and create the spin echo.

RARE sequence

The RARE sequence uses an excitation pulse followed by a train of refocusing pulses to produce multiple spin echoes [16]. The excitation pulse is followed by multiple refocusing pulses which are each distinctively spatially encoded. Therefore, multiple k-space lines can be sampled following each excitation resulting in a considerable reduction in the scan time. The reduction in scan time compared to a normal spin echo sequence is characterized by the RARE-factor [17]. When a RARE-factor of 16 is used, 16 echoes are spatially encoded during one T_R reducing the total experimental time by a factor of 16, as used in this work.

Gradient echo pulse sequence

Gradient echo (GRE) imaging is primarily used in fast imaging and is therefore commonly used in 3D volume imaging. The 180° RF refocusing pulse is not needed in GRE imaging. Refocusing occurs through gradient reversal on the frequency encoding direction. First the spins are dephased by a readout

gradient lobe. Subsequently, the spins are rephased by a readout gradient with opposite polarity to the first gradient. When flip angles less then 90° are used, the pulse sequence is called gradient echo fast imaging (GEFI). Therefore, the longitudinal magnetization is never fully excited by an RF refocusing pulse leaving a substantial proportion always aligned along the z-axis [15]. A GEFI pulse sequence was used to acquire T_1-weighted images.

1.1.3 Functional magnetic resonance imaging (fMRI)

Functional magnetic resonance imaging (fMRI) is enabled by the magnetic properties of oxygenated hemoglobin (oxyhemoglobin (Hb)) and deoxygenated hemoglobin (deoxyhemoglobin (dHb)). DHb is paramagnetic and thus influences the local susceptibility of the surrounding magnetic field. The distortions that are caused by its presence lead to a local decrease of T_2^*. Increased neural activity leads to an increase of cerebral blood flow (CBF) (neurovascular coupling) and therefore, to a net decrease of dHb. This in turn leads to a small increase of the local MR signal which is caused by the changes in blood oxygenation. The described effect is called 'blood oxygenation level dependent (BOLD)' and is the basis for most of the fMRI studies conducted in humans [18].

However, the BOLD effect is not a direct measure of neural activity. Since the application of anesthesia BOLD imaging is not ideally suited for functional MR imaging in rodents.

1.1.4 Paramagnetic contrast agents

The use of paramagnetic ions as contrast agent for MRI was first suggested by Lauterbur in 1978 [19]. Paramagnetic substances possess a permanent magnetic moment. These magnetic moments are randomly aligned without

an externally applied magnetic field. Upon application of a magnetic field the magnetic moments align parallel to the field and produce a local magnetic field. The interaction with the externally applied field leads to an effective lessening of the two relaxation times of neighboring nuclei, resulting in signal enhancement [20]. Quantum mechanically, the property of paramagnetism is caused by the presence of an unpaired spin [20]. As the magnetic moment of an unpaired electron spin is essentially greater than that of an unpaired neutron or proton spin, agents with unpaired electron spin are especially suited as NMR contrast agent [20]. Paramagnetic ions possess magnetic moments which exceed that of protons 1000 fold [21]. The electronic spin is characterized by very short relaxation rates, which cause rapid fluctuations of the local fields, thus inducing transitions between the nuclear spin states [22]. The effectiveness of paramagnetic contrast agents depends on the effective magnetic moment, the correlation time (meaning that ions with very short electron spin relaxation times, such as Co^{2+}, are poor agents), the temperature and the value of the external magnetic field [22]. Both relaxation times, T_1 and T_2, are effected by the presence of paramagnetic contrast agents. However, the shortening of T_1 leads to an increase in signal intensity until the optimal concentration is reached. Further increasing the concentration of the contrast agent decreases signal intensity due to effects on T_2 [23]. Therefore, it is advantageous to use contrast agents which exhibit greater effects on T_1 than on T_2 and pulse sequences that highlight changes in T_1 [23], as the acquisition of T_1-weighted images.

1.2 Analysis of MRI data

For human brain imaging automated methods for data analysis are widely available. To date, this is not the case for the rodent brain [24]. Due to

the dependence on the analyst and time consumption of manual analysis of large-scale studies, semi-automated or fully automated analysis is preferable. Existing semi-automated or automated methods mostly rely on complicated algorithms which are not available to the public. Therefore, a semi-automated approach is presented in the methods section (2.1.2). It is independent from in-house written software and relies instead on the use of the freely available software of statistical parametric mapping (SPM, www.fil.ion.ucl.ac.uk/spm). Another advantage of using SPM software for analysis is the similarity to human MRI data analysis. This allows for a better comparability between clinical and preclinical studies. This section shortly introduces the concept of SPM and steps necessary for analysis of the mouse brain. As acquired images in this work resemble anatomical images, only steps necessary for these type of data will be addressed.

1.2.1 SPM software package

SPM is a software package which is based on the programming platform Matlab. The idea of SPM is to construct and assess spatially extended statistical processes which are used to test hypotheses about functional or anatomical imaging data [25]. Statistical parametric maps are created at the voxel level by using the general linear model (GLM). The data are thus described in terms of experimental and confounding effects, as well as residual variability [25].

1.2.2 Spatial transformations

Usually the analysis of MRI data starts with a sequence of spatial transformations. These transformations aim at reducing differences among subjects, in order to perform voxel-based analyses across subjects, as the data derived

from a particular voxel is assumed to belong to the same brain region [25]. By violating this presumption one might introduce changes in voxel values not resulting from an applied paradigm [25]. Thus, between subject registration is necessary to account for variations in the positioning of the animals in the scanner. To ensure that brains of different subjects exhibit the same size for the voxel-based analysis images are usually spatially normalized. To date, there is no standardized mouse brain template available. Therefore, it is necessary to create mouse brain templates. Detailed steps of the creation of the mouse brain templates used are described in the methods section 2.1.2.

Smoothing of the images is commonly performed, since a proportion of the noise is assumed to be independent from voxel to voxel whereas the signal of interest extends over several voxels. Therefore smoothing, achieved by using Gaussian kernels, renders the distribution of noise more normal [25] and thus improves the signal-to-noise ratio [26]. The smoothed images are usually submitted to the model used for SPM analyses.

1.2.3 Statistical parametric mapping

1.2.3.1 GLM

The GLM is described by the equation $Y = X\beta + \epsilon$. The observed variable Y is described by a linear combination of an explanatory variable X, which is called the design matrix, and an error term ϵ [27]. β corresponds to an unknown voxel parameter. Each column of the design matrix is related to one of the effects that were built into the experiment or that might influence the result, added as explanatory variables, covariates or regressors. Figure 2.11 shows the design matrix used for the analysis for one of our studies. The first three columns contain MEMRI images of the three different experimental groups. Columns four to six contain the mean value of whole brain signal

intensities as covariate. Ordinary least squares are used to assess the relative contribution of each of these columns. Depending on whether one wants to look at a particular linear combination of these relative contributions or at all of them, T or F statistics are used for statistical comparison [27].

To be able to conduct hypothesis-free testing of signal intensity differences on a whole brain basis, comparison at the voxel level are necessary. In human MRI and fMRI studies this is a standard method for analyzing data. MRI images of a certain resolution consist of thousands of voxels. Performing tests on a voxel by voxel basis on thousands of voxels means performing thousands of tests. This introduces the multiple comparison problem: Using the common GLM approach, as SPM does, an univariate t-statistic for each and every voxel is calculated (mass-univariate testing). For images with a data matrix of 128×128×128, as used in this work, 2097152 tests need to be performed. This means that at an α-level of 5% 104858 voxels show up activated although there is no such information in the data. This is the so called multiple comparison problem. The most common solutions to this problem in MRI are the correction for family wise error (FWE) and the false discovery rate (FDR).

1.2.3.2 FWE

The FWE is a Bonferroni correction and is the most strict and consequent one. By using the FWE one simply divides the nominal α-level by the number of conducted tests ($\alpha = \frac{\alpha \mathrm{nom}}{n}$) with n denoting the number of voxels. However, in functional imaging neighboring voxels are spatially correlated. Thus, the number of independent observations in the data is smaller than the number of voxels. Therefore, in fMRI n needs to be replaced by the number of independent observations [26].

An advantge of using the FWE is that it leads to the minimization of α. However, the β-error is highly increased, meaning that many voxels that

should show an effect fall below the corrected threshold.

1.2.3.3 FDR

Another completely different approach is controlling for the false discovery rate. Instead of controlling the probability for ever reporting a false positive as with FWE, the FDR controls for the expected proportion of false positives amongst voxels declared positive [28]. Uncorrected p-values need to be determined for each voxel. These uncorrected p values are then ordered in increasing order $p_1 \leq p_2 \leq \cdots p_n$. Then the largest value k needs to be found so that $p_k < \alpha k/n$.

A problem of FDR correction is that if the t-statistics of the most significant voxel does not exceed the critical threshold, then none of the remaining voxels will.

In summary, the FWE controls for the probability of ever reporting a false discovery, while the FDR detects false positives and controls for them such that they do not make up more than α of the discoveries [28].

1.3 Manganese

The investigations of manganese as paramagnetic MRI contrast agent reach back to the early beginnings of nuclear magnetic resonance [29]. Today MEMRI is an increasingly used tool for imaging the rodent brain in preclinical research. However, one major drawback of manganese is its toxicity upon overexposure [30]. On the other hand, manganese is an essential trace element as the lack thereof leads to severe illness and even death [31]. The following sections will introduce the properties of manganese, and will mainly address todays knowledge about manganese toxicity, and how manganese enters the brain.

1.3.1 Occurrence in the environment and the body

Manganese is a chemical element with the atomic number 25 and thus belongs to the transition metals. It is the 12th most abundant element in the earth's crust [32] and can be found in many types of rocks and soil. Manganese does not occur as a pure metal in the environment but in oxidized form or as a salt bound to sulfur and chlorine[33]. Manganese in higher oxidation forms (Mn^{2+}, Mn^{3+} or Mn^{4+}) is used in steel production to increase the hardness, stiffness and strength of steel [33]. In these forms, manganese poses a threat to the health of people exposed to manganese as dust (e.g. miners and welders) [33].

Manganese can enter the body via several ways. The most common ones are inhalation (as dust) and ingestion. The amount of manganese intake via food may vary depending on the type of diet. The adequate intake for manganese was set to 2.3 and 1.8 mg/day for men and women, respectively (Food and nutrition board, Institute of medicine). The highest concentrations of manganese are found in nuts (18-46 ppm), grains (0.4-40 ppm), legumes (2.2-6.7 ppm), fruits (0.2-10 ppm), and vegetables (0.4-6.6 ppm) [34].

As natural component of the environment manganese is also part of the air, soil, and water. Near industrial sources manganese concentrations in the air are 20 times as high as in rural and urban areas. Manganese concentrations in soil depend strongly on the extent of mining activities and range from 40 to 900 mg/kg in normal soil up to 7000 mg/kg in soil with high mining activity [35, 36]. As some compounds of manganese are soluble in water ($MnCl_2$, $MnSO_4$) exposure to the trace element may also result from the ingestion of drinking water [34].

Manganese plays an important role in many physiological functions as a constituent of multiple enzymes and as an activator of other enzymes [37]. The antioxidant enzyme manganese superoxide dismutase is primarily present

in the mitochondria and serves to protect mitochondrial components from superoxide, which is a natural byproduct of respiration [38]. Manganese as a transition element can exist in multiple valence states. Thus it is able to promote redox reactions and form cytotoxic free radicals [32].

Manganese-activated enzymes play an essential role in the metabolism of carbohydrates, amino acids, lipids and proteins [30]. Furthermore, manganese plays an important role in normal immune function, the regulation of blood sugar levels and cellular energy. It is needed in reproduction, digestion and bone growth, and in the defense mechanism against free radicals [30]. Manganese is further needed in the urea cycle in the liver, where it is used in the form of arginase, to detoxify ammonia generated during amino acid metabolism [39]. Liver, pancreas and kidneys were found to have the highest manganese concentrations in humans, rats and monkeys [40]. However, manganese is also present in the brain, where it is needed for the conversion of glutamate to glutamine through the manganese-activated enzyme, glutamine synthetase [41]. Yet, manganese is not equally distributed throughout the brain. The highest concentrations are found in the olfactory bulb and pineal gland [40], brain structures which are both not entirely protected by the blood-brain barrier. In rats, high concentrations of manganese were also found in the hypothalamus [42]. Furthermore, regions of the basal ganglia, namely, the glopus pallidus (GP) and the putamen, contain slightly elevated manganese levels in rats [43].

1.3.2 Manganese deficiency

Non-experimentally induced manganese deficiency in humans has not yet been reported [30]. Animal studies, however, showed that those fed a manganese deficient diet had poor skeletal growth, poor bone mineralization, reduced cartilage development, and slow wound healing [44, 45, 46, 47]. Furthermore,

it could be shown in animals that manganese deficiency may play a role in defective ovulation, testicular degeneration, fetal malformations, and death of the fetus [48, 49, 50].

Some of these findings may also hold true in humans. Saner et al. (1985) measured the manganese hair concentration of pregnant women [51]. They found that women with low hair concentration of manganese gave birth to children with congenital malformations whereas the infants of women with normal hair concentrations of manganese were healthy.

The first case of manganese deficiency was reported by Doisy in 1974, who unintentionally eliminated manganese from a vitamin K-deficient diet for a patient [52]. The patient developed hypocholesterolemia; scaly, transient dermatitis; reddening of hair and depressed blood clotting proteins [52] after three and a half months on the diet. After administration of vitamin K the symptoms did not vanish.

Experimentally induced manganese deficiency was first reported by Friedman et al. (1987). Men who were placed on a manganese-depleted diet developed a erythematous rash on the upper torso, groin area and lower extremities [53]. Furthermore, women with manganese consumption lower than 1 mg manganese/day developed altered mood and increased pain during the premenstrual phase of their estrous cycle [30, 54].

Moreover, manganese deficiency could lead to some forms of cancer as a consequence of the functional loss of the manganese-containing enzyme, superoxide dismutase, which plays a role in the protection of cells from free radicals [55].

Additionally, studies seem to point towards an involvement of manganese deficiency in the development of diabetes. It has also been found that blood manganese concentrations in epileptic patients is lower than in normal people [56], indicating an involvement of manganese in the pathology of epilepsy.

1.3.3 Manganese toxicity

In contrast to manganese deficiency which is not normally observed in nature, manganese toxicity is. Since 1837, it has been known that overexposure to manganese can lead to an acute psychiatric symptom called 'Manganese madness' [57]. It was first found in welders in a manganese ore grinding plant in France. The symptoms consisted of low-volume speech, drooling, and loss of facial expression [32]. It was furthermore shown that chronic exposure to manganese produces parkinson-like symptoms [58]. The best studied cases of manganese-induced parkinsonism, also called manganism, are in a group of Chilean miners [59, 60, 61, 32] and Taiwanese alloy smelters [62]. The parkinson-like symptoms might be a consequence of the accumulation of manganese in the dopaminergic system of the brain since it has been shown that manganese accumulates preferentially in the basal ganglia. Histopathological investigations of the brain after manganese overexposure showed neuronal degeneration in the GP, substantia nigra and in the caudate nucleus and putamen of the striatum [63, 64]. It was shown by Erikson et al. (2005) that the dopamine transporter plays a crucial role in facilitating manganese accumulation in the striatum and, therefore, might be essential for the mediation of manganese neurotoxicity [65]. Together with the loss of postsynaptic striatal dopaminergic projections [66] these results show the direct impact of manganese overexposure on the dopaminergic system.

Furthermore, it has been shown that interactions of manganese with the neurotransmitter glutamate (Glu) not only reduce the ability of astrocytes to remove Glu from the extracellular space, but also increases the sensitivity of the glutamate receptor to Glu and lead to the inhibition of mitochondrial activity [67, 68, 69]. The causes of manganese-induced neuronal damage are most likely due to disruption of mitochondrial function [70]. It has

been shown that acute exposure to high levels of manganese interferes with normal mitochondrial respiration [71], which leads to oxidative stress in the cell due to the alteration of glutathione and superoxide dismutase enzyme activity [72, 67, 73], two major protective mechanisms against oxyradicals. The disturbance of this protective mechanism leads to the local formation of oxyradicals, resulting in a disturbance of iron homeostasis and mitochondrial functioning [74]. The formation of free radicals through manganese overexposure may lead to an enhancement of the auto-oxidation of catecholamines, such as dopamine, and further to an increased production of 6-hydroxydopamine, which is a selective catecholaminergic neurotoxin and therefore might cause death of dopaminergic and noradrenergic cells [75, 76, 77].

The initial location of manganese accumulation, the GP, is a GABAergic nucleus [78]. However, the effects of manganese on regional GABA levels are diverse. One early study about manganese intoxication showed an increase in GABA levels in the caudate nucleus of the brain in rats upon systemic manganese overexposure [79]. In contrast to this finding, studies carried out a few years later showed a decrease in GABA levels after manganese exposure over a longer time period (15 to 30 days) [80, 81, 82]. However, the contradictory results may arise from different manganese treatment protocols [78]. Regardless, all of these studies indicate that the GABAergic system is affected upon chronic exposure to manganese.

In summary, the detailed causes about what mediates manganese toxicity are still unknown. However, it seems plausible that all three major neurotransmitters in the basal ganglia are affected by manganese overexposure [78].

1.3.4 Transport of manganese

Manganese as a contrast agent is most commonly used as the paramagnetic ion Mn^{2+}. However, to be able to use Mn^{2+} as a contrast agent in neuroimaging it needs to be delivered to the brain. Therefore, it is necessary to understand how Mn^{2+} enters the brain and how it is further transported once it is in the brain. Thus, a short overview of what is currently known about the transportation of Mn^{2+} in the central nervous system will be given.

1.3.4.1 Entering the brain

Before being available in the brain as contrast agent, Mn^{2+} first needs to enter the brain. Three pathways hypothesized as possible mechanisms for Mn^{2+} entrance into the brain: through the olfactory system, across the blood-brain barrier (BBB) or through the cerebro-spinal fluid (CSF).

Olfactory system

As the olfactory tract is not protected by barriers, application of Mn^{2+} via the olfactory system seems to provide the easiest pathway. It has been shown in rodents and pike fish that Mn^{2+} is able to be transported into the brain via the olfactory nerve into the olfactory bulb upon exposure to Mn^{2+}-containing air [83, 84, 85]. Once in the olfactory bulb Mn^{2+} is transported further into the brain and can be detected in other regions such as the visual cortex [86].

BBB

The BBB is an active interface, that restricts the transport of potentially toxic or harmful substances from the blood into the brain [87]. Another important function is the so called carrier function, which enables the transport of nutrients into the brain and the removal of harmful metabolites [87]. It

therefore plays an important role in maintenance of the CNS homeostasis [87]. Small lipid-soluble molecules like oxygen (O_2) and carbon dioxide (CO_2) pass through the BBB via diffusion. But most of the substances that need to pass the BBB cannot do so by diffusion are not lipid soluble. These substances cross the BBB by carrier-mediated transport systems [88].

Yamada et al. (1986) found that manganese accumulation in the brain occurs in iron-rich areas [63]. It was therefore suggested that transport systems for Mn are similar to those for iron. This introduced the idea of Transferrin (Tf) mediated transport across the BBB. However, experiments investigating the role of Tf in manganese transport show controversial results [89, 90]. A study by Crossgrove and colleagues (2003) in rats provided evidence for carrier-mediated influx of Mn^{2+}, Mn citrate and Mn Tf through cells comprising the BBB [91]. Manganese Tf is likely to enter the brain through Tf receptor-mediated endocytosis [91, 90, 92]. Furthermore, it is stated that uptake as manganese citrate is transferred across the BBB. However, transporter candidates for manganese citrate are hard to predict [91]. Mn^{2+} is predicted to be carried across the BBB by the divalent cation or metal transporter (DCT1, DMT1), which serve as high affinity non-transferrin bound iron membrane transporters with non-selective affinities for Mn^{2+} and other divalent ions [91, 93, 94]. In summary, the study found that Mn^{2+}, manganese citrate and manganese Tf do not cross the BBB via diffusion but through carrier-mediated transport. Transport rates were found to be highest for manganese citrate, indicating a special role for this specific pathway.

CSF

Another possible way for manganese to enter the brain is across the epithelium of the choroid plexus (CP) into the CSF in the ventricles and eventually across the ependyma into the parenchyma [95]. It was shown that entrance over

the CP is independent of carrier proteins [96]. Furthermore, brain regions with large ventricular space showed great signal enhancement in T_1-weighted images which had vanished 24 hours after administration and had spread throughout the brain [97], indicating the entrance into the brain through the CSF. The same study showed that two hours after injection brain regions near the ventricles showed enhanced signal intensity compared to regions far from the CSF [97, 98]. Furthermore, Bock and colleagues state that Mn^{2+} uptake of non-human primates primarily takes place through the CSF [95], as strong accumulation was found in regions adjacent to the lateral ventricles; however, they did not exclude the possibility that parts of Mn^{2+} were taken up via the BBB.

In summary, it is not known which route manganese prefers for entering the brain. However, data concerning the crossing of the BBB are controversial and it is still not clear exactly which transporters are involved in mediating the transport across the BBB. From the data taken from the literature it seems plausible that manganese is primarily transported across the CSF into the brain. Additionally, upon disruption of the BBB the influx of manganese into the brain can be strongly increased [89], indicating a major involvement of the BBB in preventing the entrance of maganese into the brain. It has been furthermore shown that at normal plasma concentrations transport across the BBB dominates whereas at high plasma concentrations transport across the choroid plexus is prevalent [95, 89, 99]. Through intraperitoneal (ip) administration of Mn^{2+} high manganese plasma levels are induced temporarily. This indicates that in the experiments performed in this work manganese most likely entered the brain primarily via the CSF.

1.3.4.2 Transport in the brain

Due to its chemical similarity to Calcium (Ca^{2+}) [100], Mn^{2+} is able to enter neurons through L-type voltage-gated Ca^{2+} channels during neuronal depolarization upon neuronal activation [101]. This has been shown to be true in the brain as well as in the heart [101, 102, 103, 104]. Figure 1.5 illustrates the transport of Mn^{2+} in the neuron. Once in the neuron Mn^{2+} ions are taken up by the endoplasmic reticulum [83, 105] where they are most likely packaged in vesicles [72, 106]. Through blockade of axonal transport in both anterograde and retrograde directions it could be shown that Mn^{2+} is transported down the axon [72] to the presynaptic site of the neuron. There it is released into the synaptic cleft and taken up by the next neuron [106, 107]. This process enables the use of Mn^{2+} as an *in vivo* tract tracer.

1.3.5 The clearance of manganese from the brain

The efflux of Mn^{2+} from the brain has been barely studied [108]. However, it has been shown by autoradiographic measurements in the rat brain that the biological half-life of Mn^{2+} in the brain ranges from 51 to 74 days with the longest half-lives in the hypothalamic nuclei and the thalamus [109]. Furthermore, this study showed that the half-life of Mn^{2+} in the brain is by far longer than in the rest of the body, which might indicate that Mn^{2+} is carrier transported into the brain, but not out of it [108]. An *in vitro* study on cultured chick glial cells indicates that the efflux of Mn^{2+} is diffusion mediated [110]. Another study investigated the decline of MRI signal intensity after intravenous infusion of $MnCl_2$ and found that intensities had declined to near control levels after 14 days [97].

However, investigations about which mechanisms mediate the efflux of Mn^{2+} from the brain are still necessary to fully understand the dynamics

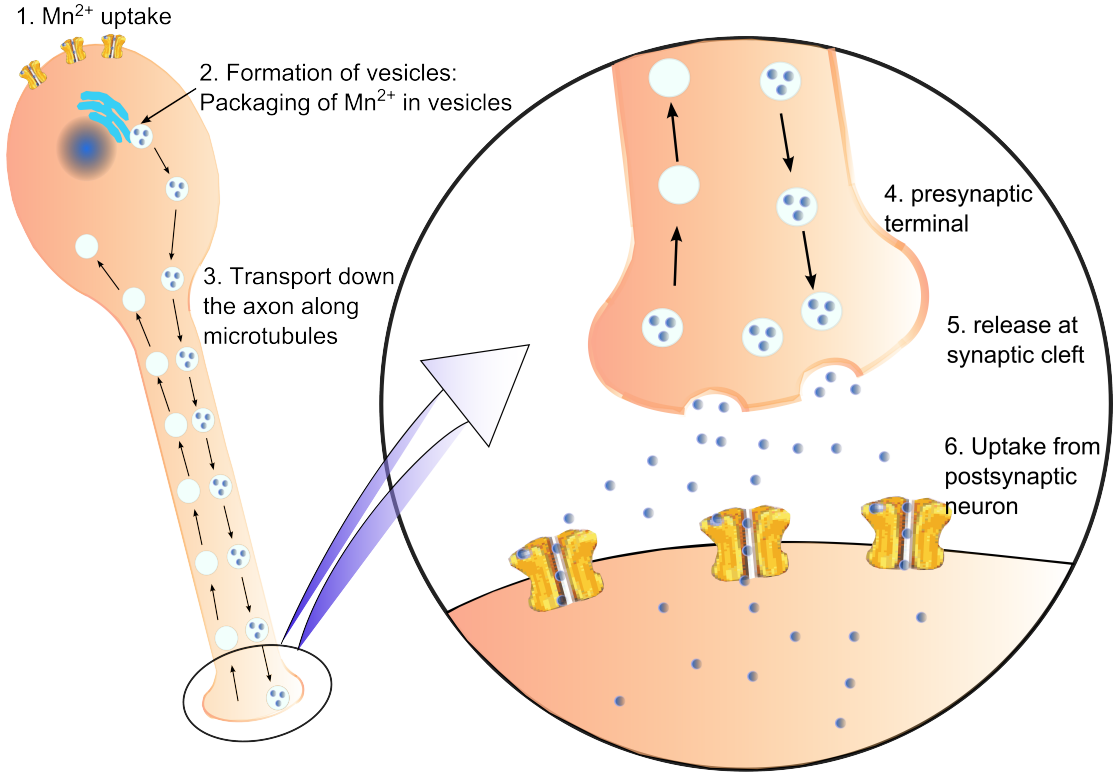

Figure 1.5: Scheme of Mn^{2+} transport. After having entered the brain Mn^{2+} ions enter the neuron through voltage gated Ca^{2+} channels (1). They are then taken up by the endoplasmic reticulum and packaged into vesicles (2). They are further transported down the axon via microtubules (3). Once at the presynaptic terminal of the neuron (4) the ions are released into the synaptic cleft (5) and taken up by the next neuron again through voltage gated Ca^{2+} channels (6).

of Mn^{2+} and especially the reason for why it stays in the brain for a much longer period than in any other tissue.

1.4 MEMRI

The use of Mn^{2+} as MRI contrast agent was initialized over 20 years ago by London et al. (1989) [111] who studied its toxic effects on anesthetized rats. MEMRI is increasingly used in animal research due to its increased soft

tissue contrast. Its paramagnetic property leads to an effective reduction of the T_1-relaxation times of the surrounding tissue and therefore to a contrast enhancement of brain structures. Figure 1.6 shows the difference between a brain of a mouse which was injected with $MnCl_2$ and a brain of a mouse injected with NaCl. The effects of the presence of Mn^{2+} ions are clearly visible. Especially regions with high cellular density, such as the hippocampus (HPC) and the central nucleus of the amygdala (CeA) [112], show a great signal enhancement, whereas NaCl injected animals show little native contrast.

The evolution of MEMRI began in the late nineties, where it was first used as a neuronal tract tracer [106] and activity marker [113]. Together with anatomical imaging, tract tracing and activtiy dependent assessement are the main applications of MEMRI in biological systems [114].

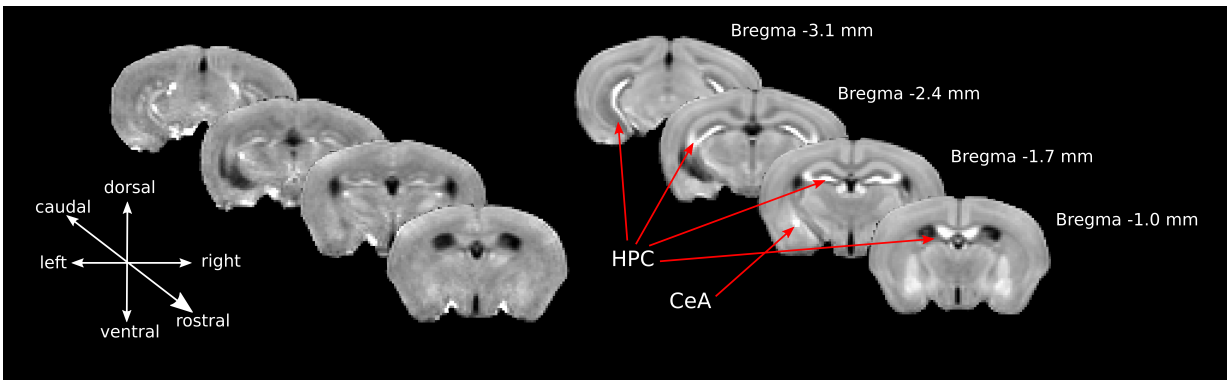

Figure 1.6: Effect of Mn^{2+} on contrast enhancement in the brain. Images of mouse brains of mice injected with $MnCl_2$ (right) and NaCl (left). The paramagnetic property of Mn^{2+} ions leads to an effective reduction in the T_1 times, which yields contrast enhancement on T_1-weighted images. Structures such as the HPC and CeA (red arrows) show great signal enhancement. Bregma coordinates of shown slices are indicated to the right of $MnCl_2$ injected brain. Further, directions within the brain are denoted on the lower left corner.

1.4.1 Neuronal tract tracing

The use of MEMRI as a tool for neuronal tract tracing is enabled by the fact that Mn^{2+} is transported along neurons by microtubule-dependent axonal

transport and is able to cross synapses and thus reach interneurons leading to contrast enhancement of the brain circuit in question [114]. Tract tracing is achieved by the application of Mn^{2+} directly into the desired pathway. The first studies were performed on the visual and olfactory system by placing Mn^{2+} directly into the vitreous of the eye or into the nasal cavity, respectively [83, 115]. Furthermore, the auditory system was investigated using a cochlear Mn^{2+} injection [116]. Pioneer work in the field of neuronal tract tracing using MEMRI was carried out by van der Linden et al., who studied the song bird vocal control system and brain plasticity [117, 118, 119] upon intracerebral injections of $MnCl_2$.

1.4.2 Anatomical imaging

The use of MEMRI as an anatomical imaging tool is rendered possible simply by the fact that Mn^{2+} enters neurons. Figure 1.6 shows the astounding effect of the presence of Mn^{2+} in the brain. The low native contrast is enhanced especially in structures such as the HPC or CeA. This effect facilitates the identification of studied brain structures in the brain. It has already been used in studies interested in changes in hippocampal volume [120], or as a marker for lesions [121, 122]. Furthermore, the volume of the song center of birds has been studied using MEMRI [118].

1.4.3 Functional imaging

MEMRI as a functional imaging tool is especially interesting for imaging studies in rodents. For ethical reasons and the avoidance of artifacts, animals have to be anesthetized during the scanning procedure. Therefore, the use of classical BOLD imaging (section 1.1.3) in rodents is difficult, as the application of anesthesia leads to unknown effects on the BOLD response. In contrast,

MEMRI is not primarily dependent on hemodynamic changes as a correlate of neuronal activity, but rather reflects neuronal activation directly at the cellular level. Its use as functional imaging tool is enabled by its chemical similarity to Ca^{2+}. As previously stated Mn^{2+} ions are able to enter neurons via voltage-gated Ca^{2+}-channels and its accumulation in neurons is activity dependent [114, 100]. As the MEMRI contrast builds up over a longer period of time [95] it becomes possible to expose awake animals to complex behavioral paradigms [123]. MEMRI has already been successfully applied in murine studies. For example, it has been used for mapping of sound evoked activity in mice [124]. It has furthermore been shown that Mn^{2+} accumulation in the somatosensory cortex was significantly increased in mice after whisker stimulation [125]. Another study showed an increase in signal intensity in the hypothalamic nucleus after feeding the animals different diets [126].

All these successfully executed studies show, that MEMRI has a great potential to become an exceptional tool for *in vivo* functional imaging.

1.5 Mouse model of extremes in trait anxiety

As the main study of this work investigates a mouse model of extremes in trait anxiety using MEMRI, the following chapter will deal with anxiety, the mouse model used and describe what is known about the neurocircuitry of anxiety.

1.5.1 Anxiety

Anxiety constitutes a normal response to threatening situations and is considered a normal emotional state throughout the human population [127]. Anxiety is an essential emotion in the identification of threat and danger and therefore, serves a physiological protective function. Transient anxiety states

trigger an appropriate response, which is often expressed as escape or avoidance of the threat, and is of fundamental importance for the survival of higher order animals [128]. In healthy subjects, anxious states are regulated by inhibitory and facilitatory mechanisms, which either oppose or activate anxious states [128]. These mechanisms serve several functions, such as: to avoid extensive anxiety states, to trigger responses which are proportional to the encountered danger, to allow behavioral response (escape, avoidance), and to restore a normal emotional condition once the threat has passed [128]. The disturbance of these mechanisms may lead to an excessive experience of anxiety, which is a clinically defined, pathological anxiety-related state. This state manifests itself in a wide variety of ways and ranges from disproportionate responses to perceived threats or the tendency to interpret equivocal situations as threatening to chronic anxiety without obvious cause [129].

Anxiety has furthermore been defined as the fearful reaction to another emotion, such as the fear of the panic response in panic disorder [130]. Anxiety disorders not only cause significant distress and suffering in the lives of patients, but they are also among the most common types of psychiatric disorders [127]. An international study conducted by Kessler and colleagues (2007) found, that anxiety disorders were the most prevalent kind of psychological disorder in ten of 17 investigated countries [131].

Several distinct human anxiety disorders are described by the DSM-IV [132] and the international classification of diseases ICD-10 [133]. Included are: panic disorders, obsessive-compulsive disorder, post-traumatic stress disorder, social phobia, specific phobias, and generalized anxiety disorder [134].

Although the spectrum of emotions which is perceptible by rodents is thought to be much more limited than that of humans [127], anxiety-related behavior in particular may be very well modeled in rodents and shows remarkable resemblance with human anxiety [135, 127]. However, scientists are often

tempted to interpret fear responses as 'anxious' or 'brave' behavior [136]. As most of the behavioral tests for anxiety-related behavior rely on measures of locomotion, anthropomorphizing results gained from these experiments needs to be avoided. Only if the behavior of the animals can be influenced by the application of anxiolytic drugs (e.g. benzodiazepines) it is justified to refer to it as anxiety-related behavior [136]. A very promising approach to model trait anxiety in animals is selective breeding. According to Landgraf et al. (2007) [137], the technique of selective breeding appears to be superior to targeted gene knockouts, as an entire array of neurobiological mechanisms and pathways are selected for, instead of just one altered specific gene and gene product. In this work we investigated one such mouse model and it will be described in detail in the following subsection.

1.5.2 Mouse model of extremes in trait anxiety

The mouse model of extremes in trait anxiety consists of three selectively bred lines, which are high, normal, and low anxiety-related behavior mice (HAB, NAB, and LAB respectively). The breeding strategy for establishing the mouse model of extremes in trait anxiety was based on a strategy which was already applied succesfully in rats [138, 139]. The starting point for breeding the animals was the CD1 outbred strain (i.e. animal with heterogeneous genetic background). Breeding is based upon the behavior of the mice on the elevated plus maze (EPM). The EPM, as most anxiety-related behavioral tests, challenges the animals congenital anxiety of open and brightly lit spaces against their sense of exploration. On the EPM animals have the choice between two dark, closed and two brightly, lit open arms (figure 1.7). Anxiety-related behavior can be rated based on the time spent on each one of these arms [140]. The variance of this natural behavior between single subjects was exploited by pairing animals with extreme behavioral data, meaning

either spending very little time on the open arms, or very much time on the open arms. This breeding strategy resulted in the HAB, NAB, and LAB mouse lines (figure 1.8). In general, HAB spent less than 10%, LAB more than 50% and NAB around 30% on the open arms of the EPM [140]. More than 250 animals from more than 15 litters of outbred CD1 mice were used as a starting point for selective and bidirectional breeding for anxiety-related behavior [141]. Figure 1.8 shows the development of the time spent on the open arms of the EPM (%TOA) over the course of the different generations up to today. A stable phenotype of both lines, HAB and LAB, developed after a few generations. NAB mice were added in 2005 to provide an intermediate phenotype with intermediate times spent on the open arms, comparable to former CD1 mice. The increase in times spent on the open arm after generation 35 in all three lines is caused by a restructuring of the scoring from manual to automatic. So far, many studies have been performed on these mouse lines, from genetic investigations [142, 137] to investigations of brain functioning mostly using c-Fos staining after exposure to stressors [129, 143]. Genetic investigations showed that the different strains differed significantly in the expression of glyoxalase-I, vasopressin and TMEM132D [144, 142, 141]. Glyoxalase-I, a cytosolic enzyme which plays a major role in the detoxification of dicarbonyl metabolites, has been shown to be underexpressed in brain tissue and blood in HAB mice whereas it was found to be overexpressed in LAB mice in the same tissue types, compared to NAB line [141]. This pattern was so reliable and robust, glyoxalase-I was even suggested as a biomarker of anxiety-related behavior in the HAB/NAB/LAB mouse model, since it would help to categorize subsets of animals in a more reliable and consistent manner [141, 137].

The neuropeptide arginine vasopressin (AVP) acts as a neuromodulator or neurotransmitter when released within distinct brain areas and it is able

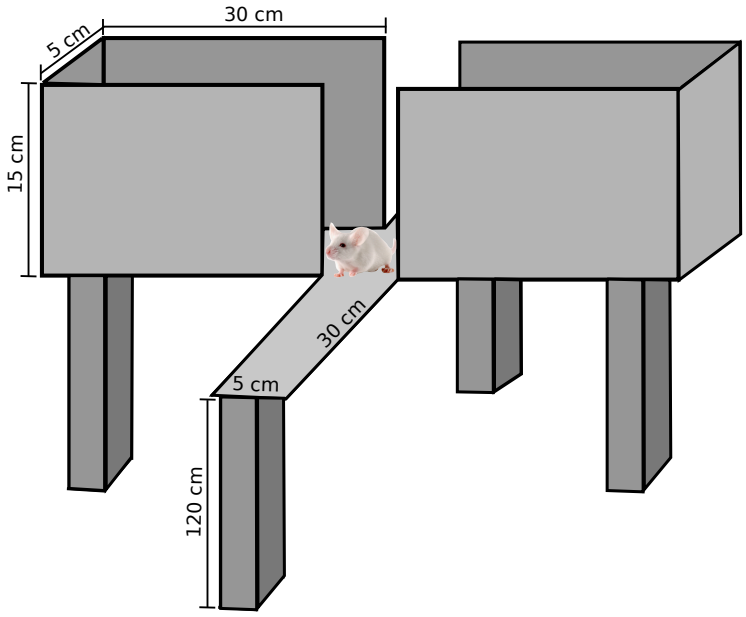

Figure 1.7: Elevated plus maze. The EPM consists of two open (30 × 5 cm) and two closed (30 × 5 × 15 cm) arms. It is located 120 cm above the floor [141]. The more anxious the animals are the less time they will spend exploring the open arms of the EPM.

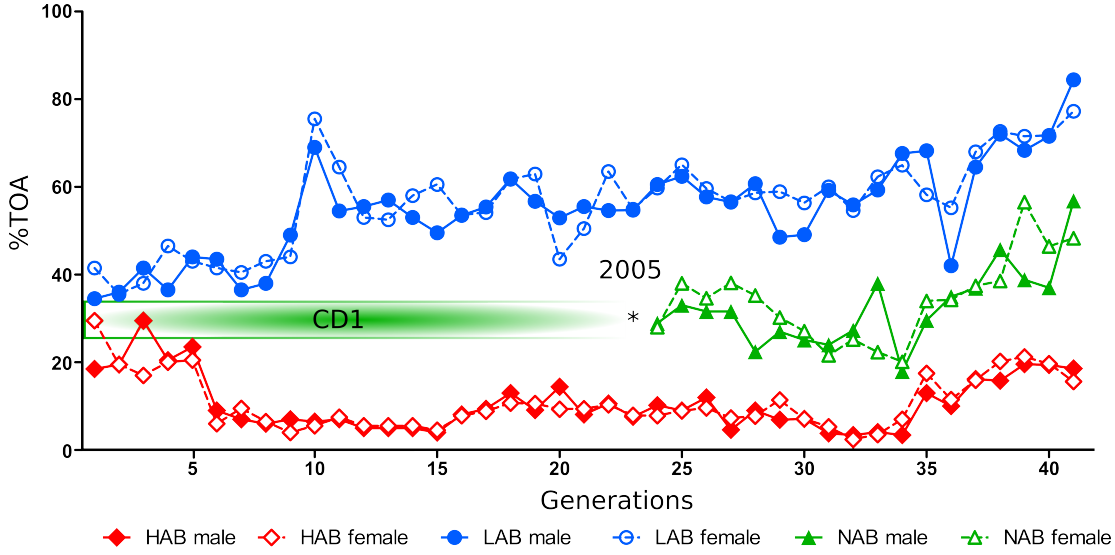

Figure 1.8: Selective breeding due to the behavior on the elevated plus maze. The graphic shows the breeding curve over 41 generations. Males (closed symbols) and females (open symbols) with either spending very low (high anxiety-related behavior) or very much time (low anxiety-related behavior) on the open arms of the EPM. %TOA denotes the percentage of time spent on the open arm of the EPM. After few generations a stable separation of HAB and LAB lines is observable. In 2005 NAB lines were added as 'supercontrol' [136] (indicated as * in the figure), with males and females behaving like the group average of CD1 mice.

to regulate wide varieties of brain functions and may influence emotional behaviors [142, 137]. It could be shown that the expression of AVP in the paraventricular nucleus of the hypothalamus (PVN) was decreased in LAB animals [142]. In the same study it was shown that LAB animals exhibited signs of diabetes insipidus, namely increased intake of fluid and diminished urine osmolality [142]. This might be associated with the lack of AVP, which is known to be decreased in diabetes insipidus.

Differences in the expression of TMEM132D were studied after the gene was identified as susceptibility gene for panic disorder in a human genome wide association study. The study showed a significantly increased expression of TMEM132D in HAB animals compared to LAB in the cingulate cortex. All other investigated brain regions did not reach significance [144].

The animals were furthermore exposed to a number of different behavioral tests. Besides the EPM, they were also exposed to the dark-light avoidance test, open-arm exposure test, ultrasound vocalization test, tail-suspension test and the forced swim test [141]. LAB mice not only spent significantly more time in the light compartment compared with HAB and NAB mice, they also had more frequent head dips in the open-arm exposure test. Furthermore, HAB pups emitted significantly more cries in the ultrasound vocalization test. In the tail suspension and the forced swim test HAB mice displayed significantly increased immobility time. These tests all indicate a higher level of anxiety in HAB as compared to LAB mice, whereas LAB mice showed reduced depression-like behavior as assessed with the tail-suspension and forced swim test [141]. However, these studies rarely used NAB animals as controls. Thus, it is not known, which of the extremes, HAB or LAB, show altered behavior as compared to controls.

Furthermore, it could be shown in rats that corticosterone secretion under basal conditions were similar in both lines, HAB and LAB. In contrast, corti-

costerone response to open arm exposure was significantly increased in HAB animals, indicating a hyper-reactive hypothalamic-pituitary-adrenal (HPA) axis in HAB animals [145]. Again, NAB animals were not tested.

1.5.3 Neurocircuitry of anxiety

As previously mentioned, *in vivo* imaging studies using BOLD-based fMRI are difficult to apply in rodents. This is especially the case for testing anxiety-related paradigms because the application of psychological stressors under anesthesia is more or less impossible. However, attempts to conduct classical fMRI studies on anxiety in conscious rodents have been made. Stress caused by the scanning procedure was reduced through a training procedure before the scans and the administration of anxiolytic drugs. Both studies were performed in rats [146, 147]. However, these methods are either not applicable in mouse models or still need to be established. Due to the shortcomings of *in vivo* imaging methods of anxiety circuits, functional *ex vivo* staining methods are frequently applied in stress and anxiety research to study neuronal activity patterns in the brain [127]. These methods include staining for immediate early gene expression, mainly c-fos, following a stressor. The reason that c-fos expression is so common is due to its low level of basal expression, making its upregulation easily detectable [127]. Upon stimulation c-fos is induced in the cell nucleus within a couple of minutes. Its protein product, c-Fos, can be detected between 1 and 3 hours after the stimulus and disappears 4 to 6 hours after treatment [127].

Figure 1.9 shows a sketch of the sites of neuronal activation in HAB/LAB rodents as revealed by c-Fos staining. Differential activations were found after the exposure to five different aversive stimuli in rats and mice. These stimuli included exposure to the open arm of an EPM [129, 148], exposure to the open field [148], social defeat [149], airjet [143] and the administration

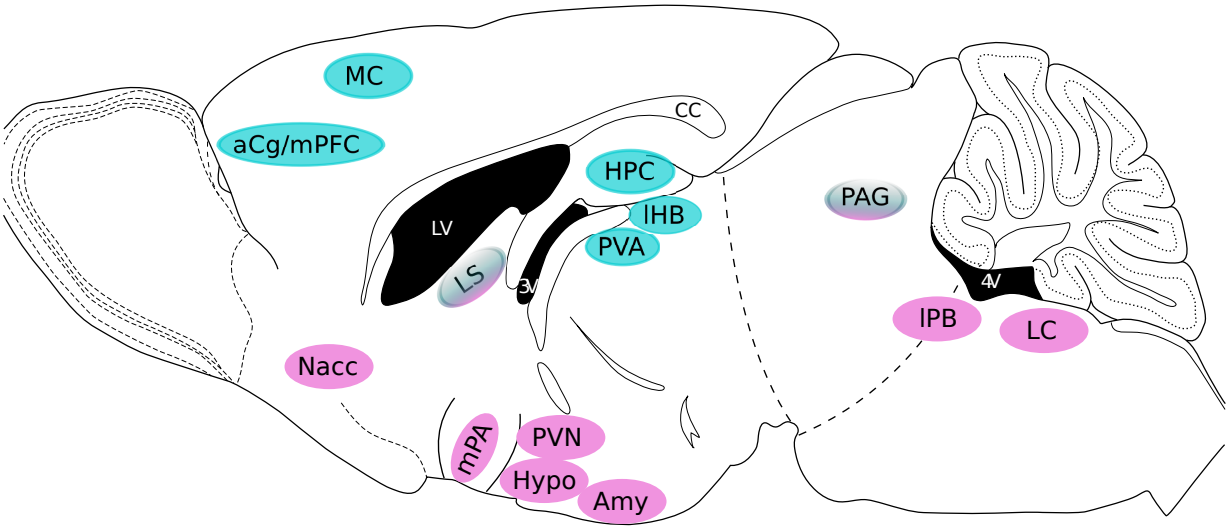

Figure 1.9: Sites of neuronal activation as found by c-Fos staining in anxiety. The figure shows which brain regions have been found to be differentially activated in HAB vs LAB rats as assessed by c-Fos mapping. Changes have been found after exposure to five different challenges namely, air jet exposure, administration of the anxiogenic drug FG-7142, open arm exposure, open field exposure and exposure to social defeat. Blue stands for hypoactivation, red for hyperactivation in HAB vs LAB rats [127]. aCg: anterior cingulate cortex; mPFC: medial prefrontal cortex; MC: motor cortex; HPC: hippocampus; PVA: paraventricular thalamic nucleus; lHB: lateral habenular nucleus; LS: lateral septum; mPA: medial preoptic area; Nacc: nucleus accumbens; PVN: paraventricular hypothalamic nucleus; Hypo: hypothalamic area; Amy: Amygdala; PAG: periaqueductal gray; lPB: lateral parabrachial nucleus; LC: Locus coeruleus; CC: corpus callosum; LV: lateral ventricle; 3V: third ventricle; 4V: fourth ventricle. Concept of figure taken from [127].

of the anxiogenic drug FG-7142 [143]. It has to be noted that identification of the neuronal population activated depended heavily on the applied stimulus, indicating that particular aspects of provoked aversion, fear or anxiety activate specific parts of the anxiety circuitry [127]. Brain regions that were found to be differentially activated in HAB vs LAB animals included parts of the limbic system, such as the medial prefrontal cortex (mPFC) and the amygdala. The mPFC, which provides inhibitory input to the amygdala, was found to be hypoactivated in HAB as compared to LAB animals, whereas the amygdala showed hyperresponsive neurons in HAB animals. Furthermore, the septo-hippocampal system was found to be differentially activated. While the septum showed hypoactivation in the ventral and hyperactivation in the

dorsal part, the HPC was only hypoactivated after exposure to the different stressors. Distinct regions of the hypothalamus (HTh), namely the medial preoptic area and the medial and lateral hypothalamic areas showed hyper-responsive neurons in HAB animals. Furthermore, the PVN, which is known to be involved in the integration of stress reactions and had been shown to be responsive to induced anxiety [127, 150, 151, 152], expressed significantly more c-Fos protein in HAB animals as compared to LAB animals. In the thalamus (Th), the habenula and the paraventricular thalamic nucleus there was less c-Fos response in HAB animals. Another very important brain region in mediating anxiety-like behavior which was found to be differentially activated between the different mouse lines was the periaqueductal gray (PAG). Increased c-Fos expression could be shown in HAB animals in the dorsolateral PAG after administration of FG-7142 or airjet exposure, causing escape behavior [143]. The same study showed a hyperactivation of neurons of the locus coeruleus of the brain stem.

The discussion will go into detail for some of the brain regions found and how they belong to the neurocircuitry of anxiety.

1.6 Cytochrome oxidase activity

Cytochrome oxidase (CO) is the terminal enzyme in the electron transport chain. One of its functions is to catalyse the transfer of electrons from ferrocytochrome-c to molecular oxygen to form water [153]. During this reaction, ATP is formed through the coupled process of oxidative phosphorylation [153]. As the brain is primarily dependent on oxygen for its energy supply, the level of CO activity should positively correlate with its functional level of activity [154, 155]. CO activity is furthermore an indicator of longer term metabolic demand [156]. To explain the rate of change of CO activity Poremba

et al. gave a nice analogy between muscle size and staining for CO activity: "As the demand on a muscle increases with sustained use, the muscle grows, reflecting its greater mechanical capacity[...]. Similarly, as the energy demand on brain cells is increased by sustained use, CO activity increases. Thus the CO increase reflects a greater metabolic capacity of brain cells." [157]. CO staining has been used as a measure of neuronal activation in the field of anxiety research [157], where it was shown that classical conditioning modified CO activity in the auditory system. Furthermore, increased CO activity was found in the CeA and the basolateral amygdala in HAB as compared to LAB mice under basal condition. The same study showed hypoactivity in the PVN [140].

In this work, staining for CO activity is used as a verification of MEMRI measurements, due to its long term characteristics. A study in the visual cortex of marmosets showed that the distribution patterns of manganese and CO activity do resemble each other [158]. Unfortunately, they have not shown whether manganese accumulation and CO activity correlate with each other.

1.7 Aims of the thesis

The general aim of the present thesis was to investigate MEMRI as a tool for functional *in vivo* imaging. The major aims of the conducted studies of the present thesis were as follows:

1. Reduction of toxic side effects of manganese by fractionated delivery to enable the performance of longitudinal studies and application of complex paradigms

2. Investigation of contrast dynamics in fractionated MEMRI applications

3. Development of a semi-automated data analysis pipeline to reduce the

dependency on the operator and to introduce time efficiency

4. Application of fractionated MEMRI in a mouse model of extremes in trait anxiety

5. Validation of MEMRI results with an independent histological staining method

Chapter 2

Methods

This work includes three different studies. Study I (Fractionated MEMRI) investigated the effects of different fractionated Mn^{2+} application protocols on MRI contrast enhancement as well as physiological measures in C57BL/6 mice. This study has been published in 2010 in the journal NMR in Biomedicine [123]. As this study had exploratory character, no hypotheses were probed.

Study II (dynamical behavior of Mn^{2+}) investigated the dynamical behavior of the injection protocol found to be best in balancing toxic side effects and MRI contrast enhancement in Study I. For the accumulation process a linear model was fitted, while for the clearance study an exponential one phase decay was used. Using these models, an exploratory investigation was performed, probing no defined hypotheses.

Study III (Application of MEMRI in a mouse model of extremes in trait anxiety) examined the application of a fractionated MEMRI injection protocol on HAB, NAB and LAB animals under basal conditions to study the feasibility of MEMRI as functional imaging tool on a mouse model of trait anxiety. Hypothesis-free whole brain analysis was applied to identify neurocircuitries of anxiety. Histological staining for CO activity was performed to verify results derived from MEMRI measurements.

The following chapter is divided into two parts: the general methods, which

were used for all the studies, and study specific methods. General methods include the MRI acquisition procedure as well as data analysis methods. Although regions of interest (ROI) analysis was not conducted in every study, it will be explained in the general methods part, due to its similarity to the brain extraction step.

All experimental procedures were approved by the Committees on animal health and care of the local government (Regierunspräsidium Oberbayern), and were carried out in accordance with the European Communities Council directive of 24 November 1986 (86/609/EEC).

2.1 General methods

2.1.1 MRI data acquisition

2.1.1.1 Scanning procedure in mice

All MRI experiments were performed on a 7T Avance Biospec 70/30 scanner (Bruker BioSpin, Ettlingen, Germany). During the procedure animals were anesthetized with isoflurane (DeltaSelect, Germany) and fixed in a prone position to a saddle-shaped receive-only coil. Mice were further kept under inhalation anesthesia with an isoflurane-oxygen mixture (1.5-1.9 vol% with oxygen flow of 1.2-1.4 l/min). Head movements were prevented by stereotaxic bedding and fixation of the frontal teeth with a surgical fiber. The body temperature was monitored with a rectal thermometer (Thermalert TH-5, Physitemp Instruments, USA) and kept between 34°C and 36°C using a heating pad. Heart rate was continuously monitored using a plethysmographic pulse oxymeter (Nonin 8600V, Nonin Medical Inc., USA).

T_1- and T_2-weighted (T1w and T2w, respectively) images were acquired with the following parameters:

T1w images

Dorman et al. [159] showed that longitudinal relaxation rates $R_1(=1/T_1)$ as determined by MEMRI can reliably be used to estimate regional brain concentrations. In the presented study, high-resolution 3D T1w images were acquired using fast gradient echo imaging. Aiming at high spatial resolution, no quantitative T_1-mapping was performed. Considering the previously reported variation in T_1-relaxation times after Mn^{2+} accumulation [160, 98], changes in T1w image intensities are expected to show a linear dependency on R_1. For a given flip angle α, the longitudinal magnetization in the steady state (ss) is given by:

$$M_{ss} = \frac{M_0(1 - exp(-\frac{T_R}{T_1}))}{1 - cos(\alpha)exp(-\frac{T_R}{T_1})} \tag{2.1}$$

For $T_R \ll T_1$, Taylor expansion of the exponential function neglecting higher order contributions, show that

$$M_{ss} = \frac{M_0 T_R/T_1}{1 - cos(\alpha)(1 - (T_R/T_1))} = \frac{M_0 T_R R_1}{1 - cos(\alpha) + cos(\alpha)T_R R_1} \tag{2.2}$$

Assuming a minimum T_1-relaxation time in the order of approximately 500 ms for brain tissue at 7T [95, 160, 98] after the application of amounts of Mn^{2+} as used in this work the R_1 dependency of the denominator can be neglected for T_R=50 ms and $\alpha = 65°$, as used for T1w imaging in this work, since $cos(\alpha) \cdot T_R = cos(65°) \cdot T_R \cdot R_1 < 0.042$, and a linear dependency of the steady state magnetization on R_1 in T1w images may be assumed.

T1w images were obtained using different protocols. MRI data for studies I and III were acquired using protocol number 1. Data for study II was obtained using protocol number 2 or 3:

1. T_R/T_E = 50/3.2 ms, matrix size MS =128 × 106 × 106 zero filled to

128 × 128 × 128, field of view (FOV)=16 × 16 × 18 mm^3, number of averages (NoA)=10, Bandwidth (BW)=100000.

2. T_R/T_E = 50/4.4 ms, MS =128 × 106 × 106 zero filled to 128 × 128 × 128, FOV=16 × 16 × 18 mm^3, NoA=10, BW = 50000, fat suppression = 600 Hz.

3. T_R/T_E = 50/4.4 ms, MS =128 × 106 × 106 zero filled to 128 × 128 × 128, FOV=16 × 16 × 18 mm^3, NoA=10, BW = 50000, fat suppression = none.

Spatial resolution was 125 × 125 × 140.6 μm^3. The duration of the measurement were 1 hour and 33 minutes in both protocols. The different protocols will further be addressed as T_1w_1, T_1w_2 and T_1w_3.

T2w images

T_2-weighted images were obtained using a 3D RARE (see section 1.1.2.9) sequence with the following parameters: T_R/T_E = 1000/10 ms, MS =128 × 112 × 112 zero filled to 128 × 128 × 128, FOV=16 × 16 × 18 mm^3, NoA=2, RARE factor = 16 resulting in a spatial resolution of 125 × 125 × 140.6 μm^3, BW = 100000 Hz. Duration of the measurement was 30 minutes.

2.1.2 MRI data analysis

All data analysis methods in this work were performed using SPM software (www.fil.ion.ucl.ac.uk/spm). All images underwent the steps explained in the following two sections 2.1.2.1 and 2.1.2.2. Depending on the study, images were then analyzed using ROI analysis (Study I and partly Study II)(section 2.1.2.3), voxel-wise curve fitting (Study II) or voxel-wise statistical comparisons (Study III). Voxel-wise curve fitting was conducted using programs written in Matlab.

2.1.2.1 Initial processing

All acquired images were reconstructed using the Paravision software from Bruker (Bruker BioSpin, Ettlingen, Germany) and transferred to standard ANALYZE data format. To correct for slight differences in the positioning of the animals T1w and T2w images were roughly reoriented. Images were then co-registered using affine transformations, consisting of rotations and translations. The intensity gradient, introduced by the geometry of the surface coil was removed by bias correction. The effect of bias correction can be viewed in figure 2.1, which shows an image without (left) and an image with (right) bias correction. Parameters were chosen thus that contrast between tissues was preserved.

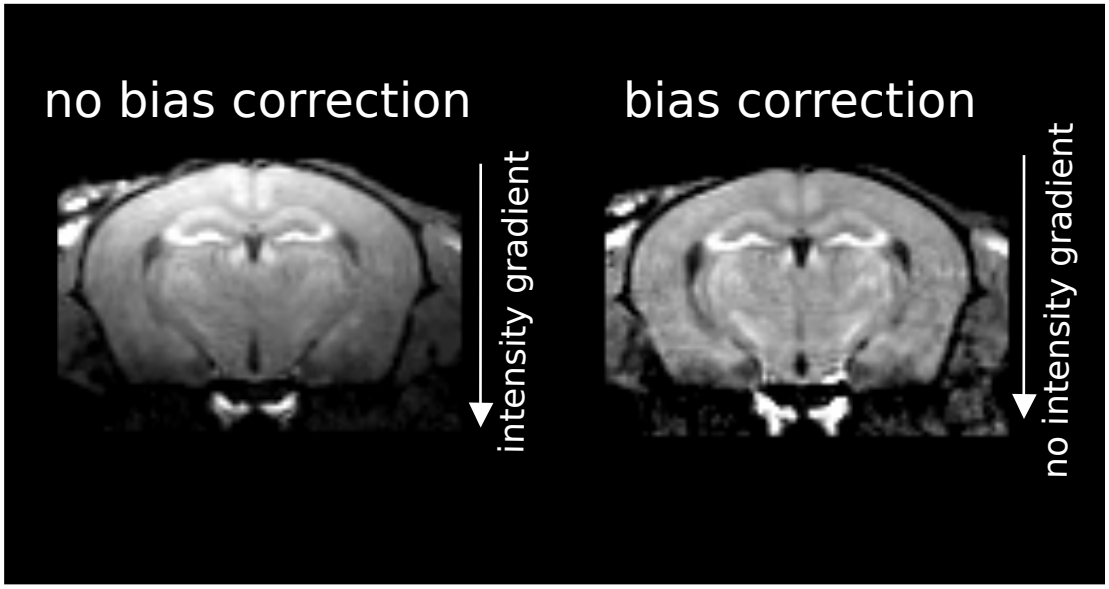

Figure 2.1: Bias correction. Acquired image before (left) and after (right) bias correction. The intensity gradient introduced by the geometry of the surface coil is removed through bias correction. The parameters of the bias correction are chosen thus that contrast between tissues was preserved.

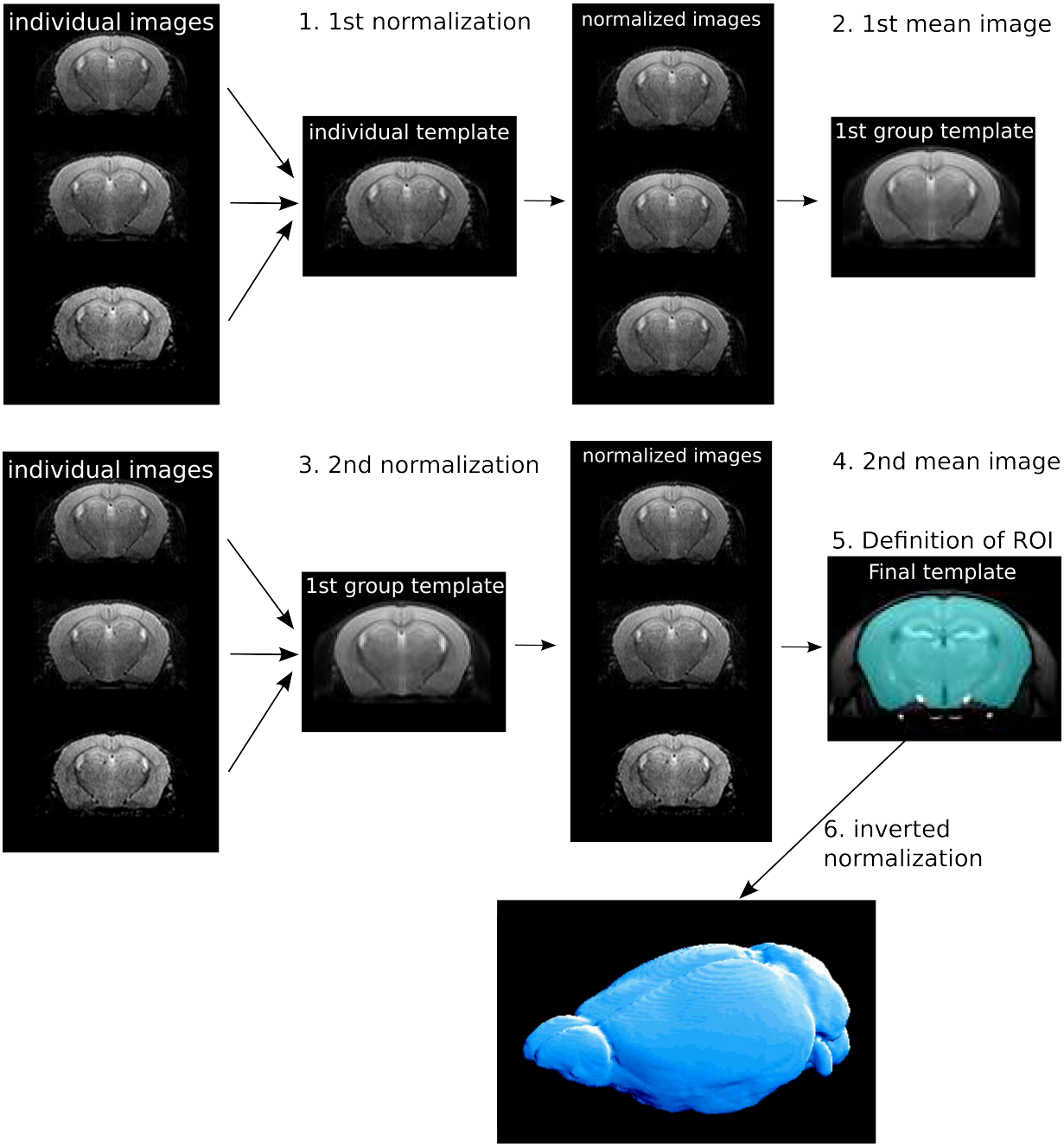

Figure 2.2: Brain extraction. Original T2w images were first normalized to a representative T2w image of an individual mouse (1). The mean image of the normalized images served as a second template (2). The original T2w images were normalized again to this first group template (3) and a the resulting normalized images were averaged again to create a second group template (4). To ensure the exclusion of hyper-intense vessels the normalization steps of the second normalization was also written on the T1w images to create a T1w group template, on which the ROI was defined (5). This whole brain ROI was finally transformed back by inverted spatial normalization to the anatomy of every single mouse brain (6).

2.1.2.2 Brain extraction

Due to the fact that the brain intensity of T2w images is more uniform within the brain and the brain is silhouetted against non-brain structures, these images were normalized first to a representative T2w image to define brain borders. Normalization parameters were chosen so that original intensities in the whole brain were not altered. The mean image of these normalized images was taken as second template. The mean was taken as a final normalization template to ensure the inclusion of all images of the study into the template to generalize the normalization step. The normalization field generated during the T2-normalization step was eventually written on both the T1w and the T2w images. Finally, a mean of the normalized T1w images (ROI template) was taken. This mean image was used for the definition of the ROI, in this case, the whole brain. A ROI including all brain structures, except for blood vessels was defined manually on the ROI template. The use of SPM enables the inversion of the normalization fields. This feature is exploited to back-deform the whole brain mask to fit on the primary individual bias corrected brain images. The interpolation, which is needed for the back deformation step, converts the original binary brainmask into a non-binary brainmask. The application of a non-binary brainmask for brain extraction would result in a corruption of the intensity values of the images. It is therefore necessary to apply an intensity cutoff to ensure a binary format of the brainmask. The intensity threshold was set at a minimum of 60 and a maximum of 254 (with original image intensities varying between 0 and 254 grey levels). The resulting ROIs were then used to remove all non-brain structures on the primary reoriented, co-registered and bias corrected image. Figure 2.2 shows a graphical display of the pipeline for clarification purposes.

2.1.2.3 Region of interest analysis

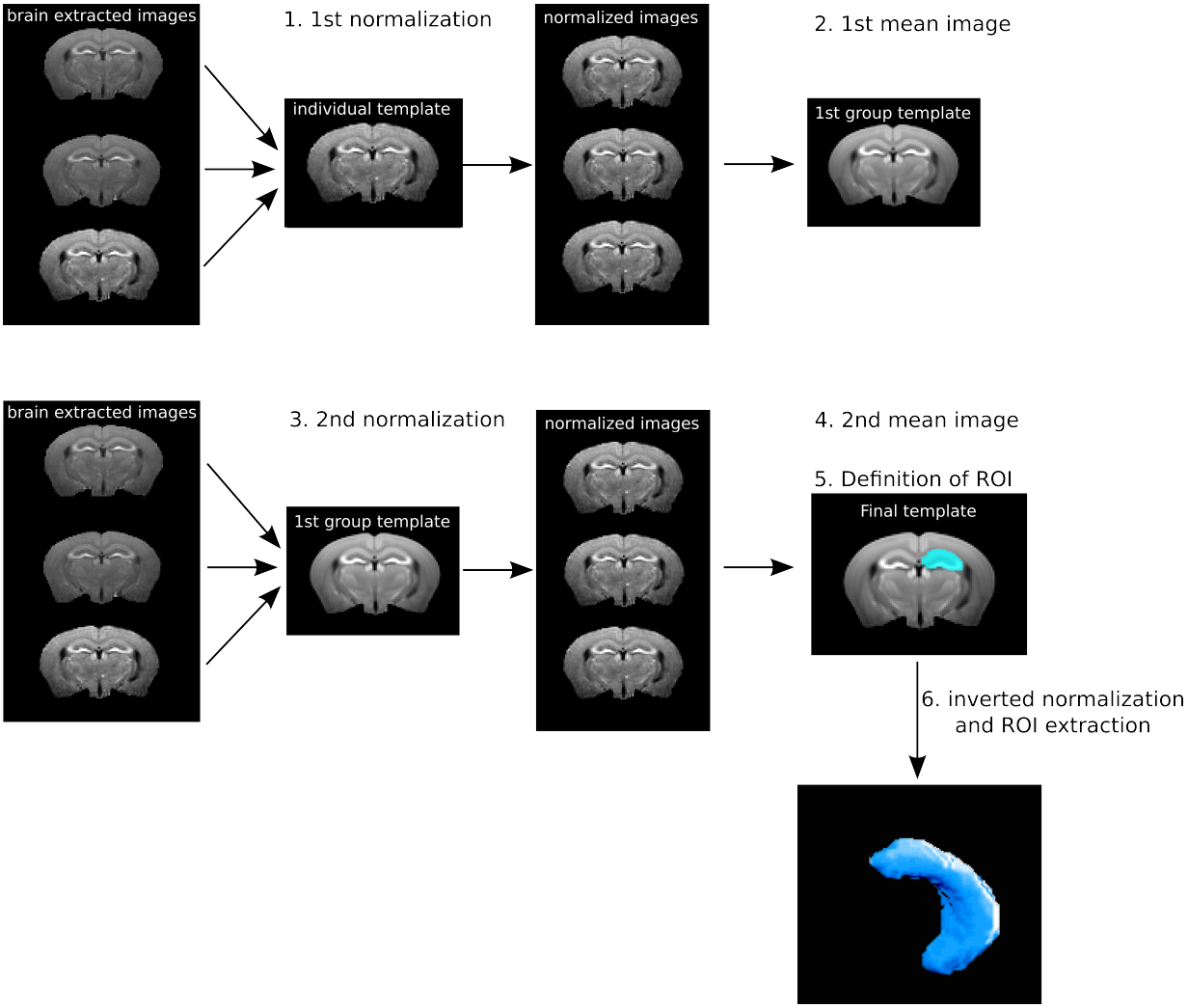

Figure 2.3: ROI extraction. T1w brain extracted images were normalized to the same individual template as in the brain extraction step (1). A first group template was created by averaging the normalized images (2). T1w brain extracted images were normalized to the first group template (3) and a second group template was generated by averaging the normalized images (4). The ROI was defined on the second group template ((5) HPC is shown as example). The ROI was transformed back to the anatomy of each individual mouse brain through inverted spatial normalization (6).

ROI extraction is done similar to brain extraction. However, for improved inner brain normalization, brain extracted T1w images are used, instead of T2w images. The T1w images exhibit regional signal intensity differences.

Hyper-intense regions, such as the HPC, serve as 'landmarks' for spatial normalization and enable the normalization procedure of SPM during which the enhanced regions were accurately fit to one another. Thus, defining the ROIs on a template image and back deforming them to their original space allows for an automatic discrimination of the structure. In detail the extraction of the desired ROI was as follows:

The whole brain T1w images were spatially normalized to the T1w image of the representative animal of section 2.1.2.2. The mean of these normalized images was used as template image for the second normalization step. The mean of these normalized images (whole brain template) was taken to outline the ROI. The region mask was back deformed with the inverted normalization of the second normalization step as in section 2.1.2.2 for each individual animal. Figure 2.3 shows a graphical scheme of the region of interest analysis. Since the HPC is one of the biggest regions and very well outlined in MEMRI images, it was chosen as an example region.

2.1.2.4 Graphical display of data

All data is graphically displayed in GraphPad 4.0 as mean± standard error of the mean (SEM), unless otherwise noted.

2.2 Study dependent methods

2.2.1 Study I: Fractionated MEMRI

2.2.1.1 Animals and application of Mn^{2+}

A solution of 50 mM $MnCl_2 \cdot 4H_2O$ (Sigma, Germany) in 0.9% NaCl was prepared. pH value of the solution was adjusted to 7.0 using HCl and NaOH. All injections were administered ip. The study was carried out on C57BL6/N

(BL6) mice, a strain commonly used for creating gene knockout animals.

A total of 42 animals was used for the study. 24 animals were used to investigate behavior and general health status as well as endocrine response of the animals during manganese application. 18 animals were used to investigate the development of body temperature and locomotion over the course of manganese application. For endocrine measurements and assessment of general health status, animals were randomly assigned to one out of four groups containing six animals per group: The first group received three injections of 60 mg/kg of the solution with an inter-injection interval of 48 hours (referred to as $3 \times 60/48$). Group number 2 received 8 injections of 30 mg/kg of the solution with an inter-injection interval of 24 hours (hereafter referred to as $8 \times 30/24$). The third group received a single injection of 99 mg/kg of the solution (1×99). As the first two animals of group 3 showed severe side effects on Mn^{2+} shortly after the injection and had to be sacrificed, the 1×99 group was changed for the remaining animals to 6 injections of 30 mg/kg with an inter-injection interval of 48 hours (further referred to as $6 \times 30/48$). Group number 4 served as a control group, receiving three injections of 0.06 ml/10 g of 0.9% NaCl every 48 hours (figure 2.4). Animals for body temperature and locomotion measurements were randomly assigned to group $3 \times 60/48$, $8 \times 30/24$ and $6 \times 30/24$ with 6 animals per group. To account for the circadian rhythm of corticosterone secretion, injections were always given in the beginning of the dark phase of the mice. After each injection animals were returned to their home cage.

2.2.1.2 Endocrine measurements

To investigate the activation of the HPA-axis in response to the different $MnCl_2 \cdot 4H_2O$ application schemes, corticosterone levels were measured 4 hours and 12 hours after the first Mn^{2+}-injection (denoted as d1/4h and

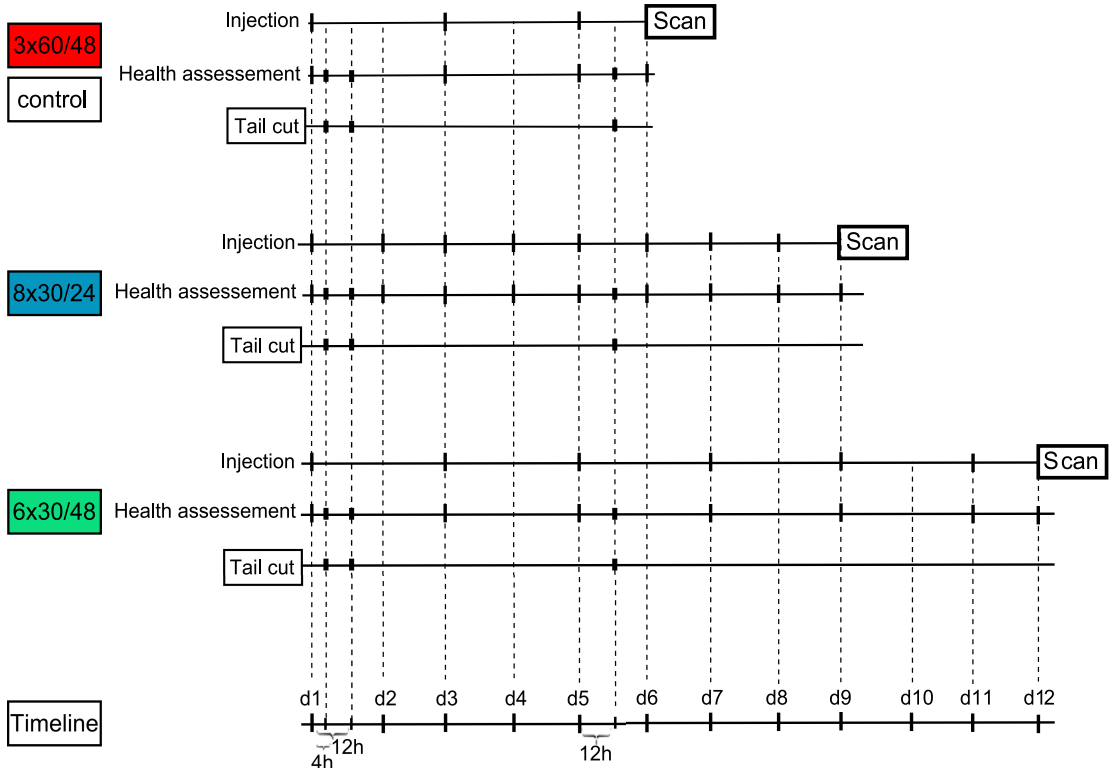

Figure 2.4: Experimental timeline. Experimental timeline of application schemes, health assessment, and corticosterone measurements (tail cut). The timepoint of MR imaging is also indicated. Control animals are treated according to the $3 \times 60/48$ scheme.

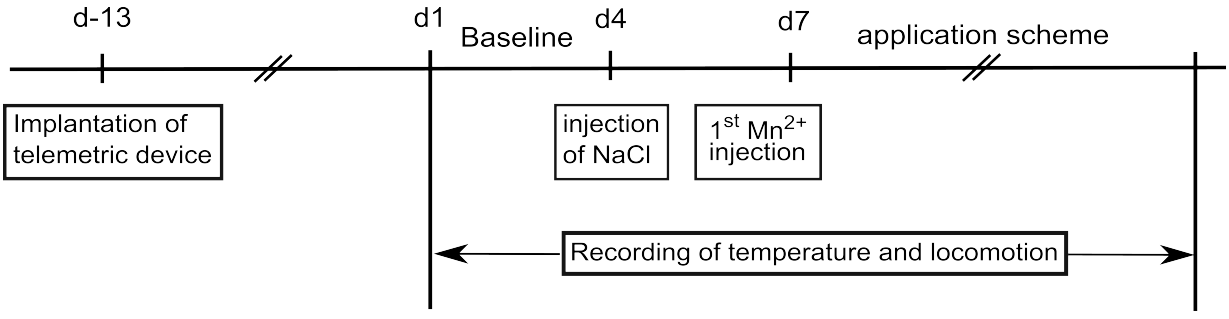

Figure 2.5: Experimental schedule of telemetric measurements. After implantation of the telemetric device animals were allowed two weeks of recovery after which a three day baseline recording started. An injection of saline was applied three days before the Mn^{2+} injection protocols were started.

d1/12h respectively) and on day five 12 hours after the Mn^{2+}-injection (figure 2.4). Blood samples were collected via tail cut in capillary tubes containing ethylenediaminetetraacetic acid (EDTA, Kabe Labortechnik, Germany) to prevent clotting. Samples were kept on ice until centrifuging (8000 rpm, 15 min, 4°C), after which plasma was subtracted and stored at -20°C. Plasma corticosterone measurements were performed using an ImmuChem Double Antibody Corticosterone ^{125}I Radioimmunoassay kit (MP Biomedicals, Eschwege, Germany) with a minimal detectable corticosterone concentration of 7.7 ng/ml. The coefficients for intra-assay and inter-assay variation were 7.3% and 6.9%, respectively.

2.2.1.3 Body temperature and locomotion

Body temperature and locomotion were assessed using telemetric devices, which were implanted at least 14 days before the starting of recording (Figure 2.5). For the implantation procedure, mice were anesthetized using a combination of ketamine/xylazine (50 mg/kg ketamine (Essex Pharma GmbH, Germany) + 5 mg/kg xylazinhydrochloride (Rompun, Bayer health care, Germany)). The transponders were purified and sterilized using benzalchonium chloride (Sigma, Germany), repeatedly flushed with sterile 0.9% NaCl and inserted into the abdominal cavity of the animals. The wound was disinfected with Braunol (Braun AG, Melsungen, Germany). For analgesia, 0.5 mg/kg Metacam (Vetmedica GmbH, Boehringer Ingelheim, Germany) was injected subcutaneously directly after surgery. The animals were given a recovery period of 14 days. Due to technical problems and subsequent acquisition errors, three animals had to be excluded resulting in the following group sizes: four animals for the $6 \times 30/48$, five for the $8 \times 30/24$ and six for the $6 \times 30/24$ group. Over the course of the corresponding injection protocol the development of body temperature and locomotion was measured using the Dataquest

LabPRO (Data Sciences International, Version 3.11, USA, Minnesota) acquisition system. Locomotion is displayed as activity counts for the period of interest. The activity counts depend strictly on the distance the animal moves horizontally with a velocity above 1 cm/s. After two weeks of recovery from the implantation procedure a three-day baseline was recorded. As body temperature and locomotion follow a circadian rhythm deviations of these measures from a mean of the three-day baseline recording was calculated. As control measurement body temperature and locomotion response to a single NaCl injection (0.1 ml/10g) three days before initiation of the Mn^{2+} injection protocol were acquired. For data analysis temperature and locomotion measurements were averaged for bins of 30 minutes for each animal.

2.2.1.4 Health assessment

Behavior and general health status of the animals were assessed after each injection and prior to each blood collection (Figure 2.4). Measures included body weight, body position, tremor, palpebral closure, coat appearance, whiskers, lacrimation, defecation, gait and tail elevation. All measures were assessed according to the European Mouse Phenotyping Resource of Standardized Screens guidelines (EMPRESS, http://empress.har.mrc.ac.uk). The measures of interest were recorded in a "viewing arena", which was in our case a standard Makrolon type IV cage. After injections animals were placed into the viewing arena. Without disturbing the mouse measures were collected due to the assignments of EMPRESS:

Body position: Observe the mouse and identify whether it appears to be inactive, active or excessively active (scoring: inactive=0, active=1, excessively active=2)

Tremor: Make a note of whether or not the mouse appears to tremble (scoring: absent=0, present=1)

Palpebral closure: Study the mouse for palpebral closure (scoring: eyes open=0, eyes closed=1)

Coat appearance: Look carefully at the mouse coat and determine how tidy and well groomed it is, making a note of any deviances (scoring: tidy and well groomed coat=0, irregularities=1)

Whiskers: Make a note of whether the mouse has intact or trimmed whiskers (scoring: present=0, absent=1)

Lacrimation: Make a note of the presence or absence of lacrimation (scoring: absent=0, present=1)

Defecation: Make a note of whether or not the mouse defecates (scoring: present=0, absent=1)

2.2.1.5 ROI analysis

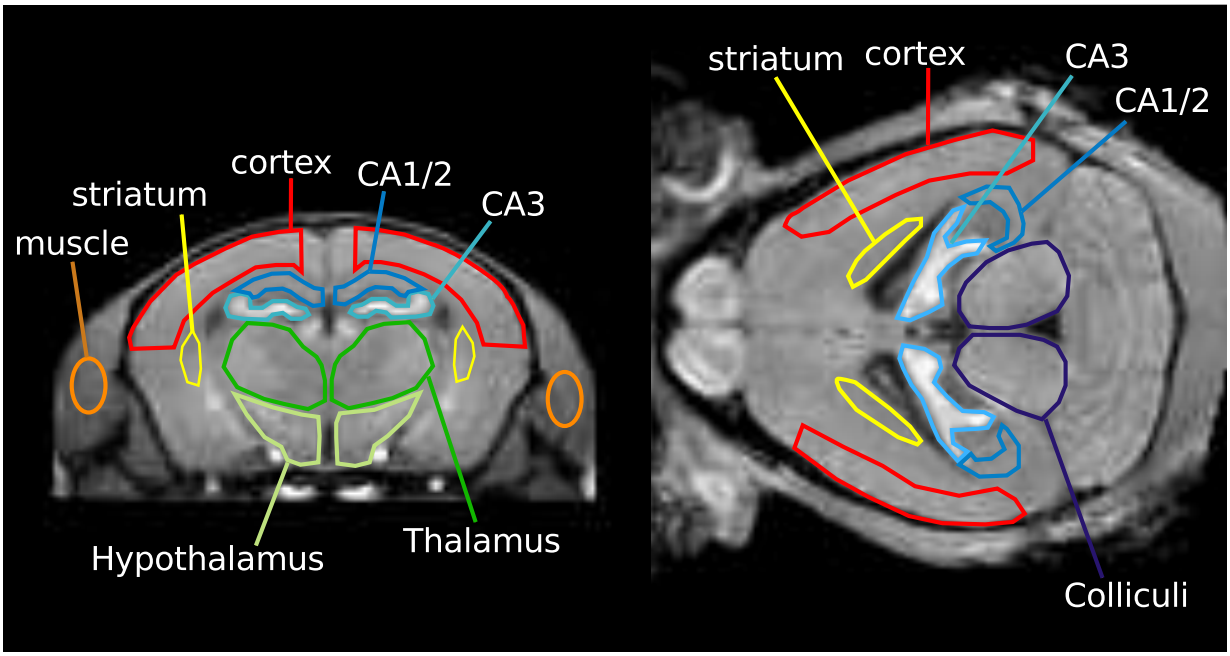

Figure 2.6: ROIs as defined on the T1w group average. ROIs are roughly depicted on a representative coronal (left) and horizontal slice (right). All ROIs were defined on multiple slices and bilaterally, based on the anatomical atlas of BL6 mice by Franklin and Paxinos [161].

ROIs were defined on the T_1w_1 group template for selected structures (fig-

ure 2.6) based on the anatomical atlas of the C57BL/6 mouse by Paxinos and Franklin [161]. The bilateral inferior colliculi (IC), CA1/2 and CA3 regions of the HPC, the caudate putamen (CPU), the Th and HTh, and parts of the cortex were defined as ROIs. Furthermore the whole brain (wb) served as ROI. As a measure of global signal intensity an area of the muscle surrounding the skull was defined.

Signal intensities were measured using in-house written software in interactive data language (IDL, www.cresao.com).

2.2.1.6 Visualization of fine structures

To visualize the capacity of the fractionated application schemes to resolve cerebral fine structures, such as cortical layers, the original image matrix size of 128×128 does not provide sufficient resolution. Therefore, representative images of each group were reprocessed to an image matrix size of $256 \times 256 \times 256$ with subsequent bias correction. The zero filling leads to truncation artifacts ('Gibbs ringing') on coronal sections which hamper precise evaluation of cortical layer structures, especially parallel to the skull surface. Therefore, only the retrosplenial granular cortex (RSG) was evaluated, since it runs perpendicular to the skull surface.

2.2.1.7 Statistical analyses

Data resulting from endocrine secretion was analyzed using a one-way analysis of variance (ANOVA) to compare corticosterone levels between groups at different time points.

For temperature and locomotion, grand means over all injection timepoints were calculated. These values were submitted to one-way ANOVA to examine the effect of the application scheme. Repeated measurements ANOVA was

applied to each application scheme separately to explore the development of temperature and locomotion drops over time.

Body weights were compared using repeated measurements ANOVA for day 1, day 3 and day 5. Least significant difference (LSD) post-hoc test was applied, whenever necessary.

Calculated mean intensities within the ROIs were divided by the animals mean intensity of the muscle ROI. In the following, normalized values are referred to as relative intensities (RI). Besides the separate ROIs, an average RI over all ROIs combined excluding whole brain and muscle was calculated, which will be referred to as cortical and subcortical (c+sc) RI. We analyzed the data using one-way, two way and repeated measurements ANOVA with SPSS 16.0. Statistica 5.0 was used to conduct pair-wise post-hoc comparisons. To investigate the effect of the application scheme on the wb and c+sc RI values one way ANOVA was employed. To explore region×group effects that would indicate different contrast across regions depending on the application scheme, two-way ANOVA was applied with factors group (4-levels) and region (7-levels). To determine if application schemes produced distinct between-region contrast differences two analyses were performed: first, LSD post-hoc tests of the interregional differences per group were reviewed and nominally significant pair wise differences were counted per group. Second, the coefficient of variation (COV) was determined across regional RIs and correlated with the total dosage of applied $MnCl_2 \cdot 4H_2O$, based on the assumption that both mean intensity and interregional differences can be enhanced using Mn^{2+}. The COV is defined as the ratio of standard deviation σ to the absolute value of the mean μ:

$$COV = \frac{\sigma}{\mu} \tag{2.3}$$

Correlation was determined by using the Spearman rank correlation test. Sig-

nificance was accepted if $p<0.05$.

2.2.2 Study II: Dynamical behavior of manganese in the $8 \times 30/24$ injection protocol

2.2.2.1 Animals and application of Mn^{2+}

Accumulation of Mn^{2+}

For measuring the dynamics of the accumulation of Mn^{2+} of the $8 \times 30/24$ protocol, 80 animals were randomly assigned to one of 8 groups with 10 animals per group. The same $MnCl_2$ solution as described in section 2.2.1.1 was used for delivering Mn^{2+} to the brain. Group 1 received one ip injection of 30 mg/kg $MnCl_2 \cdot 4H_2O$ and was measured 24 hours after this injection. Group 2 received two ip injections of 30 mg/kg $MnCl_2 \cdot 4H_2O$ and was measured 24 hours after the last injection. This procedure was repeated for group 3 to 8 with animals of the groups receiving numbers of injections correspondingly to their group number and an MRI scan 24 hours after the last injection (figure 2.7). Due to technical problems or death of animals additional animals were used. Therefore final group sizes were: $n_1 = 12$, $n_2 = 9$, $n_3 = 11$, $n_4 = 11$, $n_5 = 9$, $n_6 = 8$, $n_7 = 8$, $n_8 = 8$. Furthermore, 9 control animals were measured without receiving any injection. T_1w_2 images were acquired.

Clearance of Mn^{2+}

For measuring the dynamics of the clearance of Mn^{2+} five different time points after the first scan were chosen to perform a second scan: 1 week, 2 weeks, 4 weeks, 8 weeks and 12 weeks (figure 2.8). Fifty animals were randomly assigned to one out of these five groups with ten animals per group. All animals were treated with the $8 \times 30/24$ injection protocol and scanned 24 hours after the last injection. Group 1 was scanned a second time 1 week after

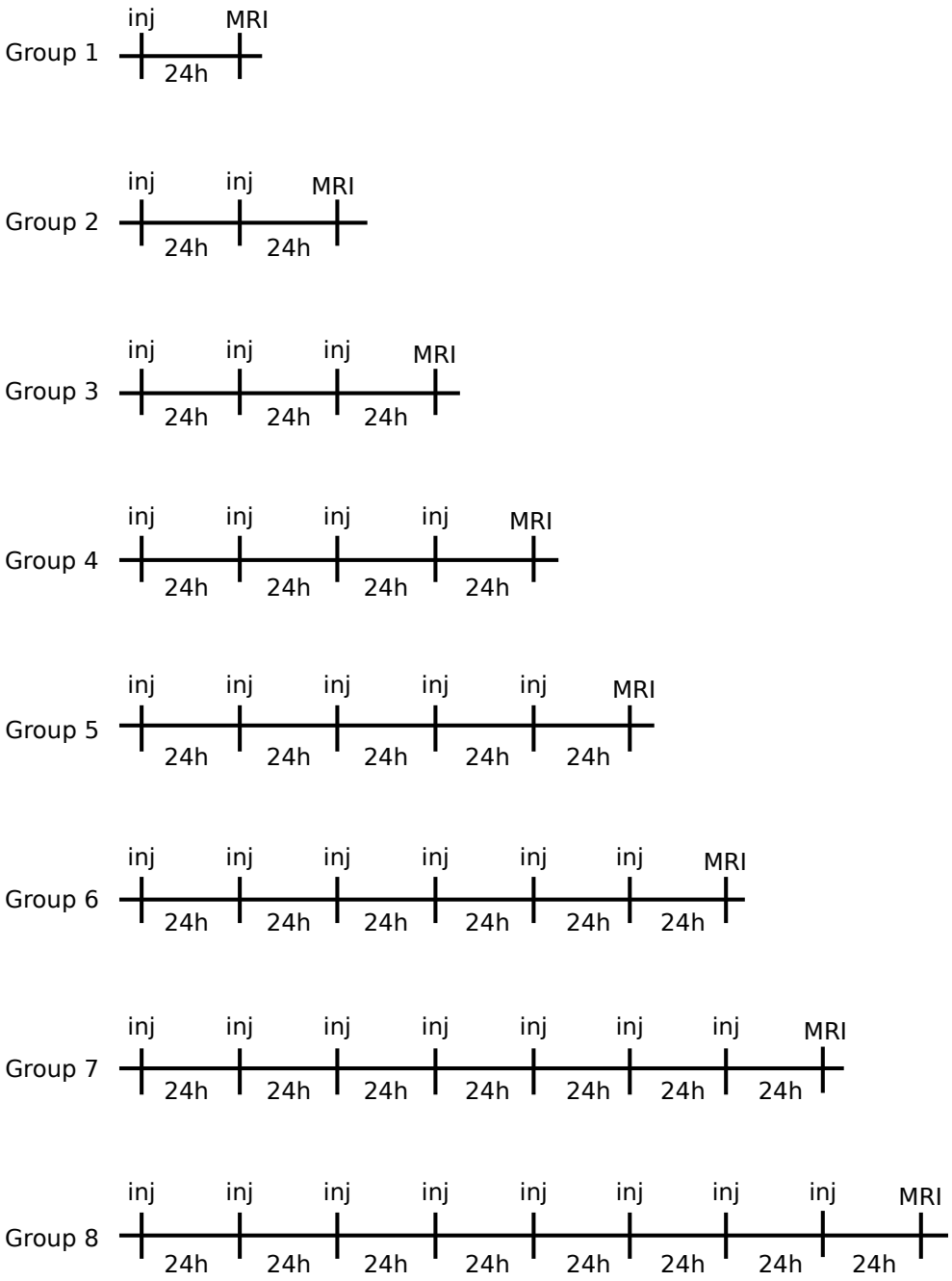

Figure 2.7: Experimental timeline of the accumulation experiment. Groups received number of injections according to their group number. Animals were scanned 24 hours after their last injection. As the control group did not receive any injection, but was only scanned, it is not specified in the graphic.

the first scan, group 2 two weeks after the first scan and so on (figure 2.8). Due to technical problems or death of animal before the second scan the final group sizes amounted to: $n_0 = 45$ $n_1 = 8$, $n_2 = 10$, $n_4 = 9$, $n_8 = 9$, and $n_{12} = 6$. T_1w_3-images were acquired, thus comparison with control animals from the accumulation study was not possible. Therefore, animals of time point 12 were used as control condition.

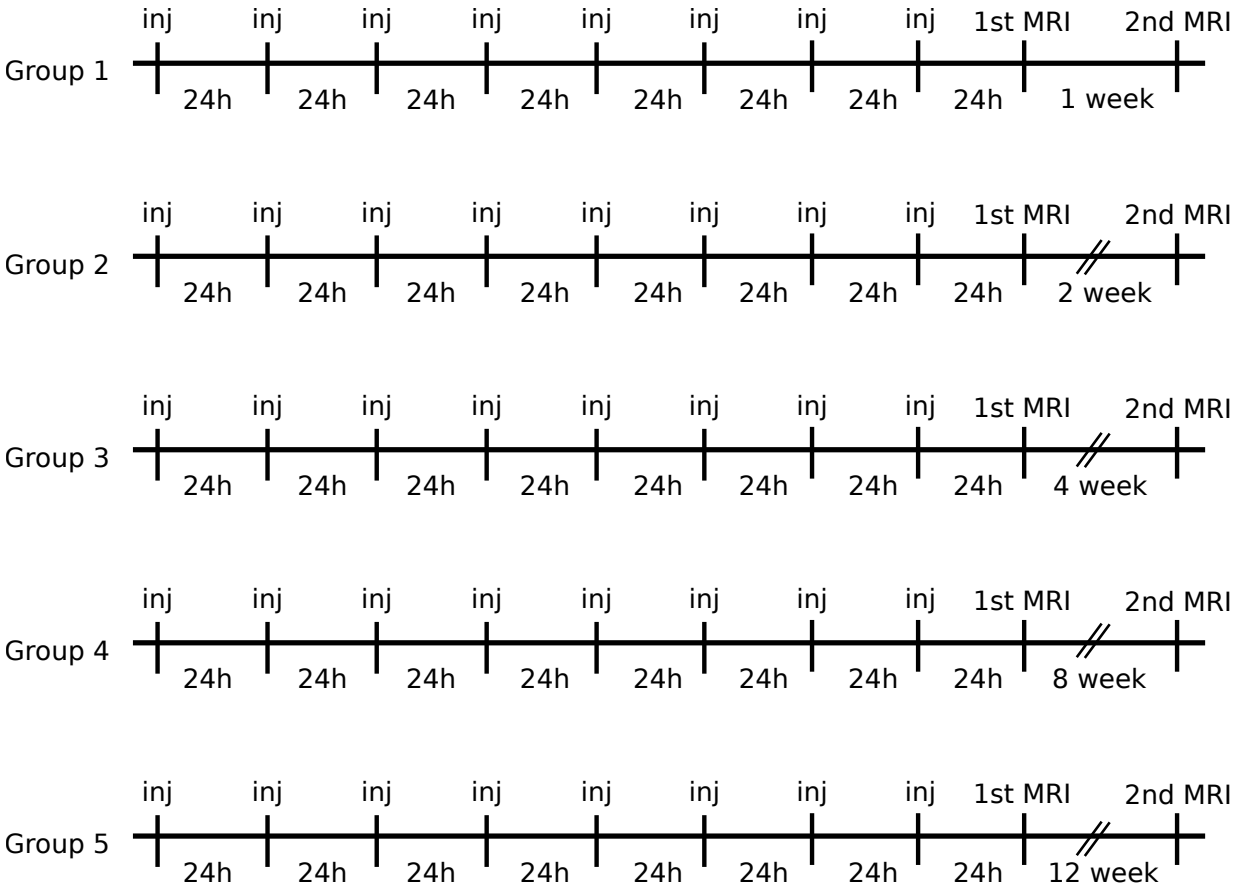

Figure 2.8: Experimental timeline of the clearance experiment. All groups received the entire injection protocol. All animals were scanned 24 hours after the last injection. Group 1-5 were measured in the MR scanner a second time 1 week, 2, 4, 8 and 12 weeks after the first measurement, respectively.

2.2.2.2 MRI data analysis

As a measure of global signal intensity the parts of the muscle surrounding the brain (figure 2.9) was defined. The extracted signal intensities of this area were taken to correct brain extracted, spatially normalized whole brain images on a voxel-by-voxel basis. Images were smoothed by a $250 \times 250 \times 281.2\mu m^3$ Gaussian kernel at full width half maximum. Normalized intensities will be referred to as RIs.

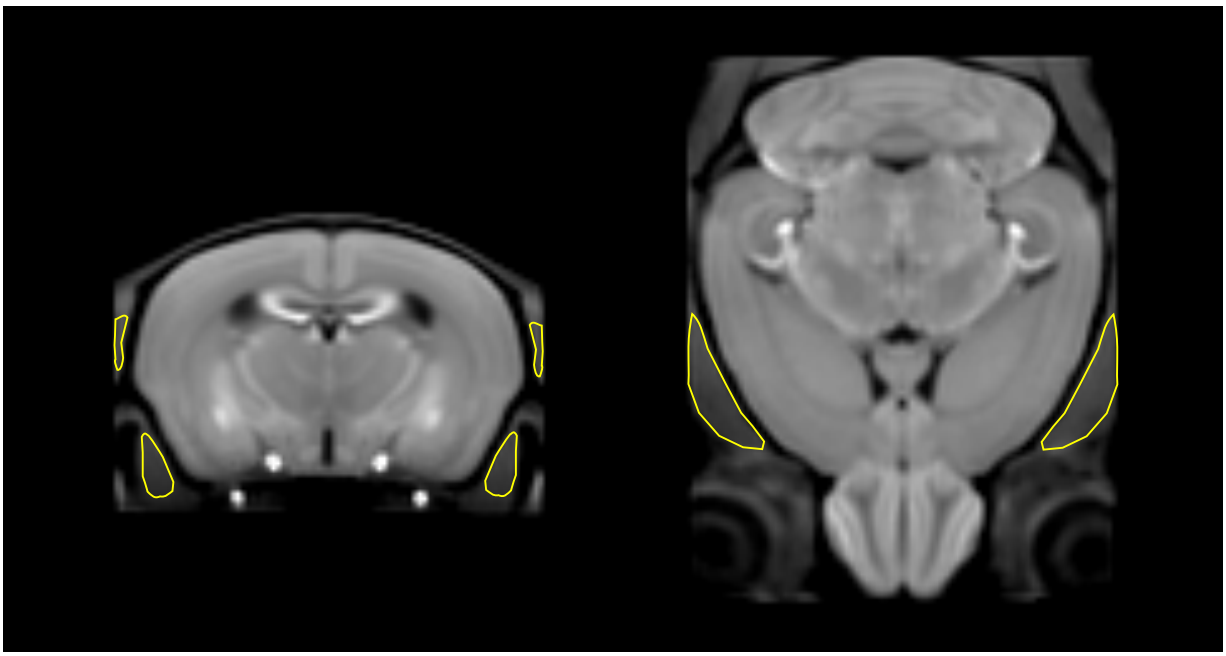

Figure 2.9: Definition of muscle. The defined area (yellow) was used to correct images for intensity in a coronal (A) and horizontal (B) section.

Accumulation of Mn^{2+}

Because of the assumption that the accumulation of Mn^{2+} is a linear increasing process a linear regression was fitted on a voxel-by-voxel basis. This was done by fitting

$$y = mx + b$$

where m denotes the slope, and b the intercept of the y axis, to every voxel separately. The result was a colour coded map with the slope of the fitted line and the correlation coefficient r^2. Further, a map with p-values was calculated to test for significance of the regression. α-level was set at 0.05. The analysis was performed using in-house written Matlab software.

Clearance of Mn^{2+}

Because of the assumption that the clearance process is an exponential decay, a one phase decay model was fitted to the data. As the exponential decay of RIs does not approach zero, but the value of native contrast, the fit resembled a three parameter fit which could not be linearized. To determine the half life of RIs after the $8 \times 30/24$ protocol the following function was fitted to the data on a voxel-by-voxel basis:

$$\mathrm{RI(t)} = \mathrm{RI_0} exp(-\lambda t) + c \tag{2.4}$$

with $\mathrm{RI_0}$ denoting the RI at time zero (24 hours after the last injection), λ designating the rate constant in 1/weeks, and c denoting the offset from zero. The half-life τ was calculated by:

$$\tau = \ln 2/\lambda \tag{2.5}$$

To estimate the goodness of fit, r^2-values and half-lives resulting from upper and lower boundaries of the 95% confidence interval (CI), were calculated. Fitting was performed with in house written Matlab software.

2.2.2.3 ROI analysis

To get a quantitative impression on slopes and half-lives of different regions, a ROI analysis was performed on the obtained maps. ROIs were defined as

shown in figure 2.10. Due to the chosen resolution, a clear differentiation between the brain structures was not possible. Therefore, ROIs denote a rough delineation of the different brain regions, which were chosen according to the anatomical mouse brain atlas of Franklin and Paxinos [161] and the differences in contrast enhancement on the mean T1w image of the study, which was used for delineation of the ROIs. Furthermore, the division in subparts of brain regions such as for different thalamic nuclei, or other parts of the brain, is impossible on the basis of MEMRI contrast. The images to the right of the MR images in figure 2.10 are taken from the mouse brain atlas of Franklin and Paxinos [161]. Chosen ROIs are coloured according to the ROIs on the MR image. These images indicate that most ROIs contain more subregions, which cannot be differentiated in the MR image. These regions were therefore taken together to one big region. Since the mean image of the study is composed of the normalized images, which also underlie the map of slope, half-life and corresponding r^2, the defined ROIs are applicable to the maps to extract region specific values of these parameters.

2.2.2.4 Statistical analysis

To explore interaction effects of either number of injections (accumulation process) or weeks after injection (clearance process) with the RI of the 21 different ROIs, two-way ANOVA was applied with factors number of injection (9 levels) and ROI (21 levels) for the accumulation process or factors weeks after injection (6 levels) and ROI (21 levels) for the clearance process.

To be able to account for unequal variances post-hoc testing was performed using independent sample T-tests. 6 chosen ROIs were investigated on whether an additional injection would lead to significantly higher RI and to find the number of injection which first led to significantly higher RI than control level. Independent sample T-tests were further used to investigate at

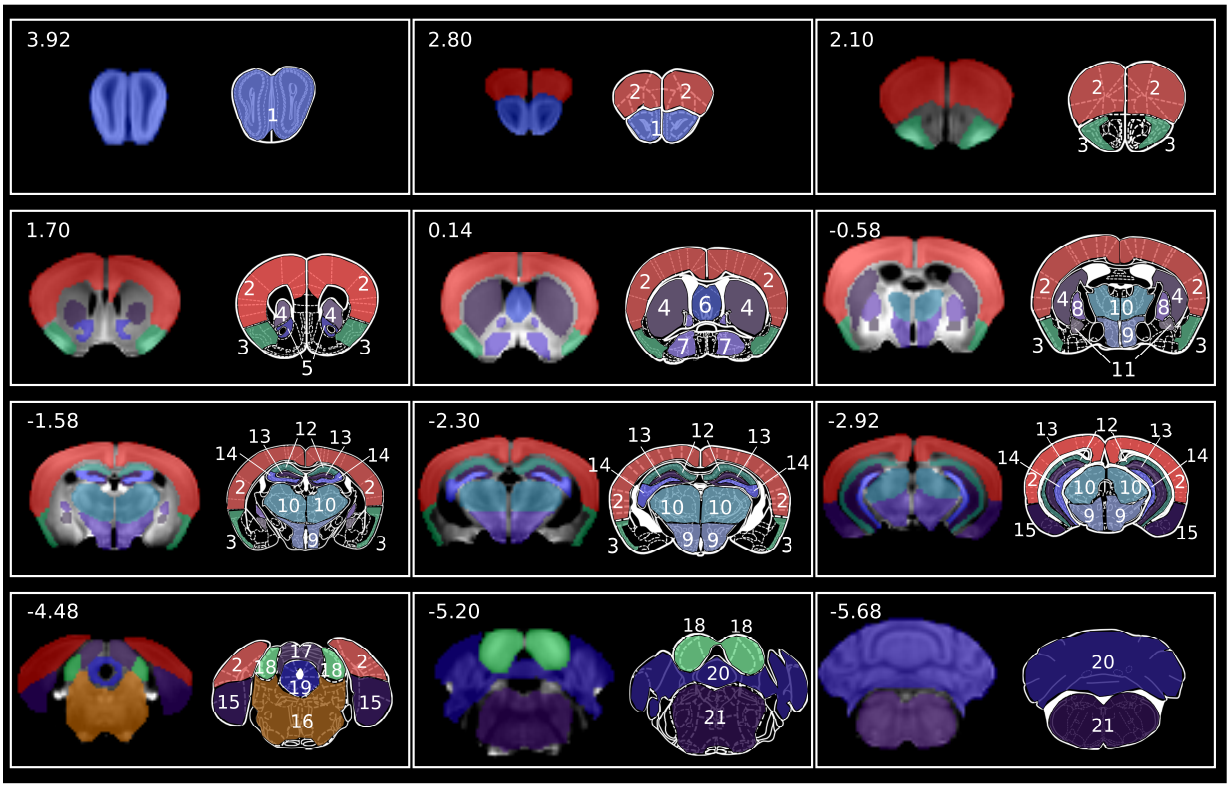

Figure 2.10: Atlas of different ROIs as used for the study. ROIs as used for the determination of slope and half lives and corresponding goodness of fit. It has to be noted that a clear differentiation between the different structures is not possible. ROIs are therefore rough delineations of the brain regions. Regions were mainly chosen due to different signal intensities in the image. Images to the right of MR images are taken from the mouse brain atlas of Franklin and Paxinos [161], and regions are coloured according to the regions chosen on the MR images. 1: olfactory bulb (OB), 2: cortex, 3: piriform cortex (PC), 4: caudate putamen (CPU), 5: nucleus accumbens (Nacc), 6: septum, 7: bed nucleus of the stria terminalis plus ventral pallidum (BNST vGP), 8: globus pallidus (GP), 9: hypothalamus (HTh), 10: thalamus (Th), 11: central nucleus of the amygdala (CeA), 12: CA1/2, 13: dentatus gyratus (DG), 14: CA3, 15: entorhinal cortex (EC), 16: midbrain (MB), 17: superior colliculi (SC), 18: inferior colliculi (IC), 19: periaqueductal gray (PAG), 20: cerebellum (CrB), 21: brain stem (BS). Numbers on the upper left side of each rectangle indicate the coordinate bregma.

what time point after the last injection RIs were at the level of week 12 for the clearance study.

The nominal α-level was set at 0.05. For multiple test correction the nominal α-level was corrected by number of tests, resulting in p_{cor} <0.001 for accumulation and p_{cor} <0.002 for clearance (Bonferroni correction).

To further investigate contrast enhancement the COV was calculated according to equation 2.3. A correlation was calculated by using the Spearman rank correlation test for the accumulation and exponential correlation for the clearance. For the linear correlation significance was accepted if p<0.05.

2.2.3 Study III: Application of MEMRI in a mouse model of extremes in trait anxiety

This study aimed at visualizing the neurocircuitry of anxiety in a mouse model of extremes in trait anxiety. To verify the results gained by hypothesis free MEMRI analysis, staining for CO activity was conducted.

2.2.3.1 Animals and application of Mn^{2+}

All experiments of this study were performed on inbred HAB, NAB, and LAB mice (chapter 1.5.2). The injected $MnCl_2$ solution was the same as in section 2.2.1.1.

A total of 79 animals was used for this study. Group sizes for MRI measurements were: n_{HAB}=19, n_{NAB}=14, and n_{LAB}=16. Although the $8 \times 30/24$ protocol was investigated this far, in this study the $3 \times 60/48$ protocol was applied to reduce handling stress as much as possible. This is necessary to reduce brain activity differences which might arise due to handling stress. Furthermore, HAB, NAB and LAB animals were bred on a CD1 background, which do not react as sensitively to Mn^{2+} as BL6 mice.

Group sizes for histological measurements were: n_{HAB}=8, n_{NAB}=8, and n_{LAB}=8. To consider possible neurotoxic effects of manganese on brain tissue animals used for histological measurements were injected with the same injection protocol as animals used for MRI measurements.

2.2.3.2 Endocrine measurements

To investigate the response of the HPA-axis between the different mouse lines corticosterone levels were measured 1 hours after the first injection (d0/1h), 4 hours after the second injection (d2/4h) and 4 hours after the last injection (d4/4h) of eight animals of each mouse line.

The procedure for measuring corticosterone levels was the same as described in section 2.2.1.2.

2.2.3.3 Voxel-wise statistical comparison

Images were smoothed using a $375 \times 375 \times 421 \mu m^3$ full width at half maximum Gaussian kernel. Second level random effects analyses were performed for statistical inference on the group level. A full factorial model was calculated which included data from HAB, NAB and LAB animals. To correct for unspecific differences in manganese accumulation the extracted whole brain intensities of the normalized smoothed images were added as covariate with interaction in the model. The used design matrix is shown in figure 2.11.

2.2.3.4 Histology

Tissue preparation

For CO staining, brains were removed 24 hours after the last Mn^{2+} injection and shock-frozen in 2d-Methylbutan (Sigma, Germany) on dry ice, wrapped in aluminum foil and stored at -80 °C until further processing. Serial coronal

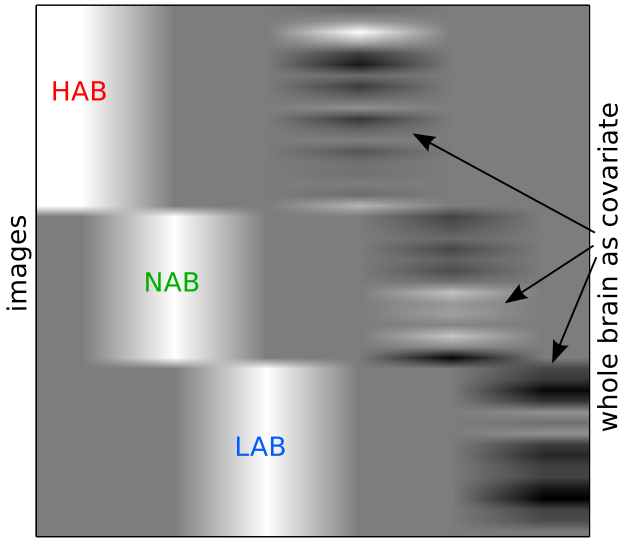

Figure 2.11: Design matrix. Design matrix used in Study III. The first three columns denote the images submitted to the model in the three different group. Columns 4-6 represent the whole brain intensities which were added as a covariate to the model with correcting for interaction effects.

sections of the whole brain were cut on a Cryostat (HM 560 Microm) at -20 °C and mounted onto Superfrost Plus slides. Slides were stored in closed boxes at -80 °C until assayed.

Staining procedure

The tissue was put in acetone for five minutes to affix the slices. To remove red blood cells the slices were put in Na^+ buffer for three times and five minutes each at 4 °C. The CO reaction solution was prepared prior to each staining at 37 °C. It consisted of 45 g sucrose, 390 mg 3.3'-diaminobenzidine (DAB, Sigma D8001), 50 mg CO of the equine heart (Sigma, C2506), 150 g nickel ammonium sulfate (Sigma. A1827) in 1l of a 0.1 M sodium phosphate buffer (PBS). A magnetic stir bar was used to circulate the solution at low speed. The slides were incubated for 20 minutes in the solution. To flush the slices and stop staining, they were washed in Na^+ buffer for three times and five minutes each at 4 °C. At room temperature the slices were fixed for 30

minutes in 4% paraformaldehyde (Sigma, Germany) in 0.1 M PBS. To stop the fixation procedure the slices were again washed in Na^+ buffer twice for five minutes each. The tissue was dehydrated through a graded series of ethanol (70%, 80%, 99%). It was eventually dehydrated using isopropanol for two minutes. Finally, the tissue was coverslipped with HistoKit (Roth T160.1) to avoid bleaching of the slices over time.

Image analysis

Bright field images of CO activity stained mouse brain sections were acquired using a Leica MZ APO microscope, an AxioCam MRc5 camera and Axio Vision Release 4.7. The exposure time was set so that neither saturation nor underexposure of the pixels occurred (t_{exp}=38 ms). 8-bit grayscale images (0-256 gray levels) were captured with a dimension of 1548×1036 pixels and a resolution of $3.5 \times 3.5 \mu m^2$. ROIs were manually defined on the images according to findings of the MEMRI study. Further parts of the cortex that were considered unaffected by genotype differences were defined as control region to correct for concentration fluctuations in the staining medium resulting in uneven staining and for uneven illumination between different images. CO activity staining was quantified by measuring the image intensities (I_{ROI}) in the defined ROIs using ImageJ. It should be noted that higher CO activity results in more intense CO-staining, and therefore lower intensity values. All values were referenced against intensity in a cortical control ROI (I_{CON}) in the same slice resulting in $I=I_{ROI}/I_{CON}$. Finally, the resulting value of I was inverted for statistical analysis and graphical display.

2.2.3.5 Statistical analysis

Results from endocrine secretion were analyzed using repeated measurements ANOVA using Statistica 5.0.

Statistical parametric maps were generated using a voxel-wise FDR correction with a threshold of $p_{FDR} < 0.01$. As the found differences were mostly driven by HAB greater than LAB effects, T-maps were created also using FDR correction at the same threshold with a HAB greater than LAB contrast. Significant clusters were identified using the anatomical mouse brain atlas of Franklin and Paxinos [161]. For post-hoc comparisons peak-voxel values of the different regions were extracted and SPSS 17 was used to calculate mean values and corresponding SEM using the same model as in SPM.

Statistical analysis for histological results was done by a multiple comparison analysis. Significance level was set at $p<0.05$. For post-hoc comparison LSD tests were performed when necessary.

2.2.3.6 Correlation analysis

Correlation analysis was performed using the Spearman's rank correlation test. Correlations were calculated between %TOA and the gray level values from CO staining and %TOA and MEMRI signal intensities extracted from the peak voxels of each region showing significant group effect corrected for wb intensity. If effects were found bilaterally in MEMRI measurements, correlations were calculated on mean values of right and left side. Significance was accepted if $p<0.05$.

Chapter 3

Results

3.1 Study I: Fractionated MEMRI

In this study the influence of different Mn^{2+} application protocols on animal well-being and MRI contrast enhancement was investigated.

3.1.1 Endocrine measurements

Figure 3.1 shows the stress response as measured by corticosterone levels to injection of vehicle or Mn^{2+} at the different time points. On the first day (time point d1/4h and d1/12h) corticosterone measurements for the $6 \times 30/48$ and the $8 \times 30/24$ group were pooled (pooled 30), as both groups received their first injection of 30 mg/kg of $MnCl_2 \cdot 4H_2O$. All groups showed the highest corticosterone levels on d1/4h, with levels of 64 ± 49 (mean $\pm$ standard deviation) ng/ml for the control, 160 ± 59 ng/ml for the pooled 30 and 192 ± 187 ng/ml for the $3 \times 60/48$ group. On d1/12h these levels declined to 27 ± 19, 80 ± 63 and 122 ± 84 ng/ml for control, pooled 30 and $3 \times 60/48$ group, respectively. All Mn^{2+} treated groups showed increased corticosterone levels on d1/4h and d1/12h compared to the control group, but not on d5/12h. Statistical analysis failed to reveal a significant effect of group ($F_{2,19} = 2.37, p = 0.12$) at the

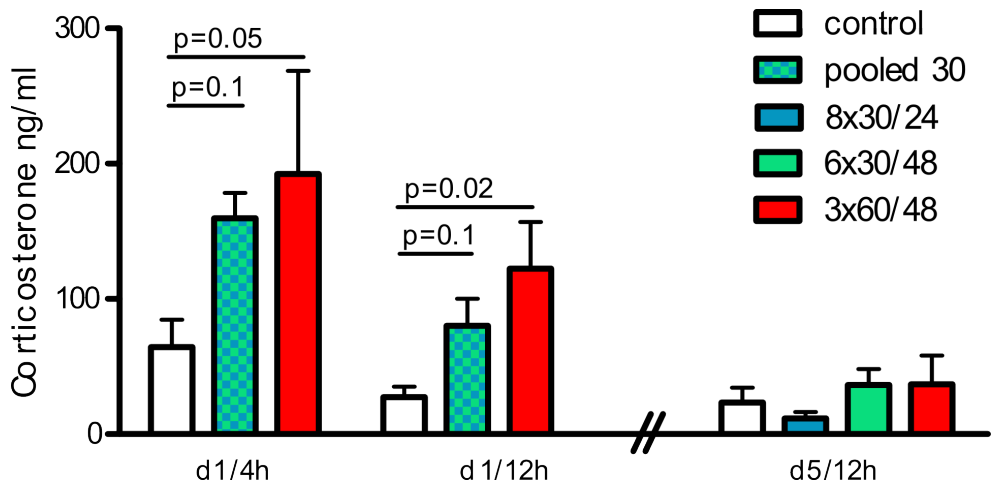

Figure 3.1: Effects of Mn^{2+} treatment on corticosterone secretion. Corticosterone levels at different time points for the different application schemes. $8 \times 30/24$ and $6 \times 30/48$ were pooled at d1 as both groups received first injection of 30 mg/kg $MnCl_2 \cdot 4H_2O$. Mn^{2+} groups started out with higher corticosterone levels than the control group but reached levels of vehicle treated animals after repeated injections.

first time point (d1/4h). Post-hoc tests showed a trend between control and pooled 30 and control and $3 \times 60/48$ ($p = 0.1$ and $p = 0.05$, respectively). At the second time point (d1/12h) a significant effect of group could be detected ($F_{2,19} = 3.51, p = 0.05$) with post-hoc tests showing a trend between control and pooled 30 group ($p = 0.1$) and significant differences between control and $3 \times 60/48$ ($p = 0.02$). At day 5 (d5/12h) statistical analysis failed to reveal significant differences ($F_{3,18} = 2.37, p > 0.5$).

In summary, these results indicate that the first injection with $MnCl_2 \cdot 4H_2O$ causes a considerable amount of stress, but the animals rapidly tend to habituate to it upon repeated $MnCl_2 \cdot 4H_2O$ injection.

3.1.2 Body temperature and locomotion

A significant group effect between the grand means of temperature ($F_{2,12} = 57.25, p < 0.0001$) was found. The LSD post-hoc comparison revealed significant differences between $3 \times 60/48$ and $6 \times 30/48$ ($p < 0.0001$) as well as

$3 \times 60/48$ and $8 \times 30/24$ ($p < 0.0001$). No significant differences between $6 \times 30/48$ and $8 \times 30/24$ (figure 3.2 A) were found. As expected the temperature deviation after NaCl injection was not different from baseline. However, all tested injection protocols differed significantly from the temperature response of the NaCl injection ($p < 0.002$). Body temperature returned to normal after a period of 7.5 hours after the injection of the solution (figure 3.3 B). Time did not have an influence upon repeated injections in neither the $6 \times 30/48$ nor the $8 \times 30/24$ group ($F_{5,10} = 0.80$, p= 0.58, and $F_{7,28} = 1.12$, p= 0.38, respectively), after investigation of the temperature deviation from baseline over the time course of each application protocol. By contrast, the animals receiving the $3 \times 60/48$ protocol showed sensitization to hypothermia induced by Mn^{2+}.

The effects on locomotion were comparable to those detected for body temperature. The grand means of locomotion also showed significant differences between groups ($F_{3,29} = 6.09$, p=0.003). Post-hoc tests revealed a significant difference between $3 \times 60/48$ and $6 \times 30/48$ (p=0.023) as well as between $3 \times 60/48$ and $8 \times 30/24$ (p=0.01). Moreover the $3 \times 60/48$ showed significant difference to the NaCl injection applied three days before the first application of Mn^{2+} ($p < 0.0001$) (figure 3.2). The repeated measurements ANOVA for locomotion deviation from baseline failed to reveal significant differences between different time points in any of the application schemes.

3.1.3 Health assessment

General health status was assessed after every injection and blood collection but any changes between different application schemes were not found (see table 3.1). However, statistical analysis of body weight showed group and time effects ($F_{3,18} = 5.73$, p=0.006 and $F_{2,36} = 10.52$, p=0.005, respectively). Furthermore, the group $\times$ time interaction showed significant

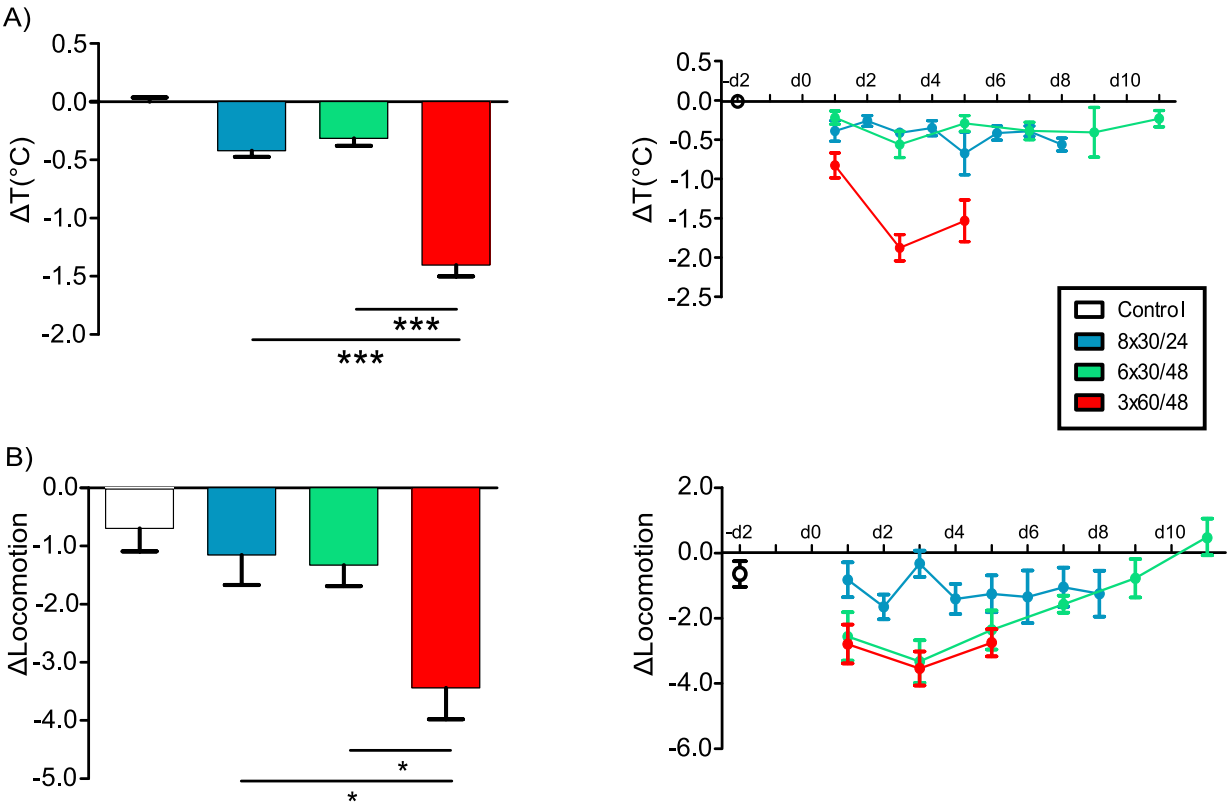

Figure 3.2: Effects of Mn^{2+} treatment on body temperature and locomotion. A) Body temperature: Grand mean over all days of injection (left) and mean of the time course of temperature deviation (right) of the adjacent 7.5 hours after the injection from the corresponding 0.5 h interval of the three day baseline mean. B) Locomotion: Grand mean over all days of injection (left) and time course mean (right) of locomotion deviation of the adjacent 7.5 h after injection from the corresponding 0.5 h intervals of the three day baseline. Locomotion counts are strictly dependent on the distance the animals move with a velocity of above 1 cm/s.

differences ($F_{6,36} = 3.77$, p=0.005), indicating different development of body weight over time. Before the first injection the body weights of animals of the different groups did not differ significantly (average weight: 24.0 ± 0.6 g). All groups receiving Mn^{2+} showed initial weight loss, but only for $8 \times 30/24$ and $3 \times 60/48$ those losses were significant. For all the groups body weights recovered after two days (figure 3.4).

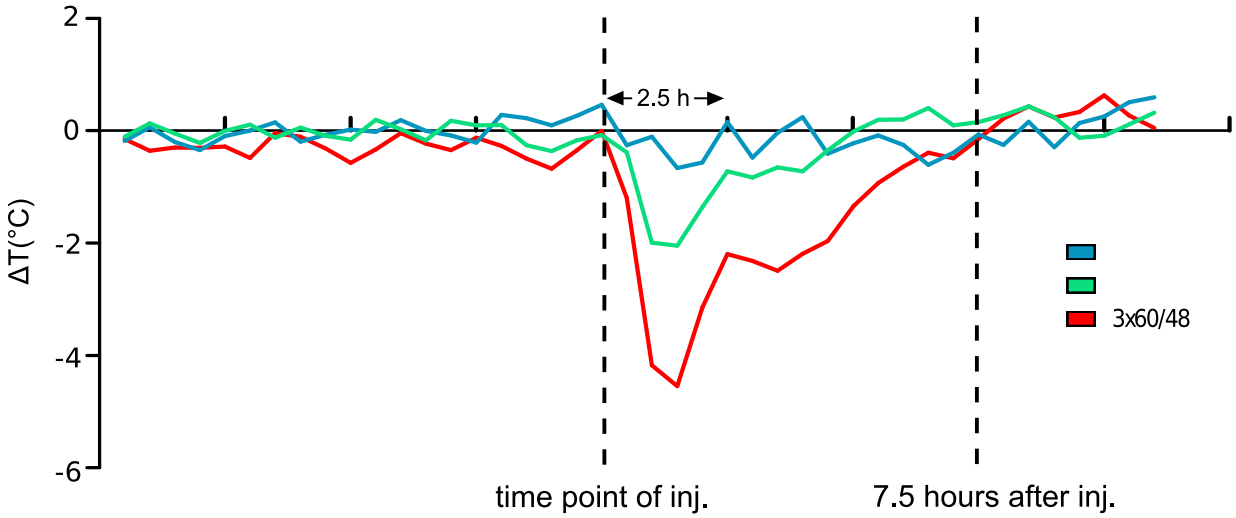

Figure 3.3: Course of body temperature for the different fractionated injection protocols. Temperature drop shown as mean curve of 0.5 h intervals after the second injection (d2 for $8 \times 30/24$, d3 for $3 \times 60/48$ and $6 \times 30/48$). The $3 \times 60/48$ application shows a mean temperature drop of around 5°C whereas the $8 \times 30/24$ and the $6 \times 30/48$ show temperature drops of maximal 1.5°C and 2°C respectively.

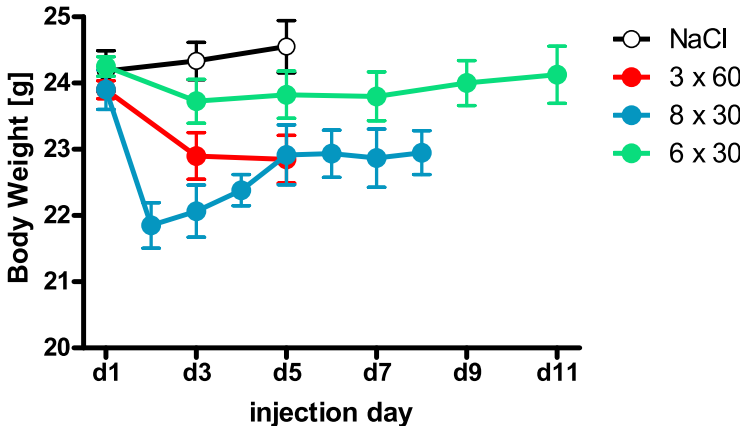

Figure 3.4: Body weight. Development of body weight over time during the course of the different injection protocols. After initial weight loss in Mn^{2+} treated groups body weights were recovering.

	Control	$3 \times 60/48$	$8 \times 30/24$	$6 \times 30/48$
Number of animals	6	6	6	4
Observation period in days	5	5	8	11
Deaths	0	0	0	0
Body position	normal	normal	normal	normal
Tremor	normal	normal	normal	normal
Palpebral closure	normal	normal	normal	normal
Coat appearance	normal	normal	normal	normal
Whiskers	normal	normal	normal	normal
Lacrimation	normal	normal	normal	normal
Defecation	normal	normal	normal	normal
Gait	normal	normal	normal	normal
Tail elevation	normal	normal	normal	normal

Table 3.1: No detectable changes in health conditions were observed in any group of animals.

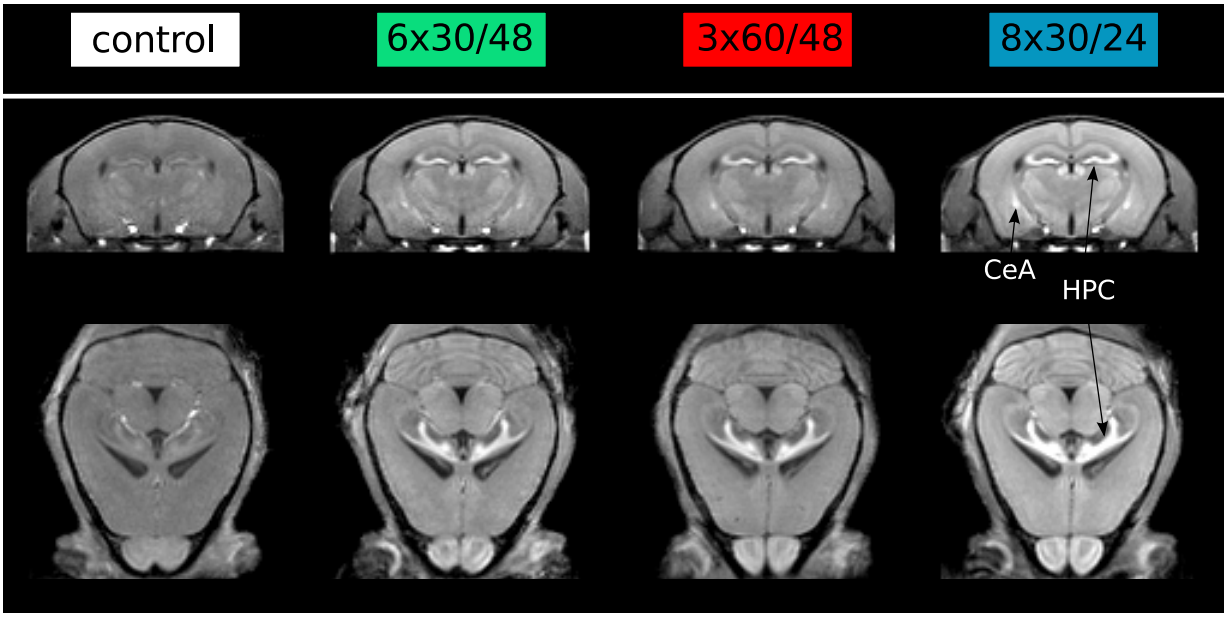

Figure 3.5: Contrast enhancement for different injection protocols. Coronal (top) and horizontal (bottom) slices for control, $6 \times 30/48$, $3 \times 60/48$ and $8 \times 30/24$ application schemes. Intensity corrected mean images of the different groups are shown. All Mn^{2+} images show higher intensities than images of NaCl injected animals. The $8 \times 30/24$ group shows highest intensity and best contrast enhancement. The $3 \times 60/48$ and $6 \times 30/48$ group visually exhibit similar signal intensity and contrast enhancement. Signal enhancement in the HPC and the CeA are highest in the $8 \times 30/24$ group.

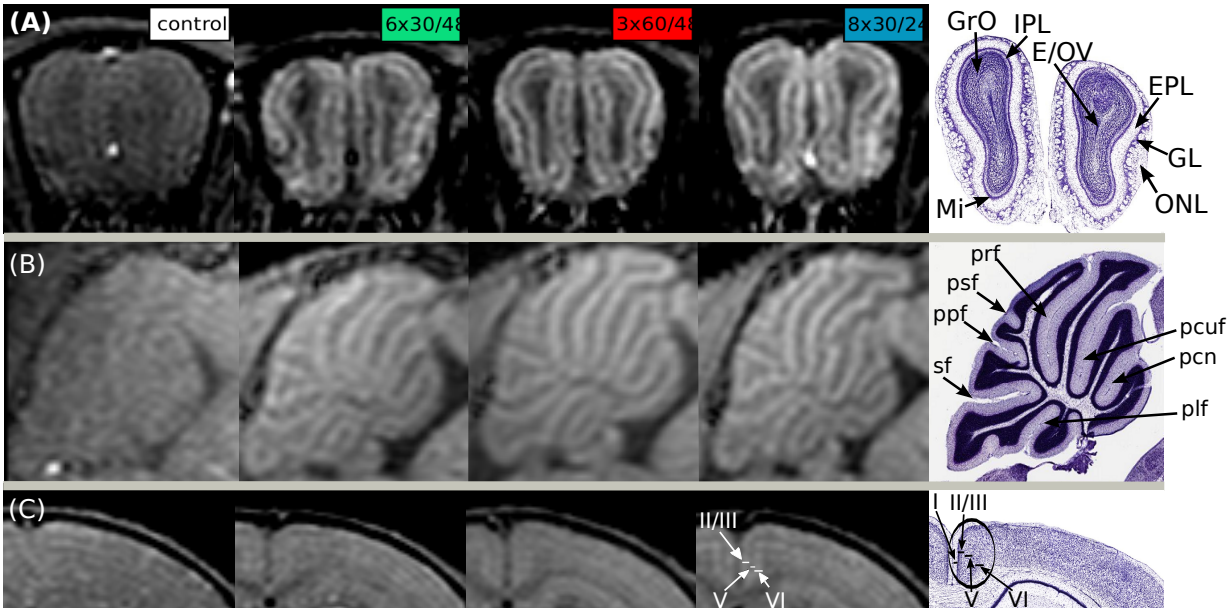

Figure 3.6: Visualization of fine structures. Shown slices are representative images of individual mice. A) Coronal sections of the OB. Its different layers can be distinguished well in every protocol involving Mn^{2+}. On the Nissl stain on the right the different layers of the bulb are indicated (http://mouse.brainmap.org/atlas/ARA/Coronal) (E/OV: ependymal and subependymal layer/olfactory ventricle. EPL: external plexiform layer, GL: glomerular layer, GrO: granular layer, IPL: internal plexiform layer, Mi: mitral cell layer, ONL: Olfactory bulb layer). B) Sagittal sections of the CrB. Delineation of the laminar structures is not present in the control group, while Mn^{2+} application led to improved tissue contrast in ascending order from $6 \times 30/48$ to $3 \times 60/48$ to $8 \times 30/24$. The Nissl stain on the right is inserted on approximately the same location to indicate different structures (www.brainmaps.org) (plf: posterolateral fissure, pcn: precentral fissure, pcuf: preculminate fissure, prf: primary fissure, psf: posterior superior fissure, ppf: prepyramidal fissure, sf: secondary fissure). C) Coronal sections of the cortex. The location of the RSG is indicated by the ellipse in the Nissl stain (right, http://mouse.brain_map.org/atlas/ARA/Coronal). Layers were identified according to the Allen mouse brain atlas (http://mouse.brain_map.org), with cortical layer IV not being present in the RSG. Layers indicated on the Nissl stain are best discriminated on the $8 \times 30/24$ MR image.

3.1.4 MRI signal intensities

Figure 3.5 shows representative coronal and horizontal slices of T1w mean images for each group. Upon visual inspection all Mn^{2+} show higher contrast than the control group. Of the investigated groups the $8 \times 30/24$ group exhibits the highest overall signal and best contrast enhancement. This becomes especially clear in the HPC, the olfactory bulb (OB) and the cerebellum (CrB).

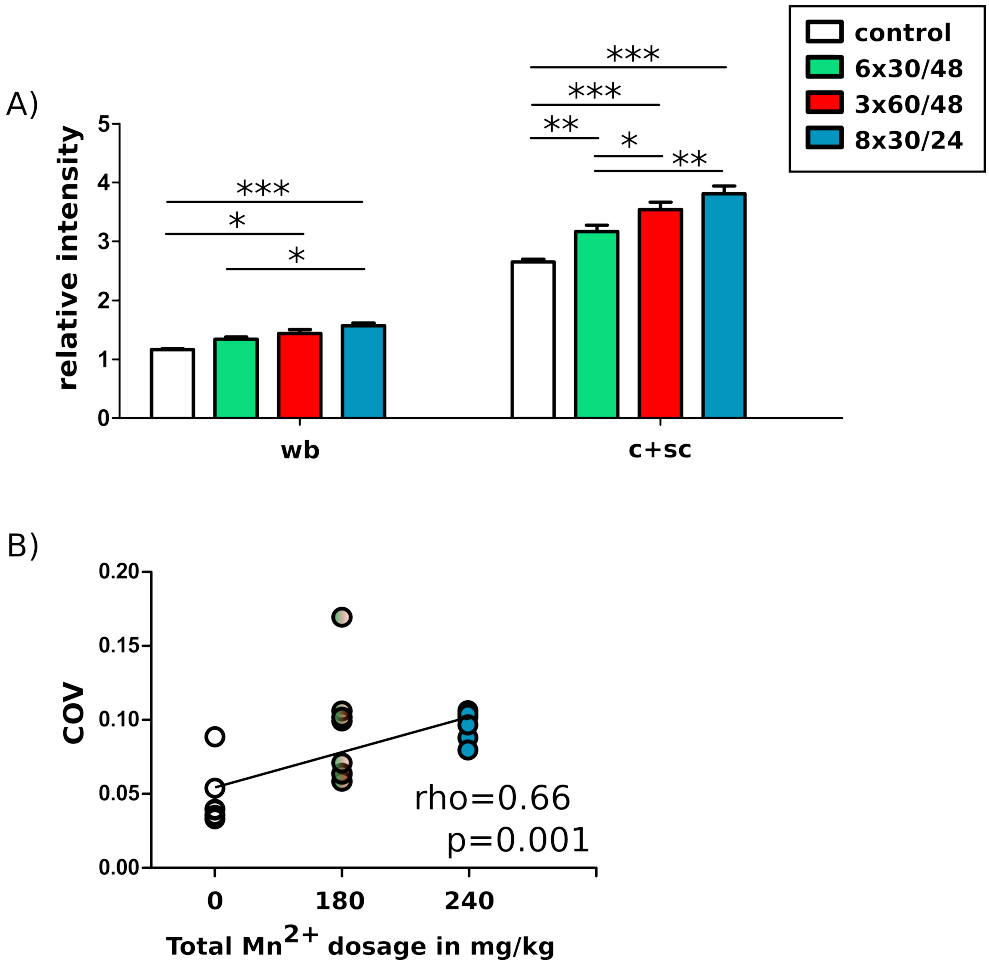

Figure 3.7: MRI signal intensities and contrast enhancement A) MRI signal enhancement in the whole brain (wb) and the average relative intensities (RI) over all cortical and subcortical (c+sc) ROIs. An increase in signal intensities was detectable from control (NaCl) to $8 \times 30/24$ in both wb as well as c+sc (* $p<0.05$, ** $p<0.01$, *** $p<0.001$). B) COV across all regional RIs calculated for each animal. A Spearman rank test was applied to the COV for the total Mn^{2+} dose delivered to the animals. The correlation coefficient was found to be $\rho = 0.66$, with a p-value of p=0.001, indicating that a higher total amount of Mn^{2+} applied provides better contrast.

The $8 \times 30/24$ protocol is followed by the $3 \times 60/48$ and the $6 \times 30/48$ group in the respective order. Reprocessed representative images show that layers of the OB were distinguishable in every injection protocol involving Mn^{2+}. However, the $8 \times 30/24$ protocol showed best contrast enhancement (figure 3.6 A). Furthermore the distinction between the layers of the CrB is present in all images acquired with Mn^{2+} (figure 3.6 B). While for distinguishing layers of the OB and layers of the CrB all three protocols seemed to be equally suitable the visualization of cortical layers of the RSG was superior using the $8 \times 30/24$ followed by the $3 \times 60/48$. Using the $6 \times 30/48$ protocol the layers were hard to distinguish (figure 3.6 C). A significant effect of the application scheme for both the wb RI as well as c+sc RI was detected ($p=0.002$ and $p<0.0001$, respectively). Post hoc tests revealed a stepwise increased order (control$\rightarrow 6 \times 30/24 \rightarrow 3 \times 60/48 \rightarrow 8 \times 30/24$). Within each group the wb RI showed lower values than c+sc RI (p-values < 0.038) (figure 3.7 A). Upon separate modeling of the ROIs strong effects of both group ($F_{3,126} = 106.3$, $p < 0.0001$) and region ($F_{6,126} = 8.5$, $p < 0.0001$) were detected. However, the group$\times$region interaction was not significant ($F_{18,126} = 1.4$, $p = 0.154$), indicating that sorting of the regional RIs was similar for all application groups. Conducting pair wise post hoc tests revealed significance of 12 pairs for the $8 \times 30/24$ protocol, as compared to 7, 5 and 3 pairs for control, $6 \times 30/48$ and $3 \times 60/48$, respectively. Furthermore, a moderate correlation was detected between the coefficient of variation (calculated across the seven ROIs for each animal) and the total delivered dose of Mn^{2+} (Spearman rank test, $\rho=0.66$, $p=0.001$) (figure 3.7 B).

3.2 Study II: Dynamical behavior of manganese in the $8 \times 30/24$ injection protocol

In this study the temporal dynamical behavior of the $8 \times 30/24$ injection protocol was investigated.

3.2.1 Accumulation of Mn^{2+}

As expected, the fractionated application protocol lead to a successive increase in cerebral tissue MEMRI contrast (figure 3.8 A). Globally, strongest signal enhancement is observed after the termination of the complete protocol. More specifically, some ROIs showed faster accumulation as others as determined by the slope of T1w image intensity.

3.2.1.1 Voxel wise linear fitting

A linear model was fitted to the data on a voxel-by-voxel basis. Figure 3.9 A and B show maps of the slope and the coefficient of determination r^2, respectively. The map of the slope resembles an anatomical image of a mouse brain as acquired with MEMRI, indicating a steep increase (high slope values) of RI in regions showing high RIs on T1w images and a flat increase (low slope values) in regions displaying dark RIs (figure 3.9 A). The map of coefficient of determination r^2 shows a more uniform distribution, however, showing slightly higher r^2 values in regions with steep slope (figure 3.9 B). An example of linear regression is shown for one voxel of the GP in figure 3.9 D.

To get a quantitative impression of the slope ROI analysis on the slope- and r^2 map was performed. The values for slope and coefficient of determination as extracted from different regions (figure 2.10) of the slope- and r^2-map are given in table 3.2. The highest increase of RI was found in the CeA (figure 3.9 A e), GP (figure 3.9 A d), BNST vGP (figure 3.9 A c) and IC (figure 3.9

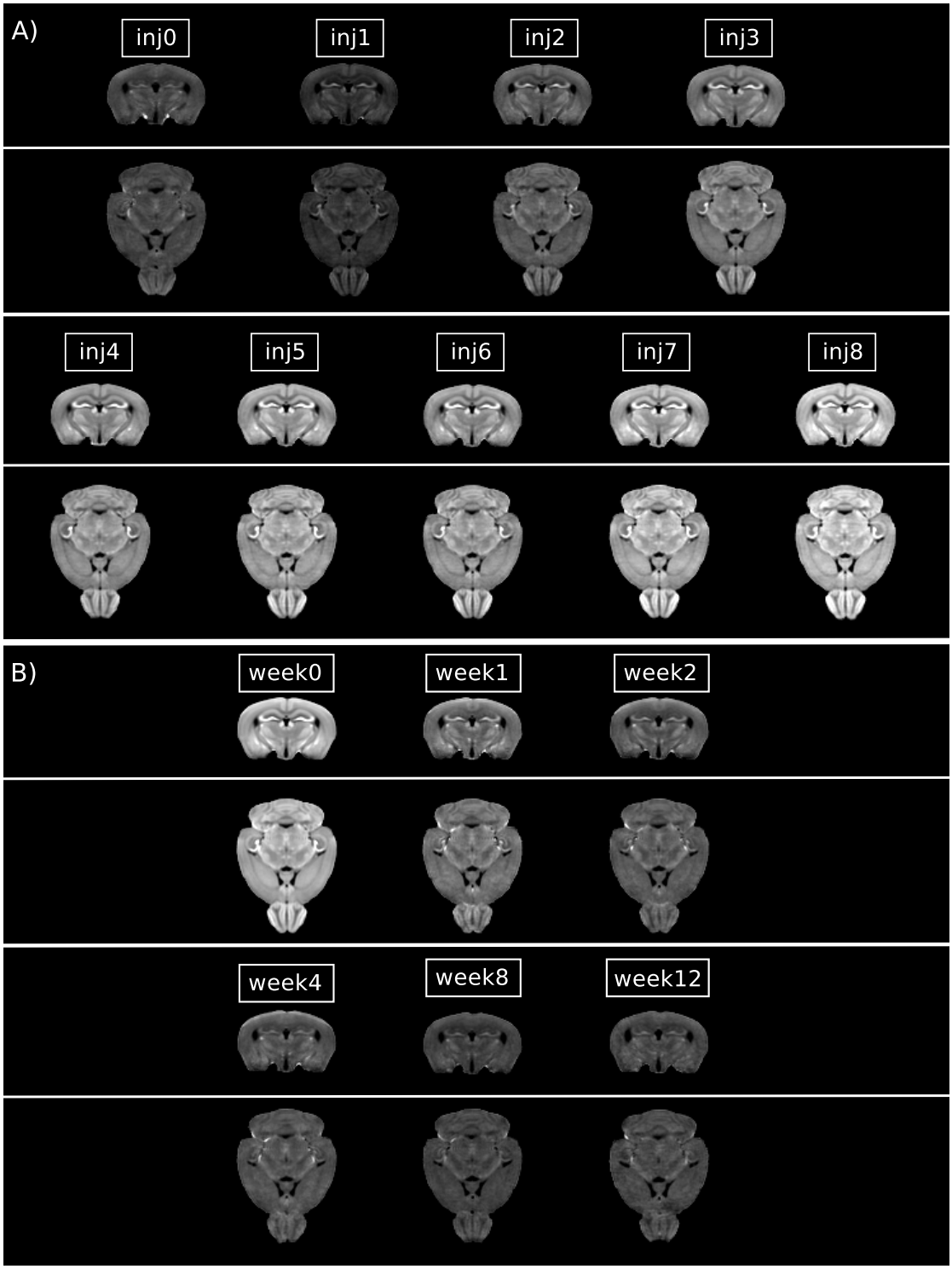

Figure 3.8: Mean images of different groups. Mean images were calculated with intensity corrected spatially normalized images. A) Accumulation. Visual inspection indicates an increase of RI from control to injection 8. Also contrast enhancement increases with increasing number of injection. Different time points during the fractionated application scheme are indicated above the corresponding image. Mean image of control animals is also shown (inj0). B) Clearance. Visual inspection shows decreasing RI and contrast enhancement with time. Different time points after last injection are indicated above corresponding images.

A i), followed by the CA3 region of the HPC (figure 3.9 A f), the superior colliculi (SC) (figure 3.9 A h) and the CA1/2 region of the HPC (figure 3.9 A f). Regions with lowest accumulation included the dentate gyrus (DG), entorhinal and piriform cortex (EC and PC, respectively) as well as the HTh. All other regions showed intermediate increase of RI. Values for r^2 were highest for GP and CeA, i.e. the regions with steepest increase in RI. Generally, r^2 values were higher in ROIs with steeper slope. The r^2 values ranged between 0.60 (OB) and 0.80 (GP, CeA), indicating that for example for the CeA 80% ($r^2 \cdot 100\%$) of scattering are explained by the number of injection and that the use of a linear model is reasonable. Further, all regressions were significant with $p < 0.0001$.

3.2.1.2 ROI analysis

Two way ANOVA revealed strong effects of both number of injection ($F_{8,1575} = 961$, $p < 0.0001$) and RI of the 21 ROIs ($F_{20,1575} = 85.7$, $p < 0.0001$). The interaction effect number of injection $\times$ RI of ROIs was also highly significant ($F_{160,1575} = 2.3$, $p < 0.0001$), indicating that the enhancement in some ROIs was more pronounced with increasing number of injection than in other ROIs.

Six ROIs were chosen for closer analysis of the accumulation process. To cover the whole range from shallow to steep increase in RI as determined in section 3.2.1.1 the CeA and the GP representing regions with steep increase, the CA1/CA2 region of the HPC and the SC representing regions with intermediate increase in RI, and the DG and the CPU, representing regions with little increase in RI, were chosen for analysis.

As an effect of number of injection was present, independent sample T-tests were conducted as post-hoc tests. Furthermore, to correct for the number of performed tests the nominal α-level $p_{nom} = 0.05$ was divided by the number

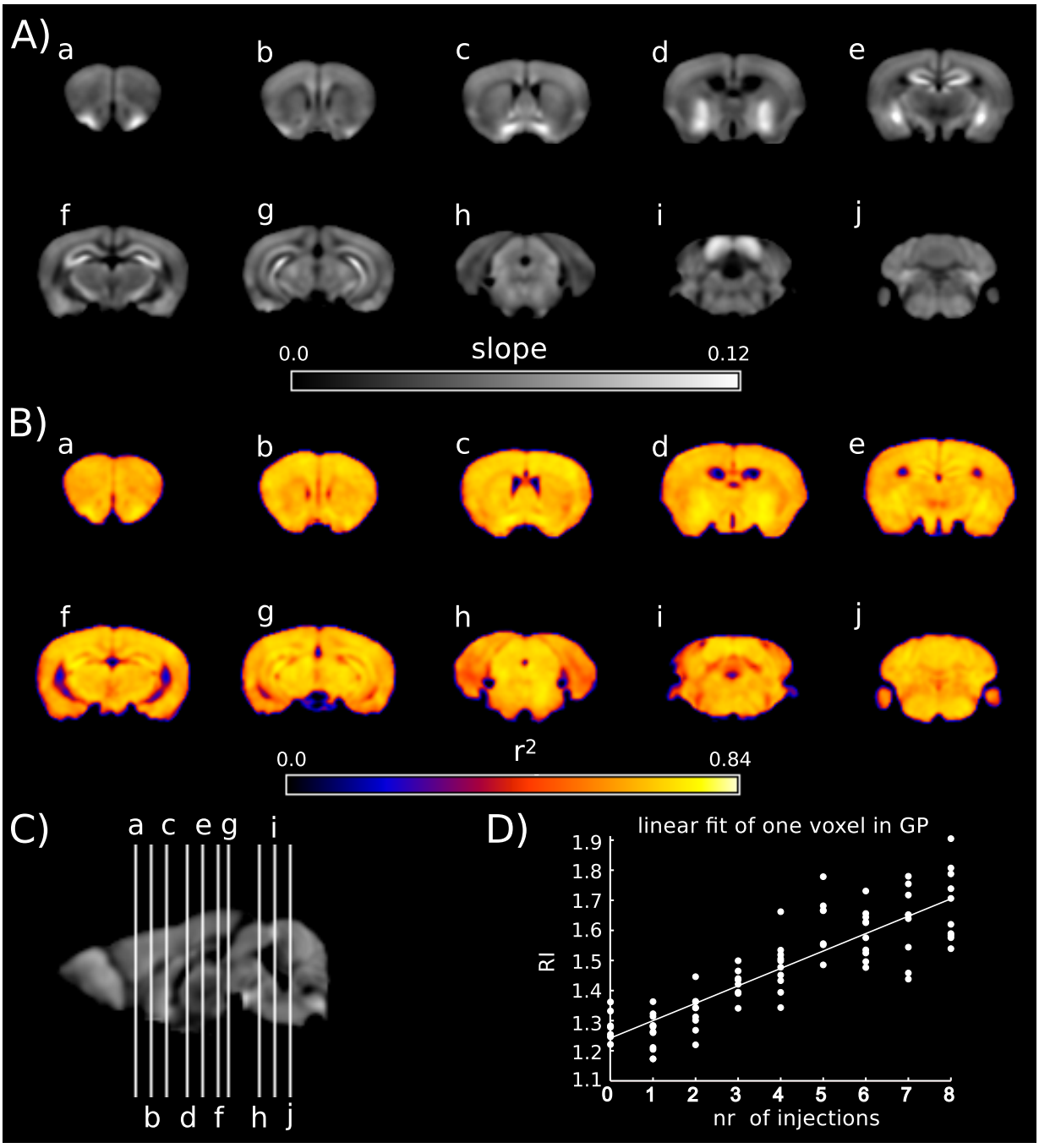

Figure 3.9: Mn^{2+} accumulation. Figure shows slope A) and goodness of fit r^2 B) gained from a voxel-by-voxel linear regression on smoothed images. High slope values indicate a steep increase of RI in T1w-images, representing increased accumulation of Mn^{2+} in these regions. C) indicates slices shown in A) and B) on a sagittal view. D) shows the distribution of RI values for one voxel in the GP. The line indicates the best fit.

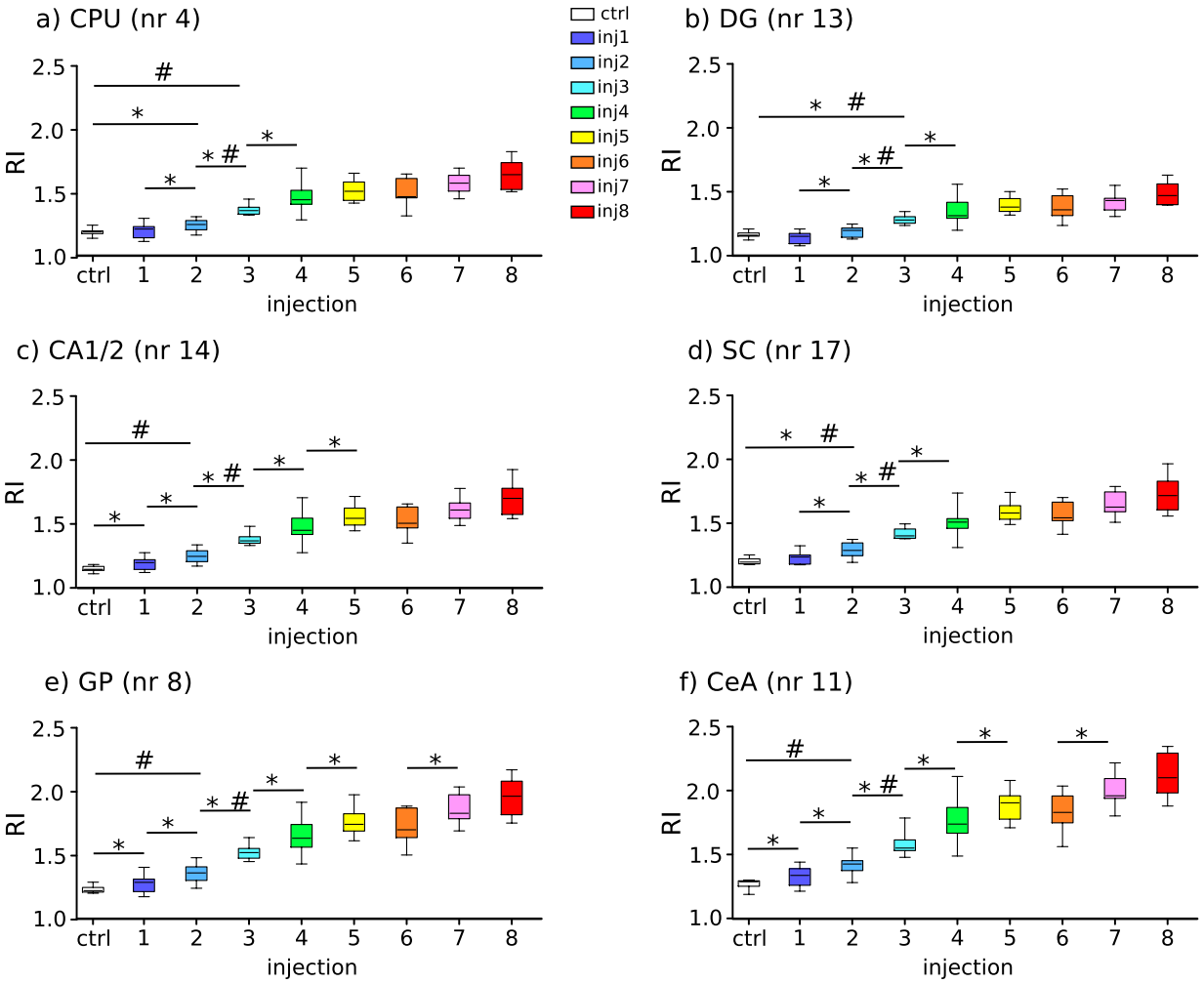

Figure 3.10: ROI analysis for Mn^{2+} accumulation. CPU (a), DG (b), CA1/2 (c), SC (d), GP (e), and CeA (f) were chosen for more detailed analysis. Numbering of ROIs according to figure 2.10 are indicated besides name of ROI. Independent sample T-tests were applied to test whether an additional injection could significantly enhance RI in comparison to the preceding injection. Furthermore, it was tested, how many injections were necessary to reach significantly different RI from control level. *:p<0.05 (nominal α-level), #:p<0.001 (corrected α-level). P-values are given in tables 3.3 and 3.4.

ROI	nr of ROI	slope [1/d]	r^2
OB	1	0.057	0.60
cortex	2	0.056	0.71
PC	3	0.053	0.64
CPU	4	0.057	0.71
Nacc	5	0.057	0.61
septum	6	0.058	0.69
BNST vGP	7	0.075	0.75
GP	8	0.083	0.80
HTh	9	0.053	0.64
Th	10	0.056	0.74
CeA	11	0.094	0.80
CA1/2	12	0.062	0.72
DG	13	0.052	0.66
CA3	14	0.068	0.69
EC	15	0.050	0.60
MB	16	0.060	0.73
SC	17	0.064	0.77
IC	18	0.073	0.76
PAG	19	0.058	0.77
CrB	20	0.057	0.70
BS	21	0.057	0.69

Table 3.2: The first two columns indicate the name of the ROIs and their number as defined in figure 2.10. Columns three and four show slopes and corresponding goodness of fit r^2 for the linear fit of Mn^{2+} accumulation. Values were assessed by ROI analysis of slope-, corresponding r^2-map for the accumulation process. All slopes were significantly different from 0 ($p<0.0001$).

of tests resulting in a corrected α-level of $p_{cor} = 0.001$. To ensure that no effect was missed, results are given for both p_{nom} and p_{cor}.

Independent sample T-tests revealed that at p_{nom} the first injection could already produce significantly higher RIs than control level in the GP, the CeA and CA1/2, while in the CPU and the SC two injections were needed. The DG showed significantly different RIs only after three injections. However, using p_{cor} two injections needed to be applied to produce significantly higher RIs than control level in regions with steep and intermediate slope (CeA, GP, CA1/2, SC) and three injections for regions with shallow slope (CPU, DG).

P-values are listed in table 3.3. To further investigate, if additional injections

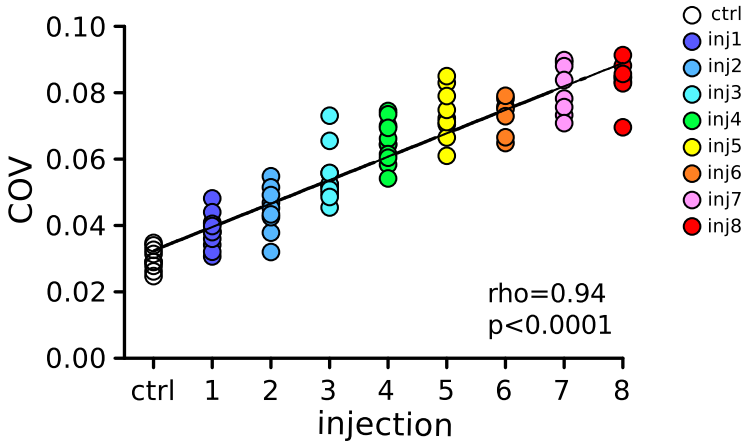

Figure 3.11: Correlation COV with number of injections. COVs calculated across all regional RIs calculated for all animals. A Spearman rank test was applied to the COV for the number of injection. The Spearman rank correlation coefficient was found to be ρ=0.94, with p<0.0001, indicating that increasing number of injections produced increased contrast enhancement.

could produce a significant increase in RI compared to the preceding injection, independent sample T-tests were conducted. Injection 2, 3 and 4 could produce significantly higher RIs than their preceding injection in all ROIs for nominal α-level. Additionally, injection 5 provided significantly higher RIs than injection 4 in the CA1/2 region of the HPC, GP and CeA for p_{nom}. Furthermore, the GP and CeA exhibited significantly higher RI after injection 7 as compared to injection 6, also for p_{nom}. Yet, at corrected α-level only injection 3 was able to produce significantly higher RI than its preceding injection. Figure 3.10 shows the distribution of data for all six ROIs. Significant differences are indicated. P-values for comparisons are given in table 3.4. It further should be noted that T1w-image intensities enhanced through Mn^{2+} show huge standard deviation differences between those animals with a higher number of injections compared to control animals or animals receiving only one or two injections of $MnCl_2 \cdot 4H_2O$. Closer inspection of the individual data sets revealed that lower intensities were consistenly found in specific

ROI	nr. of inj (p_{nom})	p-value	nr. of inj (p_{cor})	p-value
CPU	2	0.004	3	<0.0001
DG	3	<0.0001	3	<0.0001
CA1/2	1	0.007*	2	<0.0001*
SC	2	0.0005	2	0.0005*
GP	1	0.021*	2	0.001*
CeA	1	0.015*	2	<0.0001

Table 3.3: P-values of pair-wise t-tests for number of injection, which produces significantly higher RI in comparison to control level. * indicates when variances were unequal.

ROI	1 vs 2	2 vs 3	3 vs 4	4 vs 5	5 vs 6	6 vs 7	7 vs 8
CPU	0.03	<0.0001	0.009*	0.14	0.43	0.1	0.1
DG	0.02	<0.0001	0.03*	0.12	0.37	0.2	0.07
CA1/2	0.008	<0.0001	0.013*	0.05	0.32	0.08	0.07
SC	0.008	<0.0001	0.009	0.07	0.38	0.09	0.1
GP	0.007	<0.0001	0.006*	0.04	0.33	0.04	0.09
CeA	0.008	<0.0001	0.002	0.05	0.25	0.02	0.07

Table 3.4: P-values of independent samples T-test for comparisons of consecutive injections. * indicates when variances were unequal.

animals, indicating inter-individual differences in metabolization of Mn^{2+} and its transport and delivery to the brain.

Furthermore, a strong correlation between the COV and the number of injection was detected (Spearman rank test, ρ=0.94, p<0.0001), indicating a strong contrast enhancement with increasing number of injection (figure 3.11).

3.2.2 Clearance of Mn^{2+}

After termination of the fractionated application protocol clearance will finally set in. MEMRI contrast decreases with time in an exponential manner. Visual inspection indicates, that signal intensities are back to level of control condition four weeks after the last injection (figure 3.8 B). Thus, the clearance process takes much longer as the accumulation indicating a passive transport

ROI	nr of ROI	$\tau_{1/2}$[d] best fit	$\tau_{1/2}$[d] up	$\tau_{1/2}$[d] low	CI width [d]	r^2
OB	1	6.52	5.47	10.27	4.80	0.63
cortex	2	-	-	-	-	-
PC	3	6.53	5.33	12.52	7.19	0.69
CPU	4	5.83	3.88	12.01	8.13	0.74
Nacc	5	5.41	3.56	11.43	7.87	0.76
septum	6	5.79	3.94	11.96	8.02	0.73
BNST vGP	7	6.54	4.20	16.10	11.90	0.78
GP	8	5.67	3.55	14.29	10.74	0.81
HTh	9	6.08	4.20	12.61	8.41	0.72
Th	10	6.02	3.96	12.80	8.84	0.75
CeA	11	6.73	4.21	16.97	12.76	0.80
CA1/2	12	5.99	4.09	11.99	7.90	0.73
DG	13	6.48	4.54	11.94	7.40	0.69
CA3	14	5.84	4.17	11.91	7.74	0.73
EC	15	6.73	4.95	11.71	6.76	0.66
MB	16	6.29	4.35	13.53	9.18	0.75
SC	17	5.85	3.76	13.40	9.64	0.78
IC	18	6.67	4.26	15.74	11.48	0.77
PAG	19	7.22	4.68	16.00	11.32	0.75
CrB	20	5.99	4.17	12.57	8.40	0.74
BS	21	6.70	4.73	13.79	9.06	0.73

Table 3.5: The first two columns indicate the name of the ROI and the number of the ROI as defined in figure 2.10. Columns three, four and five show half-life estimate from best fit, upper (up) and lower (low) boundary of 95% CI for clearance of Mn^{2+} in days. Column six contains the width of the confidence interval in days. Column seven contains r^2-values of the exponential fit. Due to a fat artifact in the cortex it was left out of analysis.

system for Mn^{2+} clearance.

3.2.2.1 Voxel wise exponential fitting

The half-life map shown in figure 3.12 A shows a quite uniform distribution of half-lives. The bright band in the cortex is due to a fat artifact and thus the cortex will be left out of the analysis for the clearance study. Performing a ROI analysis on the map of half-lives revealed region dependent values with the longest half-lives in the PAG, CeA, and EC, followed by the IC, BNST

vGP, PC, HTh, and Th. The CA3 and CA1/2 region of the HPC showed short half-lives compared to the DG which showed intermediate half-life. To estimate the goodness of fit both, half-lives from the fit belonging to the lower and upper boundary of the 95% CI as well as the coefficient of determination r^2 were determined (values see table 3.5). The width of the 95% CI was found to vary between the different ROIs from 4.8 days in the OB to around 13 days in the CeA. Generally, the 95% CI was found to be wider in ROIs having a higher propensity to take up Mn^{2+}, such as the CeA, GP and IC. The width of the CI is dependent on the standard deviation. Thus, ROIs with higher standard deviation exhibit wider CIs. In figure 3.13 it can be seen, that ROIs showing high accumulation at time point 0 and 1 also show higher standard deviation and thus wider CIs. Values of coefficient of determination r^2 were higher in ROIs with higher Mn^{2+} accumulation, but also quite uniform over the whole brain (figure 3.12 B), as half-lives. The values ranged between 0.63 (OB, Nacc) and 0.81 (GP), indicating that for example for the GP 81% ($r^2 \cdot 100\%$) of scattering are explained by the time point after last injection and that the use of an exponential model is reasonable. An example of exponential regression is shown in figure 3.12 D for a voxel in the GP.

3.2.2.2 ROI analysis

Two-way ANOVA revealed strong effects of both weeks after last injection ($F_{5,1638} = 1033.3$, $p < 0.0001$) and RI of the 21 ROIs ($F_{20,1638} = 12.1$, $p < 0.0001$). The interaction effect weeks after injection $\times$ RI of ROIs was also highly significant ($F_{100,1638} = 2.3$, $p<0.0001$), indicating that the decrease in RI was more pronounced in some ROIs than in others.

ROI analysis was conducted to find the time point at which RI had returned to the level of 12 weeks after the last injection. This analysis was conducted on the same regions as ROI analysis for the accumulation process, namely,

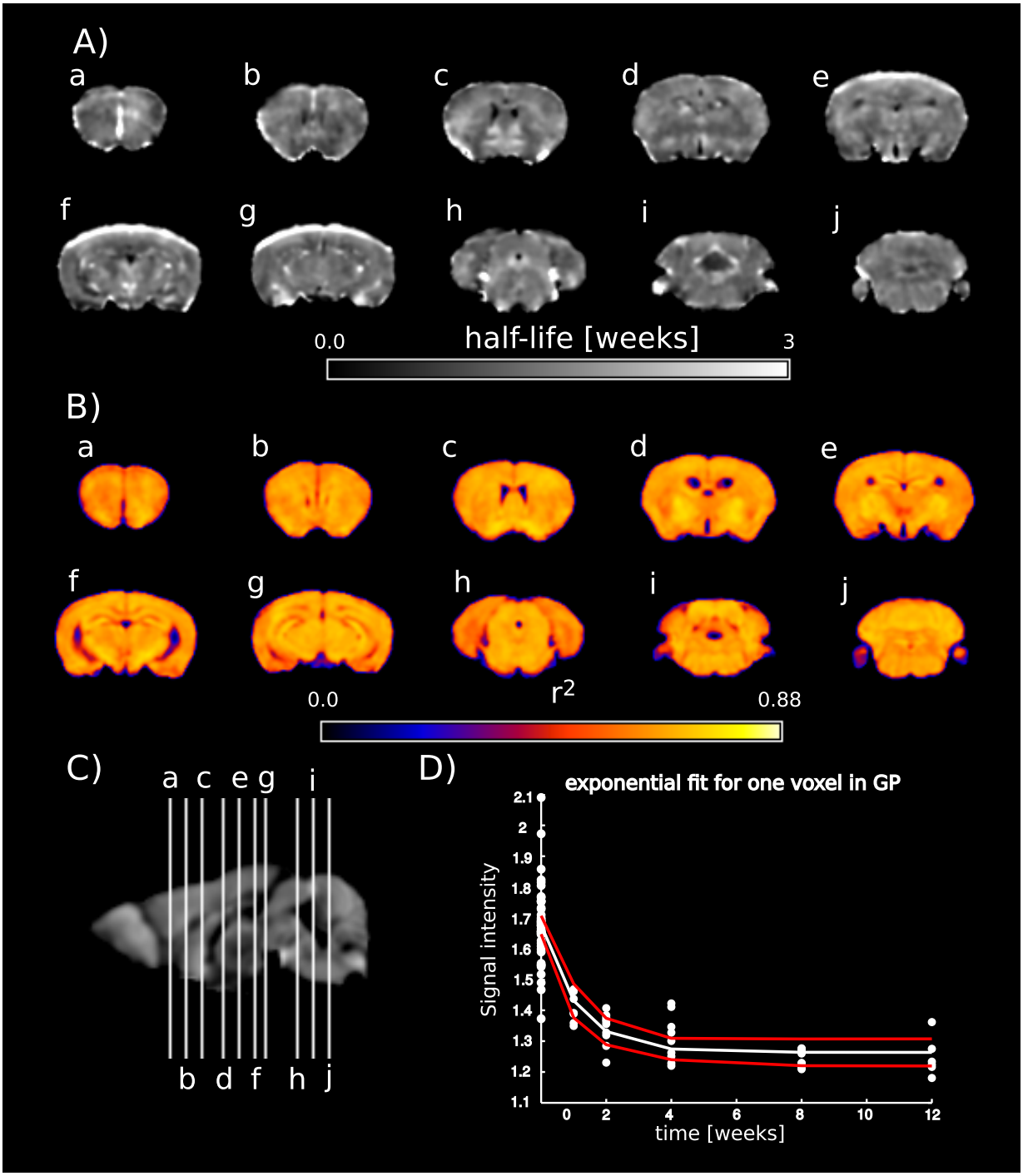

Figure 3.12: Clearance. Half-life determined from best fit values in weeks A) and goodness of fit r^2 B) as assessed by an exponential fit on a voxel-by-voxel basis. Longer half-life values indicate a slower decrease in T1w-images, representing slower clearance of manganese in these brain regions. C) indicates the coronal slices shown in A) and B). D) shows the distribution of RI values in an example voxel of the GP at time points 0, 1, 2, 4, 8 and 12 weeks. The white line indicates the best fit and red lines the 95% confidence interval.

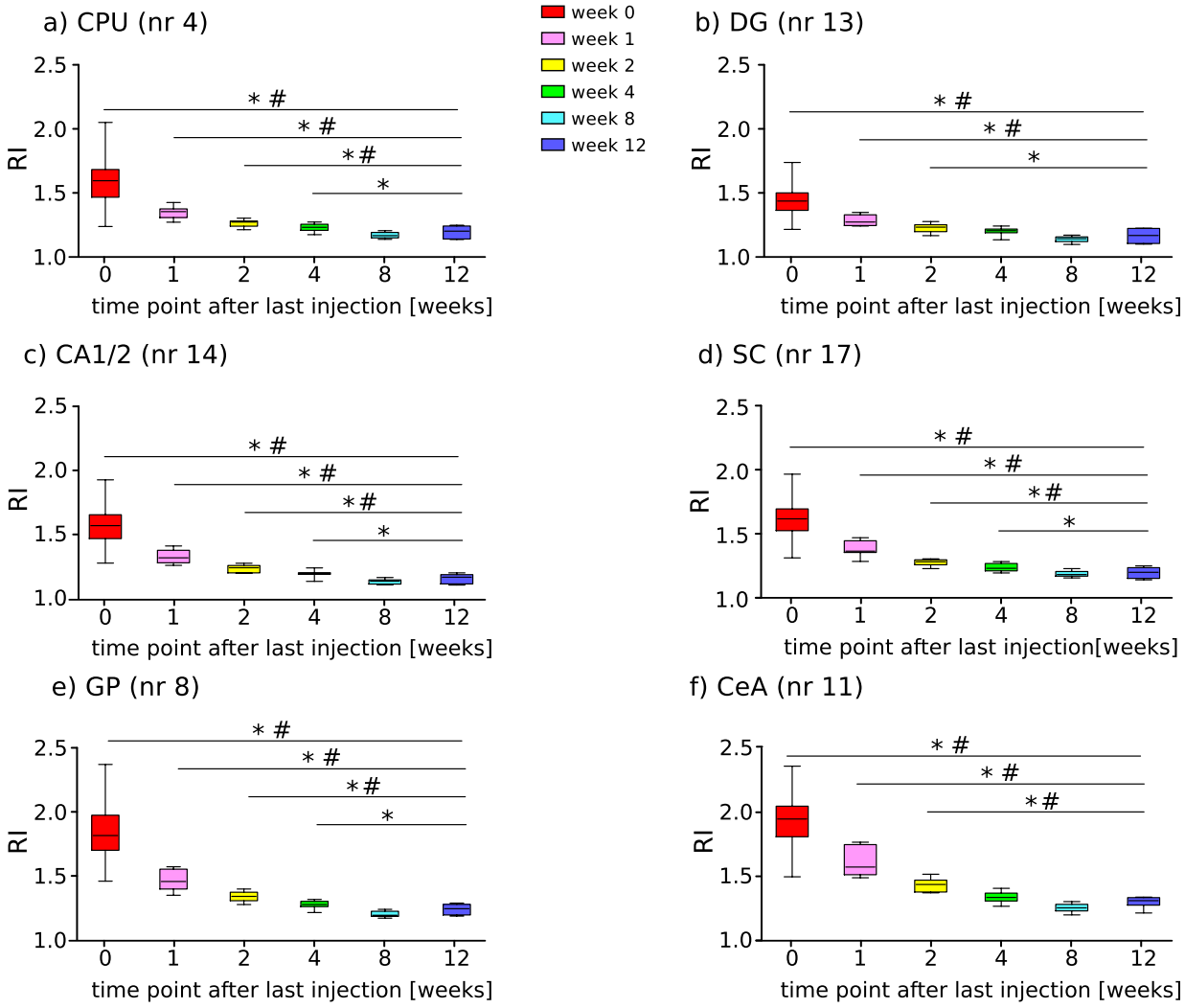

Figure 3.13: ROI analysis for Mn^{2+} clearance. CPU (a), DG (b), CA1/2 (c), SC (d), GP (e), and CeA (f) were chosen for more detailed analysis. Numbering of ROIs according to figure 2.10 are indicated besides name of ROI. Independent sample T-tests were applied to test when RIs were back to level of control condition. *:p<0.05 (nominal α-level),#:p<0.002 (corrected α-level).

the CeA, GP, CA1/2 region of the HPC, SC, DG and the CPU. As two-way ANOVA revealed an effect of time point after last injection independent sample T-tests were applied as post-hoc tests to account for unequal variances present in the data. Figure 3.13 shows comparisons graphically. Time points, 0, 1 and 2 were significantly different from control condition in all ROIs for nominal α-level. For corrected α-level only the DG did not reach significance

for time point 2. Further, time point 4 showed significantly higher RIs for nominal α-level in all ROIs but the CeA, and for corrected α-level in none of the investigated ROIs. Time point 8 did not show significantly increased RI in any of the ROIs for neither nominal nor corrected α-level. All necessary p-values are listed in table 3.6. It is noticeable, that the ROIs representing ROIs with high Mn^{2+} accumulation (CeA, GP) showed huge standard deviation at time point 0 and 1. This might explain the wider 95% CIs found in section 3.2.2.1 in these ROIs.

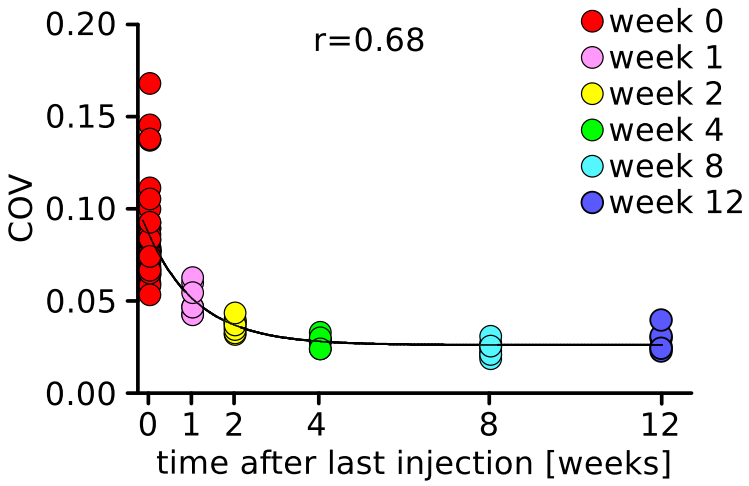

Figure 3.14: Correlation COV with time point after last injection. COVs across all regional RIs calculated for all animals. An exponential correlation was calculated for the COV and the time point of measurement after the last injection [days]. Correlation coefficient was found to be ρ=0.68, indicating that contrast enhancement decreased exponentially with time.

Figure 3.14 shows the COV in correlation with the time point after last injection in weeks. As RIs, the COV showed an exponential decay with time, indicating that contrast enhancement decreased exponentially with time. A moderate exponential correlation was found (r=0.68).

ROI	0 vs 12	1 vs 12	2 vs 12	4 vs 12
CPU (4)	<0.0001	<0.0001	0.0015	0.05
DG (13)	<0.0001	0.0005	0.007	0.06
CA1/2 (14)	<0.0001	<0.0001	<0.0001	0.02
SC (17)	<0.0001	<0.0001	<0.0001	0.02
GP (8)	<0.0001	<0.0001	<0.0001	0.03
CeA (11)	<0.0001	<0.0001	<0.0001	0.07

Table 3.6: P-values of pair-wise t-tests (unequal variances assumed) for number of injection, which produces significantly higher RI in comparison to control level.

3.3 Study III: Application of MEMRI in a mouse model of extremes in trait anxiety

In this study MEMRI was applied to the HAB/NAB/LAB mouse model.

3.3.1 Endocrine measurements

Figure 3.15 shows the stress response of the different mouse lines to the injection of $MnCl_2 \times 4{\cdot}H_2O$ 1 hour after the first, 4 hours after the second and 4 hours after the third injection. All three groups show highest corticosterone levels on the first time point, with mean levels of 237±225 (mean ± standard deviation) ng/ml for HAB, 354±135 ng/ml for NAB and 302±247 ng/ml for LAB animals. On the second time point levels declined to 145±66 ng/ml for HAB, 222±137 ng/ml for NAB and 160±117 ng/ml for LAB animals. For the third time point corticosterone levels remained more or less at the same levels as on time point 2 with mean levels of 160±83 ng/ml for HAB, 278±172 ng/ml for NAB and 188±225 ng/ml for LAB animals. Repeated measurements ANOVA revealed a significant group effect ($F_{2,19}$=5.41, p=0.013). However, post-hoc tests did not show any significant differences between the groups. Yet, mean values of corticosterone levels indicate, that the group difference might be caused by the high levels of the NAB animals

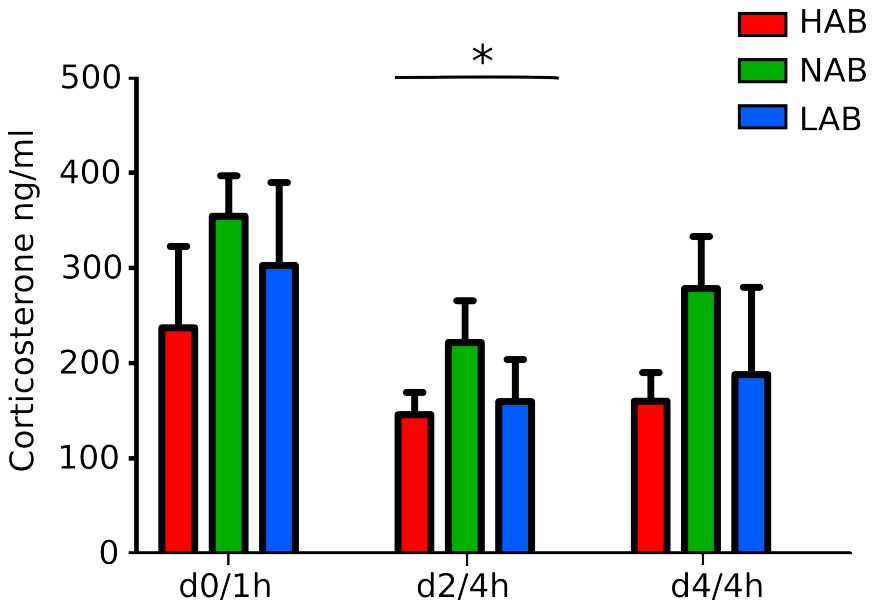

Figure 3.15: Endocrine measurements of HAB, NAB and LAB measurements after Mn^{2+} treatment. Corticosterone levels at different time points after injections for HAB, NAB and LAB animals. The first time point shows highest corticosterone levels. The asterisk indicates the found group effects. However, post-hoc comparisons did not reveal any significant differences. High corticosterone levels in NAB animals at all time points might drive the group effect. *: $p<0.05$ (significant group effect).

at every time point. Furthermore, a significant effect of time ($F_{2,38}=1.86$, $p=0.17$) or time×group effect ($F_{4,38}=0.4$, $p=0.81$) was not found.

3.3.2 MEMRI

Figure 3.16 shows the results obtained from the SPM full factorial analysis. The highlighted regions showed a significant main effect of group. The PC, BNST, septum, GP, parts of the HPC, PAG, IC, the right parabrachial nucleus (PB) and the cerebellar nucleus (CN) were found to be differentially activated between the three groups. The peak voxel estimates showed that the group effect reflects without exception a HAB>NAB>LAB contrast.

Thus, an independent two sample T-test was used to compare HAB against LAB animals. All findings could be confirmed and additionally, the right CeA was found to be more activated in HAB animals as compared to LAB animals.

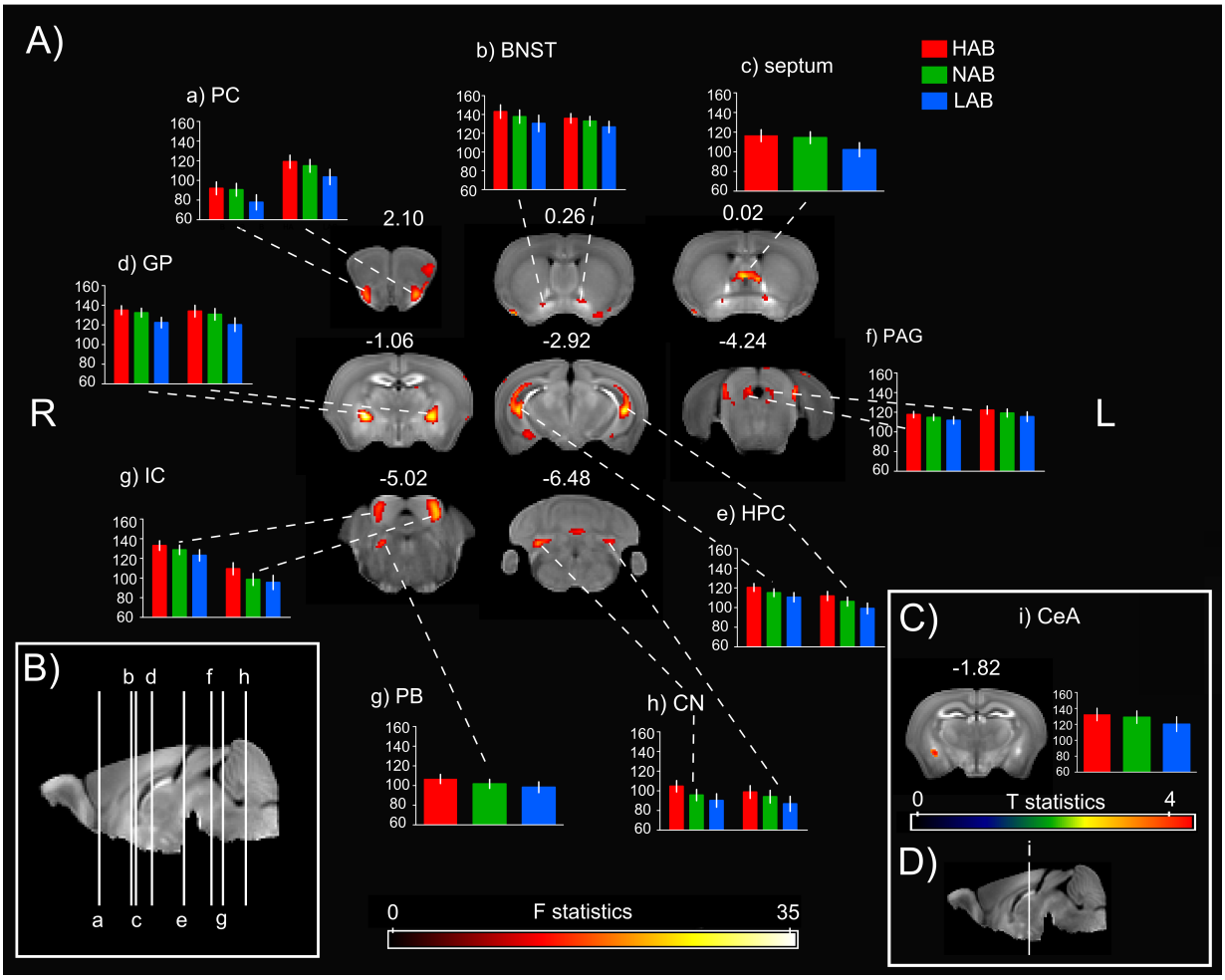

Figure 3.16: Activity maps reflecting trait anxiety. A) Clusters represent areas with significant main effect of group (F-test ($p_{FDR} < 0.01$)), overlaid on the mean T1w1 image of the study. Graph bars represent contrast estimates for the three different groups extracted from the peak voxels of the corresponding areas. All areas reveal the same activation pattern (HAB>NAB>LAB). Numbers above the brain slices indicate corresponding Bregma coordinates. B) Sagittal view indicating the position of slices shown in A). C) Independent sample T-test (HAB>LAB) showing stronger activation for the right CeA in HAB as compared to LAB animals ($p_{FDR} < 0.01$). Graph bar represents contrast estimates for HAB and LAB as extracted from the peak voxel. The number above the brain slice indicates corresponding Bregma coordinate. D) Sagittal view indicating the position of the slice shown in C).

Most of the observed effects were found bilaterally. Only the PB and the CeA were identified on the right hemisphere.

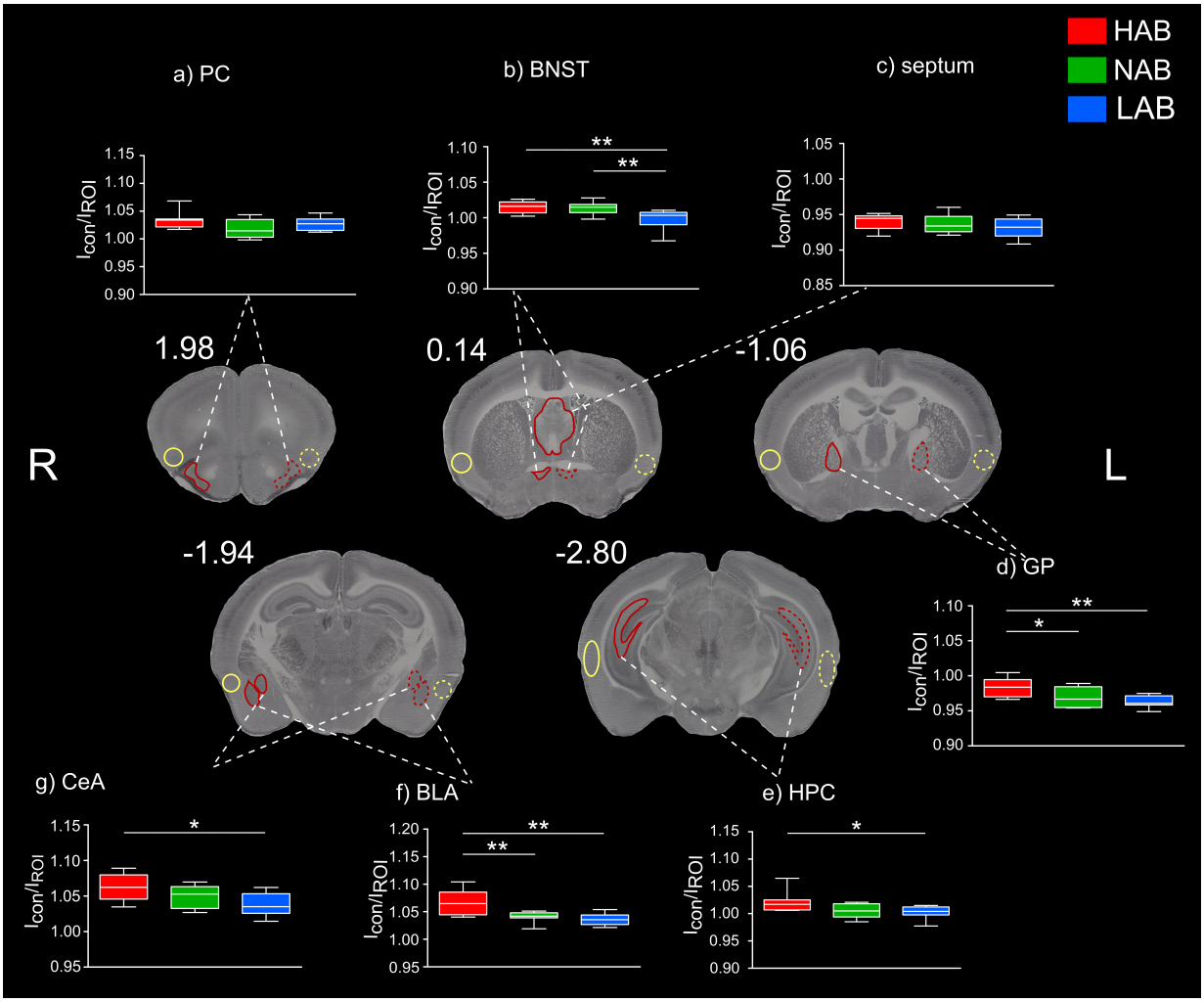

Figure 3.17: Slices stained for CO activity. Due to sometimes asymmetric cutting of the histological slices regions were not analyzed on the same slice for left and right. Therefore dotted lines indicate that region may have been defined on another slice. Box plots show reciprocal values of grey levels of ROIs (red on the brain slices) divided by grey levels of cortical region (yellow on the brain slices). *: $p<0.05$, **: $p<0.001$

3.3.3 Histology

To validate the MEMRI findings CO stained brain slices of an independent sample of HAB, NAB and LAB mice were analyzed. ROIs were chosen based on MEMRI findings. Additionally, the basolateral amygdala (BLA) was analyzed. As the brain slices showed bad quality from the PAG to the CrB the analysis of the PAG, PB, IC, and the CN was not possible.

	BNST	GP	HPC	CeA	BLA
HAB vs LAB	0.008	0.002	0.026	0.011	0.003
HAB vs NAB	0.974	0.039	0.052	0.143	0.007
LAB vs NAB	0.006	0.148	0.720	0.191	0.672

Table 3.7: P-values of the post-hoc comparisons of the F-tests in regions with significant group effect. As the HPC shows a statistical trend in the group effect post-hoc comparisons were included.

Results are shown in figure 3.17. A multiple comparison analysis revealed a significant group effect in the BNST ($F_{2,17}$=6.43, p=0.008), GP ($F_{2,17}$=6.88, p=0.006), CeA ($F_{2,17}$=4.05, p=0.036) and BLA ($F_{2,17}$=7.18, p=0.005). The HPC missed significance by a narrow margin, only showing a statistical trend ($F_{2,17}$=3.39, p=0.058). The septum and PC failed to show significant differences between the three different strains.

Post hoc comparisons of ROIs which reached the level of significance revealed that all regions showed significantly more CO activation in HABs than in LABs.

3.3.4 Correlation analysis

Correlation analysis between the percentage of time spent on the open arms (%TOA) and the gray level values (CO), or the signal intensities gained from the extraction of peak voxel values on MEMRI images was performed for the regions found to be significantly different between the three different lines. The Spearman rank test revealed significant negative correlations for the BNST, the septum, GP, HPC, and the CeA for CO analysis (figure 3.19). For MEMRI analysis significant correlations were found in all the tested regions (figure 3.18).

As animals from the MEMRI and histological study resulted from different generations, %TOA were measured by different scoring systems, thus resulting in the different %TOA in figures 3.18 and 3.19.

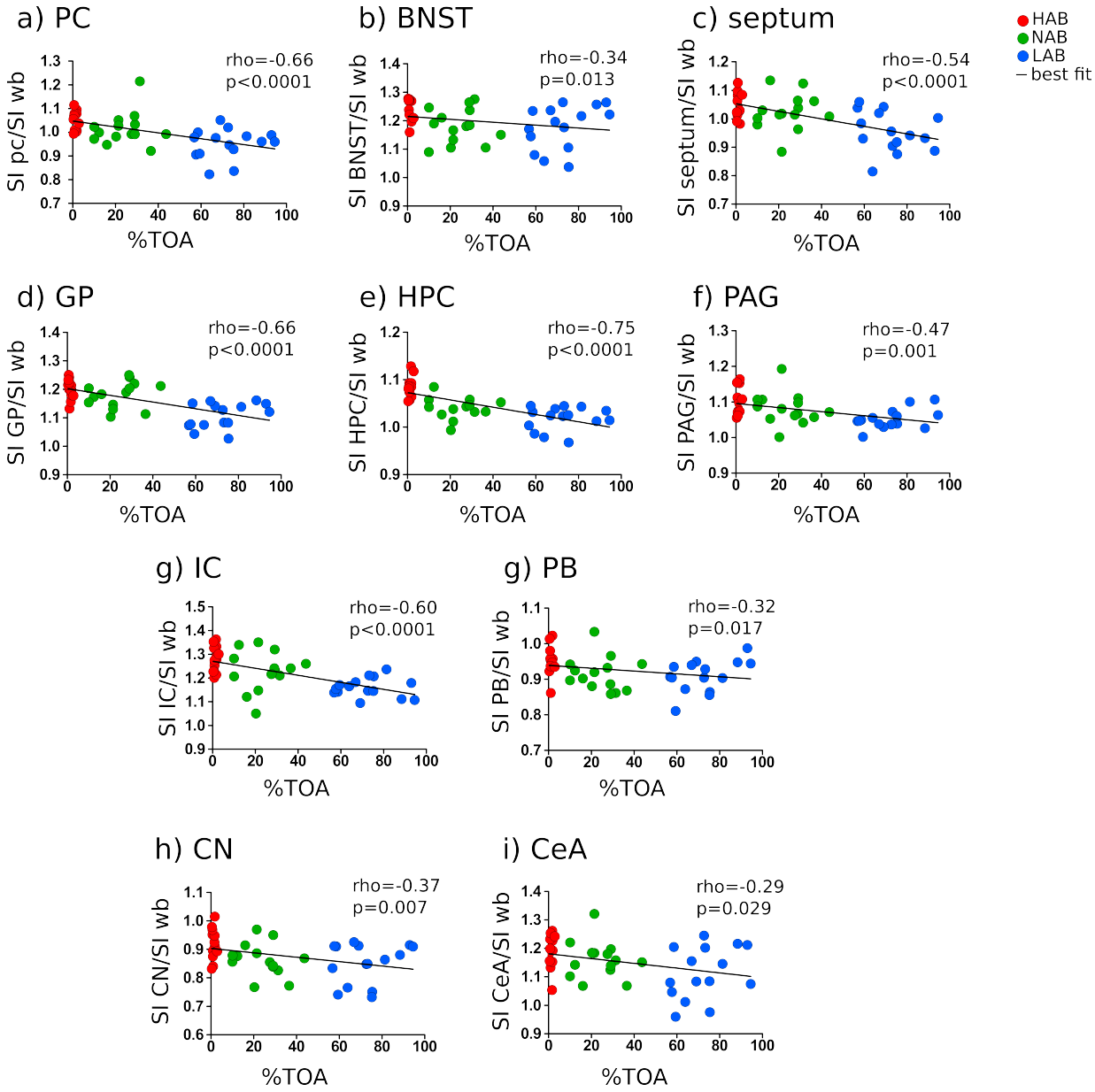

Figure 3.18: Correlation analysis of MRI signal intensities with %TOA. Correlation analysis of the signal intensity of the respective ROI corrected for wb intensity with the percentage of time spent on the open arms. Coefficients of correlation ρ and p values revealed by the Spearman rank test are given for the different regions. All regions show significant negative correlations with modest (BNST, PB, CN, CeA) to strong (IC, GP, HPC) correlation.

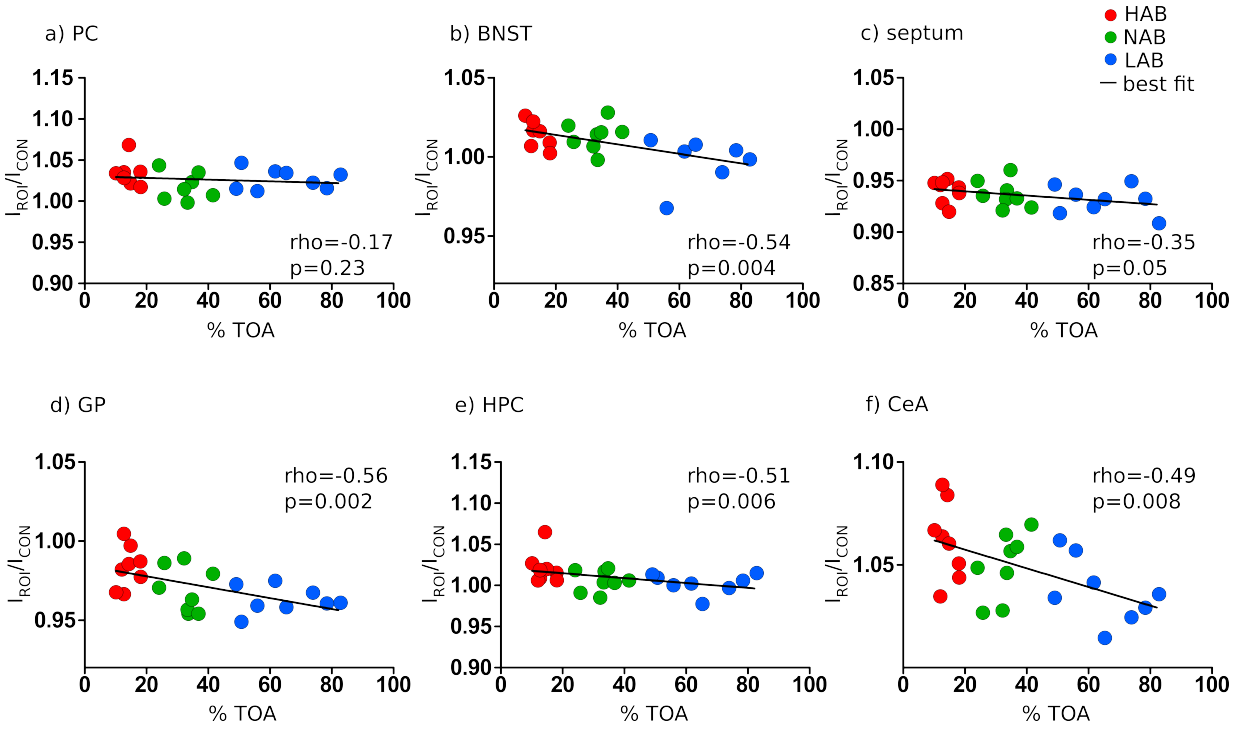

Figure 3.19: Correlation analysis of CO activity grey level intensity with the time spent on the open arms. Coefficients of correlation ρ and p values revealed by the Spearman rank test are given for the different regions. All regions but the PC show significant negative correlations.

Chapter 4

Discussion

In this thesis a fractionated Mn^{2+} injection protocols was established to minimize toxic side effects of Mn^{2+}, while obtaining satisfactory MR image contrast enhancement. Furthermore, the temporal evolution of signal intensity within this established injection protocol was investigated in the second study. Lastly, MEMRI was used in a mouse model of extremes in trait anxiety to show the applicability of MEMRI in functional studies and to visualize the neurocircuitry of anxiety. To verify the results obtained from MEMRI histological staining for CO activity was performed. The results will be discussed in the following three sections.

4.1 Study I: Fractionated MEMRI

The study investigated the effects of systemic Mn^{2+} application on vegetative, behavioral and endocrine measures on BL6 mice. As an overall summary it was found that the application protocols involving repeated injections of 30 mg/kg doses of $MnCl_2 \cdot 4H_2O$ showed the least effects on the health and well-being of the animals, while still producing satisfying MR image contrast.

While a single or even repeated application of 99 mg/kg of $MnCl_2 \cdot 4H_2O$ is notably well tolerated in rats [162] and CD1 mice (own observation), it leads

to severe health impairment or even death in BL6 mice. The delivery of a total dose of 240 mg/kg over the course of 8 days, however, had only minor consequences on vegetative functions, behavior and stress responses. Of the three proposed injection schemes, a daily injection of 30 mg/kg over 8 days was found to be optimal in reducing systemic side effects, while delivering satisfying contrast enhancement in MEMRI images. In particular, hypothermia and hypolocomotion were less pronounced than in the $3 \times 60/48$ application protocol. The application of Mn^{2+} led to nominally higher corticosterone levels 4 and 12 hours after the first treatment. However, on day five of the experiments corticosterone levels returned to levels of the control group which may indicate habituation to Mn^{2+} as a stressor. This conclusion is supported by the result that effects on body weight were only transient, with recovery after two days. Although the $8 \times 30/24$ protocol delivered the highest overall dose, it led to less severe side effects than the $3 \times 60/48$ protocol. This implies that toxic effects are not merely dependent on the total delivered dose of Mn^{2+} but also on the mode of application, i.e. single or fractionated delivery. Fractionated delivery seems advisable to avoid single dose toxicity and to exploit the fast recovery of corticosterone levels, body temperature and locomotion following low dose application. This becomes particularly useful when studying sensitive mouse models with potentially compromised health (e.g. genetically modified animals, mice at early developmental stage, or old mice) because unnecessary stress for the animals can be avoided with the fractionated approach.

The $8 \times 30/24$ protocol not only provided least toxic side effects of all tested protocols, but also provided the best differential contrast between brain structures as measured by RIs in the acquired T1w images. Studies performed on rats showed that fine structures of the OB and the CrB could be distinguished using MEMRI [163, 164]. The present study could confirm these findings in

mice, which have much smaller brain volumes. More specifically, the fine structures of the OB and the CrB could be distinguished with every Mn^{2+} application protocol. Layers of the RSG, however, only became distinguishable in animals treated with the $8 \times 30/24$ injection protocol. It has been shown before, that the labeling of laminar structures with Mn^{2+} correlates with standard histological neuronal staining methods [165]. Similar to a study by Lee and colleagues [98], who showed that MEMRI is able to resolve fine structures of the mouse cortex using single high doses of Mn^{2+} (88 mg/kg or greater), the present study showed that visualizing fine brain structures is also possible by applying fractionated doses of Mn^{2+} in mice.

Contrast differences obtained from the control group indicate a natural variation in T1w contrast, which might be traced back to cell density differences of brain structures (see section 4.2). This contrast seems to be flattened by the administration of Mn^{2+} of a total dose of 180 mg/kg, but enhanced upon administration of higher total dosages. The COV showed that this effect seems to be more dependent on the total delivered dose than on the fractionated treatment with controls showing the lowest variation followed by the groups that received a total dose of 180 mg/kg ($3 \times 60/48$ and $6 \times 30/48$) and 240 mg/kg ($8 \times 30/24$) showing the highest COV. However, the possibility that the higher regional and overall contrast of the $8 \times 30/24$ group was influenced by the shorter inter-injection interval cannot be ruled out. Moreover, the $8 \times 30/24$ protocol is limited to 8 days of injections at maximum. While this provides a reasonable experimental time frame, it cannot be excluded that further extending the low dosage application protocol would lead to even better contrast enhancement without further impairing the animals well-being.

4.2 Study II: Dynamical behavior of manganese in the $8 \times 30/24$ injection protocol

In this study, the dynamical behavior of the $8 \times 30/24$ injection protocol was investigated. Measurements of the accumulation and clearance processes were assessed through the measurement of signal intensities of T1w images at different time points. Signal intensities of the accumulation process were found to be in accordance with a linear model, increasing from control level to the level after eight injections. Further, contrast enhancement increased linearly, with best obtained differential contrast between brain structures after eight injections. No saturation was measured, indicating, that with continued injections contrast enhancement can be improved. This could be important for the visualization of fine brain structures as shown in chapter 3.1.4.

The steepest increase in MEMRI image intensity was found in the GP, IC, BNST, CeA, and CA3 region of the HPC, which is in accordance with previous qualitative observations [112]. Intermediate accumulation was observed in the CA1/2 region of the HPC, MB structures, SC, Nacc, and septum. All other regions showed little Mn^{2+} uptake, especially the DG and all cortical regions exhibited shallow increase in RI. However, all slopes deviated significantly from zero.

As signal intensities of all ROIs were in accordance with a linear model, it is concluded that none of the investigated ROIs showed a saturation effect. These results indicate, that regional image intensity reliably reflects the underlying basal, neuronal activation pattern using a fractionated application with daily repeated injections of 30 mg/kg over 8 days. However, it cannot be excluded that the application of a stressor would lead to saturation.

In MEMRI, the hippocampal formation generally shows strong T1w image contrast enhancement. Especially the CA3 region of the HPC, which appears

to exhibit one of the highest signal intensities in MEMRI images, however, it does not exhibit the steepest slope (region with fourth steepest slope). This might be ascribed to the fact that already at control level, the CA3 region displays relatively high signal intensity compared to other brain regions. The relatively bright signal in the CA3 even before Mn^{2+} application indicates a smaller T_1-relaxation time, which results from "high cellular density or tight packing" [112], and thus leads to a faster T_1- relaxation process. As stated by Watanabe et al. (2004), differences between the accumulation of Mn^{2+} in the CA3 and CA1/2 region of the HPC might be traced back to functional differences in the electrophysiological properties of CA1/2 and CA3 [166]. Spontaneous action potentials have been detected from the CA3 pyramidal cells, but not from cells of the CA1 region, using extracellular recordings [167], indicating, that CA3 cells are more excitable than those of CA1 [166]. Further, low voltage-gated Ca^{2+} channels were found to be abundant in CA3 pyramidal neurons as compared to those of the CA1 region [168]. As low voltage-gated Ca^{2+} channels open more easily, their abundance in the CA3 region might explain the higher accumulation in the CA3 as compared to the other regions of the HPC [166]. Mn^{2+} accumulation in the HPC has been exploited to increase tissue contrast in rodents in morphometric studies [120]. It was furthermore reported that the application of Mn^{2+} does not impair memory processes [169, 170]. However, other data indicate that some aspects of spatial learning may be negatively affected [171, 172]. A single application of 80 mg/kg $MnCl_2$ led to a mild, but detectable, decrease in the postsynaptic response in the DG [173].

The IC, which also exhibits high signal intensities in MEMRI images (figure 3.9 A i) exhibited third steepest slope in the present study. It has been shown that the IC exhibits large basal levels of oxidative metabolic capacity using CO activity staining [174]. Since the results of study III of the present work

indicate, that CO activity staining and MEMRI reveal the same activation patterns, it might be concluded that the high accumulation of Mn^{2+} in the IC results from high basal activity of IC neurons.

The GP belongs to the basal ganglia and is usually associated with motor behavior. Early symptoms of manganism can be linked to the rapid accumulation of Mn^{2+} in the GP. Bilateral hyper-intensities in the GP are an early indication of Mn^{2+} intoxication and correlate positively with Mn^{2+} concentrations in the blood [175]. Similarly, increased Mn^{2+} in the GP were found in patients suffering from liver disease, like cirrhotic patients [176] or patients with biliary atresia [177]. Both conditions prevent the successful clearance of Mn^{2+} from the body. In rhesus monkeys it has been shown that upon inhalation Mn^{2+} accumulation was the strongest in the OB, the pituitary gland and the GP [159]. In the present study high accumulation of Mn^{2+} is represented by the second steepest increase in signal intensity of all investigated ROIs (figure 3.9 A d).

However, the region found to exhibit strongest increase in RI due to Mn^{2+} accumulation in the present study was the CeA. The CeA is known to play a major role in emotional processing [178]. However, its propensity to take up Mn^{2+} has been barely studied quantitatively. As mentioned earlier, the distribution of Mn^{2+} throughout the brain is primarily dependent on the distribution of Ca^{2+} channels and their propensity to open. Translating this to the findings in the CeA one might conclude that Ca^{2+} channels are more abundant in the CeA than in other regions, that the CeA has, as the CA3 region of the HPC, a high cell density and that its cells are more excitable than those of other regions. The actual reasons of why the CeA exhibits highest Mn^{2+} accumulation in the present study is unknown.

As already mentioned in the results section, T1w-image intensities enhanced through Mn^{2+} showed huge standard deviation differences between

those animals with a higher number of injections compared to control animals or animals receiving only one or two injections of $MnCl_2$. Closer inspection of the individual data sets revealed that lower intensities were consistently found in specific animals thus reflecting inter-individual variance. The spread in intensities may reflect individual differences in systemic elimination and excretion of Mn^{2+}, and in transport and delivery to the brain. Further, standard deviations for ROIs with high Mn^{2+} accumulation were higher than for ROIs with lower Mn^{2+} accumulation. It would be advantageous if signal intensities could be more reliably normalized. In this study, skull muscular tissue was used as reference region, which does not fully reflect inter-individual differences in cerebral Mn^{2+} uptake. However, extra cerebral tissue should be used, as whole brain intensity and specific regional intensities all show a linear increase during the application protocol.

Along with the accumulation process, the clearance of Mn^{2+} from the brain was also studied. Data revealed that two weeks after the last injection most of the investigated brain regions still showed significantly higher signal intensities than the control condition for corrected α-level. This indicates that when used in longitudinal studies a considerably longer delay than two weeks should be considered between repeated experiments. Further, some of the investigated ROIs exhibited significantly higher RIs than control condition four weeks after the last injection for nominal α-level. Thus, to ensure total clearance of Mn^{2+} from the brain a delay of at least eight weeks should be considered. Best fit half-life times were found to range between 5.5 and 7.3 days, dependent on the specific brain region. However, evaluation of the 95% CI showed that the uncertainty of the measurement was high, and also allowing for half-life times up to 17 days for the CeA. This high uncertainty might be ascribed to the sample sizes used in this study as time point zero includes 45 data points, whereas all other time points included 10 or less data points and high

standard deviations for time points 0 and 1 after the last injection. The width of the 95% CI was strongly dependent on the ROI, with wider CIs for regions showing higher propensity to take up Mn^{2+}, such as the CeA, GP and IC. As in the accumulation process, standard deviations for time points which showed high MEMRI contrast (first scan and scan one week after the last injection) were huge and declining with further distance to the last injection. These standard deviation differences might further explain the differences in the width of the 95% CI. The differential contrast enhancement between brain structures also decayed in an exponential manner, just as RI.

ROIs showing longest half-lives were the PAG, CeA and EC. Shortest half-lives were found in the Nacc, GP, septum and CA3 region of the HPC. All other investigated ROIs exhibited intermediate values of half-lives. Generally, regions with high accumulation also showed short half-life with exception of the CeA. The distributions of half-lives throughout the brain should be further investigated. However, the longer duration of the clearance of Mn^{2+} than uptake indicates that transport out of the brain is passive and thus diffusion mediated (see section 1.3.5).

The values found in the present study are in line with previous qualitative estimates from MEMRI. Pautler et al. (2003) found that 10 days after intra-cerebral nanoliter injection of Mn^{2+} as positive contrast enhancement had vanished [105]. Furthermore, Aoki et al. (2004) found that MRI signal intensities were not significantly different to control after two weeks after single, systemic application of 140 mg/kg Mn^{2+} [97]. Yet, these studies did not determine half-lives. However,the findings of the present work and studies of Pautler et al. and Aoki et al. are in remarkable contrast to an earlier report by Takeda et al. who showed that half-lives of intravenously injected manganese were 51 to 74 days in the rat brain, using autoradiographic measurements [109]. Similarly, Dorman et al. [159] measured tissue manganese concentra-

tions after subchronic (65 days) exposure to air containing manganese sulfate. A clearance time of 45 to 65 days after termination of exposure was determined in rhesus monkeys. After 45 days, Mn^{2+} tissue concentration was still significantly higher in the GP and putamen, as compared with the control group without manganese exposure, suggesting a half-life of about 18 days in these structures. The great discrepancy between the present study and these studies might be explained by the very different times of exposure to Mn^{2+} and the different routes of Mn^{2+} application. Inhalation exposure leads to increased manganese accumulation in the lung, which was shown to contain manganese even after a recovery of 19 weeks following exposure to manganese dust [179]. This deposit of manganese in the lung might be a source of continuous Mn^{2+} supply even after the cessation of the external source and thus lead to much longer half-lives than measured in the present study. Furthermore, used species were also different. In the present work mice were used, which might show a higher metabolic rate than rats and monkeys and thus faster clearance of Mn^{2+} from the brain.

4.3 Study III: Application of MEMRI in a mouse model of extremes in trait anxiety

In the last study MEMRI was applied to a mouse model of extremes in trait anxiety. Further, results were, for the first time, compared to an independent histological functional staining method (CO activity).

MEMRI, being based on local accumulation of paramagnetic ions in activated brain regions, allows for a hypothesis free analysis of the whole brain. The PC, BNST, septum, GP, parts of the HPC, the right CeA (T-test), PAG, IC, the right PB, and parts of the CN were found to be differentially activated in the three tested groups, with the strongest activity in animals with high

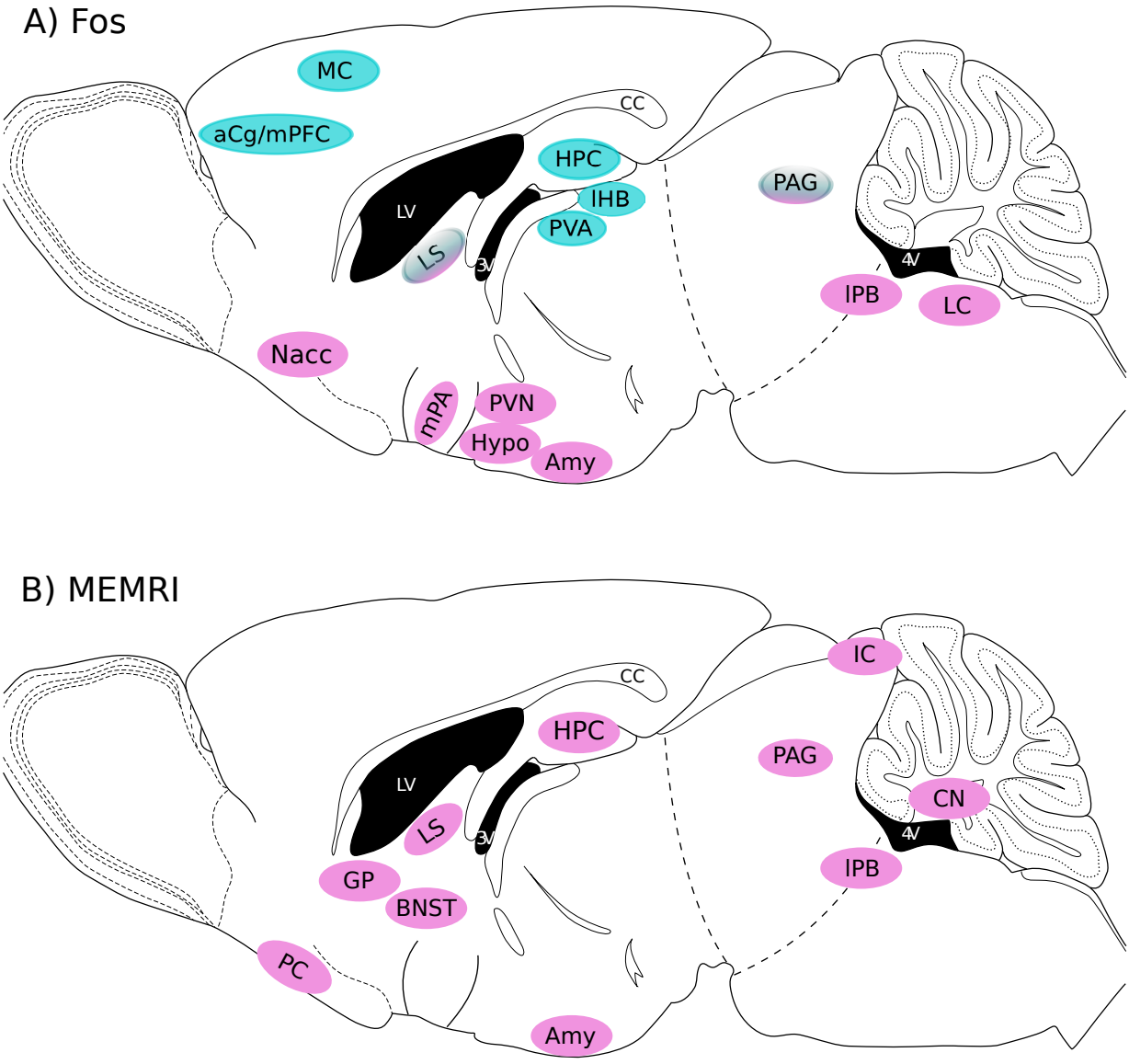

Figure 4.1: Sites of neuronal activation as found by MEMRI B) compared to Fos staining A) (figure 1.9). It is noticeable that MEMRI could not detect regions with decreased c-Fos expression after one of the applied stressors in HAB animals (blue). aCg: anterior cingulate cortex; mPFC: medial prefrontal cortex; MC: motor cortex; HPC: hippocampus; PVA: paraventricular thalamic nucleus; lHB: lateral habenular nucleus; LS: lateral septum; mPA: medial preoptic area; Nacc: nucleus accumbens; PVN: paraventricular hypothalamic nucleus; Hypo: hypothalamic area; Amy: Amygdala; PAG: periaqueductal gray; lPB: lateral parabrachial nucleus; LC: Locus coeruleus; CC: corpus callosum; LV: lateral ventricle; PC: piriform cortex; GP: globus pallidus; BNST: bed nucleus of the stria terminalis; CN: cerebellar nuceus; 3V: third ventricle; 4V: fourth ventricle.

anxiety-related behavior. MEMRI results were validated by analysis of brain slices stained for CO activity. However, due to low quality of brain slices at the level of the PAG and further caudal regions, analysis of CO activity could not be performed in the PAG, IC, CN and PB. These results demonstrate that both MEMRI and CO staining were able to identify the same brain regions showing differential activity as related to trait activity. Whole brain voxel-wise statistical comparisons are easily performed in MEMRI images. In contrast to histological staining methods MEMRI does not lead to physical demolition of brain structures. Therefore, MEMRI may be a valuable tool to assess cerebral activity and to guide subsequent histological analysis by identifying ROIs which might be crucial for the investigated trait or disease.

Figure 4.1 A shows the brain regions which were found to be part of the neurocircuitry for anxiety, as assessed by c-Fos staining, in comparison to brain regions identified using MEMRI (figure 4.1 B). To integrate the identified brain regions into todays literature, each brain region will be discussed in detail.

4.3.1 Piriform cortex

The PC has been reported to be activated in response to different anxiety and stress models. For example, it showed increased c-Fos expression in rats after exposure to the open arm [180] or foot shock avoidance test [181].

4.3.2 The septo-hippocampal system

Since the HPC and the septum are integral parts of the septo-hippocampal system they will be discussed together. They have both been found to have an involvement in anxiety mechanisms. This was shown by differential c-Fos responses between HABs and LABs following exposure to the open arm of

the EPM [148] or to social defeat [149]. Furthermore, septal lesions led to increased time spent on the open arm and to a decreased time spent burying the shock probe in the shock probe burying test [182].

The findings from this work on the HPC are of particular interest, as neither the dorsal nor the ventral HPC, but rather the intermediate part of the HPC was found to be hyper-activated in HAB animals as compared to LAB animals. In a previous work, Fanselow et al. suggest the separation of the HPC in three, rather than only two, parts: the dorsal, the intermediate and the ventral part, based on gene expression in the different parts [183] . The dorsal HPC is classically involved on cognitive processes of learning and memory associated with navigation, exploration, and locomotion and the ventral part is associated with motivational and emotional behavior, whereas the intermediate part might be involved in translating cognitive and spatial knowledge into motivation and action critical for motivation [183]. Our findings indicate that the intermediate part plays a major role in anxiety possibly by combining both the function of the dorsal and the ventral parts.

4.3.3 Globus pallidus

The GP is usually associated with motor behavior and is also thought to be one of the brain regions with highest Mn^{2+} accumulation (section 4.2). It has been shown that the GP plays an important role in performing aversive behavior based on emotions, including fear and anxiety [184]. Moreover, it has been shown that local administration of the anxiolytic drugs 5-HT and L-GA directly into the GP effectively counteracted the anxiety state in the threatening situation avoidance test, indicating that the neurotransmitter systems of the GP are involved in anxiety [184].

4.3.4 Bed nucleus of the stria terminalis and amygdala

The BNST and the CeA project to areas that are involved in the processing of fear and anxiety [185]. Furthermore, the BNST and the CeA are strongly connected with each other; fibers from the basolateral amygdala, which project to the BNST pass through the CeA and the lateral division of the CeA itself projects to the BNST [186]. It has been furthermore shown that the BNST is involved in behavioral paradigms that are manipulated by long-lasting stimuli and in paradigms that evaluate the persistent influences on behavior by brief stressors [185]. However, it has not been shown that the BNST is involved in behaviors caused by short-lasting threats, in which the danger period had a clear offset [185]. Therefore Walker et al. conclude that the BNST plays a special role in mediating anxiety, but not fear, with anxiety considered as a state of concern which is not related to immediate danger or threats.

Since the mid-nineties it has been well established that the amygdala plays a crucial role in mediating fear and anxiety [178]. It has been shown that anxiolytic drugs of all chemical classes act directly on the amygdala to reduce arousal associated with anxiety [186].

In the present study the BNST as well as the CeA were found to be hyperactivated in HAB animals as compared to LAB animals, with NAB animals showing intermediate activation.

4.3.5 Periaqueductal gray

The PAG is commonly separated into two parts, the dorsolateral PAG (dPAG) and the ventral PAG (vPAG). Both parts seem to play different roles in defensive reactions [187]. Electrical and chemical stimulation of the dorsal PAG induce panic-like behavior in rodents [188, 189], indicating an involvement of the dPAG in active forms of defensive behaviors. Furthermore, malfunction-

ing of the dPAG might be related to panic attack [187]. In contrast, the vPAG is associated with the occurrence of defensive freezing [187]. Explicit experiments with HAB animals showed increased Fos expression following exposure to airjet and administration of the anxiolytic drug FG-7142 [143]. Moreover, increased c-fos expression was found in HAB animals after the exposure to open arm of the EPM [129]. The hyper-activation of the PAG as found in the present work are therefore in line with commonly used histological methods.

4.3.6 Inferior colliculi

The IC belong to the auditory system of the rodent brain. Since electrical stimulation of the IC leads to fear like behavior (freezing, flight behavior) they have been proposed to belong to the brain "aversion system" [190] that also includes the hypothalamus, the amygdala, and PAG. The relationship between anxiety and the auditory system has to do with neurons of the IC acting as filters for sounds that require immediate action, such as sounds made by prey, predator or conspecifics [191]. Therefore, findings of the present work showing hyperactive inferior colliculi in HAB mice as compared to LAB mice, with NAB mice showing intermediate activity, is not surprising.

4.3.7 Parabrachial nucleus

The parabrachial nucleus is responsible for regulating the respiratory rate and cardiovascular changes. Projections from the BNST and the CeA to the PB might therefore be involved in respiratory as well as cardiovascular changes during fear and anxiety [192]. Furthermore, the PB network seems to be the core of the circuitry that regulates autonomic control, vestibule-autonomic interactions and anxiety [193]. The PB network thereby consists of the PB itself and its reciprocal relationship with the extended central amygdaloid

nucleus, which again projects to the BNST, the infralimbic cortex and the hypothalamus [193].

4.3.8 Cerebellar nuclei

The CrB has long been thought to be predominantly active in motor behavior. However, it has been shown that the cerebellar nuclei are also involved in behavior and cognition [194]. In 2010 it was shown that upon stimulation of the PAG c-fos expression was decreased in the cerebellar nuclei, indicating involvement in the anxiety circuitry [195]. The findings presented in this work affirm an involvement of the cerebellar nuclei in anxiety-related behavior and might serve as encouragement for further investigations with this region in combination with anxiety.

Though all the regions revealed by hypothesis-free MEMRI analysis belong to a network that is excited in anxiety as has been shown in previous studies, some regions have just been detected to play a role in anxiety or have not been extensively study, such as the GP, BNST, CN or PC. This shows that MEMRI is superior to *ex vivo* staining methods in revealing target regions for further research on anxiety-related behavior. Further, the conducted study is an indication, that MEMRI is more suited for functional imaging in rodents compared to BOLD imaging, as only the read-out of brain activity is performed under anesthesia.

However, it has to be noted that the application of Mn^{2+} does resemble an acute stressor to which animals habituate upon repeated application [123]. Results from endocrine secretion showed a significant effect of mouse line. However, post-hoc tests did not show significant differences between the HAB, NAB and LAB animals. As mentioned in the introduction, HAB, NAB and LAB animals do not show significantly different corticosterone levels under basal conditions [145]. It might therefore be concluded, that MEMRI

findings are not related to different stress levels of animals after the injections. Further, these findings render the decision for using the 3×60/48 protocol, to reduce handling stress, instead of the 8×30/24 protocol reasonable. The pathway visualized through MEMRI consists only of parts of the neurocircuitry of anxiety and regions such as the medial prefrontal cortex or the thalamus, which belong to the regions showing diminished c-Fos expression after application of a stressor in HAB animals (figure 4.1), could not be visualized. However, changes in signal intensity due the Mn^{2+} ion are hard to interpret. MEMRI measurements of signal intensity changes are a measurement of an ensemble of activation and inhibition. Thus, no change in signal intensity either means, that there is no activation, or that excitation and inhibition are balanced [196]. Furthermore, spontaneous opening of Ca^{2+} channels also leads to accumulation of Mn^{2+}

However, changes in signal intensity due to MEMRI are hard to interpret as the method cannot discriminate between excitation and inhibition in different populations of neurons in the same region. Therefore, the change in SI is a net measurement of activation obtained from both, excitation and inhibition. Therefore, no change in SI can mean either that there is no activation, or that excitation and inhibition are balanced [196]. This might explain the lack of the inhibitory pathways in our findings as the influx of Mn^{2+} through spontaneous activation might overwrite the effects which might result from inhibitory pathways.

In summary, this study provides first evidence that trait anxiety can reliably be detected *in vivo* using MEMRI.

Chapter 5

Concluding remarks

MEMRI opens the possibility to study complex paradigms in freely behaving animals, as only the read-out of the cerebral Mn^{2+} accumulation requires sedation of the animals. However, a major drawback of its use as MRI contrast agent is its toxicity when applied in too high doses. Thus, the first aim of the presented thesis was to establish fractionated MEMRI to reduce toxic side effects.

In the first study systemic side effects were substantially reduced by applying $MnCl_2$ in small dosages. However, to ensure satisfactory MRI contrast repeated applications were necessary. Hypothermia and hypolocomotion as induced by the application of higher dosages (60 and 99 mg/kg) could be reduced by the delivery of 30 mg/kg in a fractionated manner. Furthermore, stress induced by the systemic delivery of Mn^{2+} could be reduced by the application of smaller dosages, as measured by peaks of corticosterone secretion to different time points after the injections. Yet, it has been shown that the procedure of ip injections may lead to severe stress and the alteration of gene expression and brain activation in animals [197]. Although the animals habituate to ip injections as a stressor it might be meaningful to avoid repeated injection. The implantation of osmotic mini-pumps into the peritoneum has been suggested as a promising alternative [170]. These provide a slow but

continuous source of Mn^{2+} application, thus avoiding peaks in corticosterone secretion as well as the accumulation of huge amounts of Mn^{2+} all at one time in the brain.

It has been shown that the delivery of Mn^{2+} via intra-cerebral injections leads to neuronal damage of brain tissue [198]. Thus, histological investigations of neurotoxic effects on brain tissue of animals treated with the fractionated injection protocol might be useful, to assess the amount of damaged tissue. Especially the HPC seems to be targeted by Mn^{2+}, as a former study already showed comprised ability of hippocampal dependent spatial learning after the application of the suggested $8 \times 30/24$ application protocol [171].

Further, the study showed that excellent soft tissue is achieved with the suggested $8 \times 30/24$ fractionated application protocol. Even fine structures could be resolved by the fractionated application. Sampling at higher resolution should further improve visualization of fine structures and thus reduce artifacts arising through only reconstructing for higher resolution. However, sampling at higher resolution also means longer scanning times, thus increasing the time animals have to be anesthetized. Therefore, a balance between reasonable scanning time and resolution needs to be found.

In conclusion, the first study provides evidence that higher total doses of Mn^{2+} lead to improved general and between-region MEMRI contrasts while fractionated application minimizes adverse effects caused by the toxicity of Mn^{2+}. More specifically, it could be demonstrated that behavioral, vegetative and endocrine markers of stress are only minimally and transiently effected, when a fractionated application scheme with low single doses is used. MEMRI with fractionated Mn^{2+} applications is therefore particularly suitable for paradigms that probe the animals' stress system. It should be noted that effects are not readily visible in behavioral observations. It is therefore strongly recommended to not solely rely on general health assessment but to

also include physiological measurements for each particular study.

The second study investigated the temporal evolution of the MEMRI contrast of the $8 \times 30/24$ injection protocol. To do so, repeated readouts were applied during the accumulation as well as clearance process. The knowledge of the temporal evolution might help to optimize the timing of a specific task, if the paradigm cannot be continuously applied due to experimental reasons or habituation of the animal.

Results indicated that MR signal intensities did not saturate during the course of the injections. However, it cannot be excluded that the application of a stressor or other paradigms might lead to saturation effects. Thus, it still needs to be investigated, if the application of a physiological or psychological stressor in combination with the $8 \times 30/24$ protocol leads to saturation effects.

Furthermore, in order to be able to exploit one of the great advantages of using MEMRI as functional imaging tool, namely the performance of longitudinal studies, it needs to be ensured that all Mn^{2+} has cleared from the brain before another MEMRI session is started and inter-individual variances in Mn^{2+} excretion might be accounted for by choosing the right timing for the second MEMRI session. Results indicated, that at least eight weeks of delay should be considered between repeated experiments.

Further studies are needed to investigate the mechanisms that drive Mn^{2+} accumulation in the brain as well as clearance from the brain. For investigating, which Ca^{2+}-channels play a role in mediating Mn^{2+} influx into neurons, Ca^{2+}-channel knockout mice could be used for *in vivo* experiments. With *in vitro* brain stimulation the influx of Mn^{2+} could be artificially induced by the storage of brain slices in fluid doped with Mn^{2+}. The addition of Ca^{2+} blockers could then be used to investigate the role of different Ca^{2+}-channels.

The last aim of the presented thesis was to show the applicability of MEMRI in a mouse model of extremes in trait anxiety. Findings revealed a

whole network of brain regions to be hyper-activated in HAB animals as compared to LAB animals, with NAB animals expressing intermediate activation. The integration of the findings of the present thesis into todays literature indicated that the found differential activation patterns were mainly anxiety related. The results could be verified by histological staining for CO-activity, providing first evidence that trait anxiety can reliably be detected *in vivo* using MEMRI. The advantage of the unbiased approach using hypothesis-free whole brain analysis might help in identifying brain regions for analysis in histological studies which were not targeted before in the investigated question. Further, the modulation of brain regions, pharmacologically or psychologically, which are not so well known to play a role in anxiety-related behavior, might further elucidate their function in trait anxiety.

Generally, MEMRI as a functional imaging tool faces several challenges, such as the identification of the true neuronal origin of Mn^{2+}-induced contrast and its quantitative evaluation as a measure of neuronal activity [199]. The use of T_1-weighted imaging needs a reasonable control region to correct signal intensities. Thus, T1w imaging only enables the measurement of qualitative changes of T_1-relaxation times. The use of pulse sequences which directly measure T_1-times, and thus provide quantitative measures, would improve the use of MEMRI. However, using standard measurements methods, such as inversion recovery, result in unacceptable long scanning times [200]. Much faster and newer scanning methods for T_1-mapping are available, however, not yet implemented on the used scanning system.

Further, data analysis as presented in this work was carried out using study-wise templates for spatial normalization. However, the use of a template consisting of different studies (mastertemplate), would even more generalize data analysis. As the definition of brainmasks and ROIs would then be dispensable it would also be more time efficient. Thus, all future studies should be spa-

tially normalized to the mastertemplate. Large differences in ventricle sizes, as present between different mouse strains, as BL6 and CD1 mice, render the normalization procedure very inaccurate. Hence, mastertemplates should be created for each mouse strain separately.

There are extensive possibilities for future applications of functional imaging studies using MEMRI. The possibility to carry out longitudinal studies enables the measurements of brain activity changes after pharmacological interventions. Furthermore, MEMRI facilitates the identification of brain regions between different mouse lines of selectively bred animals, as hypothesis free whole brain analysis becomes possible. When looking for ROI specific changes in brain activity hypothesis free whole brain analysis is superior to classical ROI analysis, as not only chosen ROIs are analyzed. However, when looking for effects affecting the whole brain, as in Study II of the presented work, ROI analysis provides better insight into activation patterns.

In summary, the present thesis provides a robust fractionated MEMRI method for assessing trait specific cerebral activity *in vivo*. It is not limited to trait anxiety and thus can readily be applied to other traits and diseases. As longitudinal studies become possible neuronal activation patterns can be modulated pharmacologically and psychologically and their alterations can be assessed *in vivo* after the intervention. After thorough literature search, the presented doctoral thesis was found to be the first work to combine MEMRI with SPM data analysis on hypothesis free voxel-by-voxel whole brain basis and the first work to verify trait specific cerebral activity differences measured with MEMRI with a histological functional staining method (CO-activity).

Bibliography

[1] F. Bloch, , W. W. Hansen, and M. Packard. Nuclear Induction. *Phys. Rev.*, 69:3–4, 1946.

[2] E. M. Purcell, H. C. Torrey, and R. V. Pound. Resonance absorption by nuclear magnetic moments in a solid. *Phys Rev*, 69:1–2, 1946.

[3] R. Damadian. Tumor detection by nuclear magnetic resonance. *Science*, 171(976):1151–1153, 1971.

[4] P. C. Lauterbur. Image formation by induced local interactions: examples eploying nuclear magnetic resonance. *Nature*, 242:190–191, 1973.

[5] A. Kumar, D. Welti, and R.R. Ernst. NMR Fourier Zeugmatography. *J Magn Reson*, 18:69–83, 1975.

[6] J. M. S. Hutchison and M. A. Foster. *Practical NMR imaging*, chapter 1: General Principles, pages 1–47. IRL Press limited, 1987.

[7] A. Faller and M. Schünke. *Der Körper des Menschen: Einführung in Bau und Funktion.* Thieme, 15te Auflage, 2008.

[8] E. Haacke, R. Brown, M. Thompson, and R. Venkatesan. *Magnetic resonance imaging: Physical principles and sequence design*, chapter 1: Magnetic Resonance Imaging: A Preview, pages 1–13. Wiley-Lis, 1999.

[9] E. Haacke, R. Brown, M. Thompson, and R. Venkatesan. *Magnetic resonance imaging: Physical principles and sequence design*, chapter 2: Classical Response of a single Nucleus to a Magnetic Field, pages 17–32. Wiley-Lis, 1999.

[10] E. Haacke, R. Brown, M. Thompson, and R. Venkatesan. *Magnetic resonance imaging: Physical principles and sequence design*, chapter 4: Magnetization, Relaxation and the Bloch Equation, pages 51–62. Wiley-Lis, 1999.

[11] R.B. Buxton. *Introduction to functional magnetic resonance imaging: principles and techniques*, chapter 10: Mapping the MR signal, pages 218–248. Cambridge Univ Pr, 2002.

[12] R.B. Buxton. *Introduction to functional magnetic resonance imaging: principles and techniques*, chapter 5: Magnetic Resonance Imaging, pages 86–103. Cambridge Univ Pr, 2002.

[13] M.A. Bernstein. *Handbook of MRI pulse sequences*, chapter 3: Basic radiofrequency pulse functions, pages 67–77. Elsevier Academic press, 2004.

[14] R.B. Buxton. *Introduction to functional magnetic resonance imaging: principles and techniques*, chapter 4: Nuclear magnetic resonance, pages 64–85. Cambridge Univ Pr, 2002.

[15] M.A. Bernstein. *Handbook of MRI pulse sequences*, chapter 14: Basic pulse sequences, pages 579–647. Elsevier Academic press, 2004.

[16] J. Hennig, A. Nauerth, and H. Friedburg. RARE imaging: a fast imaging method for clinical MR. *Magn Reson Med*, 3(6):823–833, 1986.

[17] X. J. Zhou. *Handbook of MRI pulse sequences*, chapter 16: Echo train pulse sequences, pages 774–801. Elsevier Academic press, 2004.

[18] R.B. Buxton. *Introduction to functional magnetic resonance imaging: principles and techniques*, chapter 16: The nature of the blood oxygenation level dependent effect, pages 390–416. Cambridge Univ Pr, 2002.

[19] P. C. Lauterbur, M.H. Mendonca-Dias, and A.M. Rudin. Augmentation of Tissue Water Proton Spin-Lattice Relaxation Rates by In Vivo Addition of Paramagnetic Ions. *Frontiers of Biological Energetics*, pages 752–759, 1978.

[20] V. M. Runge, J. A. Clanton, C. M. Lukehart, C. L. Partain, and A. E. James. Paramagnetic agents for contrast-enhanced NMR imaging: a review. *AJR Am J Roentgenol*, 141(6):1209–1215, 1983.

[21] D.H. Carr, J. Brown, A. W. Leung, and J. M. Pennock. Iron and gadolinium chelates as contrast agents in NMR imaging: preliminary studies. *J Comput Assist Tomogr*, 8(3):385–389, 1984.

[22] M. Mendonca-Dias, E. Gaggelli, and P. C. Lauterbur. Paramagnetic contrast agents in nuclear magnetic resonance medical imaging. *Semin Nucl Med*, 13(4):364–376, 1983.

[23] A. Volkov. Contrast agents in magnetic resonance imaging. *Term Paper*, 17:http://home.utah.edu/∼av6a51/mri.htm, 1997.

[24] N. Chou, J. Wu, J. Bai, and A. Qiu. Robust automatic rodent brain extraction using 3D Pulse-coupled Neural Networks (PCNN). *IEEE Trans Image Process*, 2011.

[25] K. Friston. *Human Brain function*, chapter Introduction: Experimemtal

design and statistical parametric mapping, pages 1–67. Academic Press, London, 2004.

[26] M. Brett, W. Penny, and S. Kiebel. *Human brain function*, chapter 44: An introduction to random field theory, pages 867–879. Academic Press, 2004.

[27] K. J. Friston, A. P. Holmes, K. J. Worsley, J.-P. Poline, and R. S. J. Frith, C. D. abd Frackowiak. Statistical parametric mapping in functional imaging: a general linear approach. *Human brain mapping*, 2:189–210, 1995.

[28] K. Worsley. *Human brain function*, chapter 45: Developments in random field theory, pages 881–886. Academic Press, 2004.

[29] R.E. Connick and R.E. Poulson. Effect of paramagnetic ions on the nuclear magnetic resonance of O^{17} in water and the rate of elimination of water molecules from the first coordination sphere of cations. *J Chem Phys*, 30(3):759–761, 1959.

[30] J. L. Aschner and M. Aschner. Nutritional aspects of manganese homeostasis. *Mol Aspects Med*, 26(4-5):353–362, 2005.

[31] D. Rucker, R. Thadhani, and M. Tonelli. Trace element status in hemodialysis patients. *Semin Dial*, 23(4):389–395, 2010.

[32] J. Jankovic. Searching for a relationship between manganese and welding and Parkinson's disease. *Neurology*, 64(12):2021–2028, 2005.

[33] Agency for toxic substances and disease registry (ATSDR). Toxicological profile for manganese (Draft for public comment). Technical report, U.S. Department of Health and Human Services, Public Health Service., 2008.

[34] D.G. Barceloux. Manganese. *J Toxicol Clin Toxicol*, 37(2):293–307, 1999.

[35] H. A. Schroeder, J. J. Balassa, and I. H. Tipton. Essential trace metals in man: manganese. A study in homeostasis. *J Chronic Dis*, 19(5):545–571, 1966.

[36] A. W. Dobson, K. Erikson, and M. Aschner. Manganese neurotoxicity. *Ann N Y Acad Sci*, 1012:115–128, 2004.

[37] F.H. Nielsen. *Modern nutrition in health and disease*, chapter 16: Ultratrace Minerals, pages 283–303. Baltimore: Williams & Wilkins, 1999.

[38] K. Green, M.D. Brand, and M.P. Murphy. Prevention of mitochondrial oxidative damage as a therapeutic strategy in diabetes. *Diabetes*, 53:110–118, 2004.

[39] A.A. Brock, S.A. Chapman, E.A. Ulman, and G. Wu. Dietary manganese deficiency decreases rat hepatic arginase activity. *J Nutr*, 124:340–344, 1994.

[40] M. Aschner, K. Erikson, and D. C. Dorman. Manganese dosimetry: species differences and implications for neurotoxicity. *Crit Rev Toxicol*, 35(1):1–32, 2005.

[41] F. C. Wedler. Biological significance of manganese in mammalian systems. *Prog Med Chem*, 30:89–133, 1993.

[42] J. R. Prohaska. Functions of trace elements in brain metabolism. *Physiol Rev*, 67(3):858–901, 1987.

[43] A. St-Pierre, L. Normandin, G. Carrier, G. Kennedy, R. Butterworth, and J. Zayed. Bioaccumulation and locomotor effect of manganese dust in rats. *Inhal Toxicol*, 13(7):623–632, 2001.

[44] W. D. Gallup and L. C. Norris. The essentialness of manganese for the normal development of bone. *Science*, 87(2245):18–19, 1938.

[45] G. Frost, C.W. Asling, and M.M. Nelson. Skeletal deformities in manganese-deficient rats. *Anat Rec*, 134:37–53, 1959.

[46] L. G. Strause, J. Hegenauer, P. Saltman, R. Cone, and D. Resnick. Effects of long-term dietary manganese and copper deficiency on rat skeleton. *J Nutr*, 116(1):135–141, 1986.

[47] I. Tenaud, I. Sainte-Marie, O. Jumbou, P. Litoux, and B. Dréno. In vitro modulation of keratinocyte wound healing integrins by zinc, copper and manganese. *Br J Dermatol*, 140(1):26–34, 1999.

[48] G.J. Everson, L.S. Hurley, and J.F. Geiger. Manganese deficiency in the guinea pig. *J Nutr*, 68(1):49–56, 1959.

[49] A.R. Kemmerer, C.A. Elvehjem, and E.B. Hart. Studies on the relation of manganese to the nutrition of the mouse. *J Biol Chem*, 92:623, 1931.

[50] E.R. Orent and E.V. McCollum. Effects of deprivation of manganese in the rat. *J Biol Chem*, 92:651, 1931.

[51] G. Saner, T. Daolu, and T. Ozden. Hair manganese concentrations in newborns and their mothers. *Am J Clin Nutr*, 41(5):1042–1044, 1985.

[52] J. H. Freeland-Graves, C. W. Bales, and B. Fares. *Nutritional bioavailability of manganese*, chapter 10: Manganese requirements of humans, pages 90–104. American Chemical Society, 1987.

[53] B. J. Friedman, J. H. Freeland-Graves, C. W. Bales, F. Behmardi, R. L. Shorey-Kutschke, R. A. Willis, J. B. Crosby, P. C. Trickett, and S. D.

Houston. Manganese balance and clinical observations in young men fed a manganese-deficient diet. *J Nutr*, 117(1):133–143, 1987.

[54] J. G. Penland and P. E. Johnson. Dietary calcium and manganese effects on menstrual cycle symptoms. *Am J Obstet Gynecol*, 168(5):1417–1423, 1993.

[55] L. W. Oberley and G. R. Buettner. Role of superoxide dismutase in cancer: a review. *Cancer Res*, 39(4):1141–1149, 1979.

[56] A. Takeda. Manganese action in brain function. *Brain Res Brain Res Rev*, 41(1):79–87, 2003.

[57] J. Couper. On the effects of black oxide of managanese when inhaled into the lungs. *Br Ann Med Pharmacol*, 1:41–42, 1837.

[58] G.C Cotzias. Levodopa, manganese, and degenerations of the brain. *Harvey Lect*, 68:115–147, 1974.

[59] G.C. Cotzias, K. Horiuchi, S. Fuenzalida, and I. Mena. Chronic manganese poisoning. Clearance of tissue manganese concentrations with persistance of the neurological picture. *Neurology*, 18(4):376–382, 1968.

[60] I. Mena, O. Marin, S. Fuenzalida, and G. C. Cotzias. Chronic manganese poisoning. Clinical picture and manganese turnover. *Neurology*, 17(2):128–136, 1967.

[61] I. Mena, K. Horiuchi, K. Burke, and G. C. Cotzias. Chronic manganese poisoning. Individual susceptibility and absorption of iron. *Neurology*, 19(10):1000–1006, 1969.

[62] C. C. Huang. Parkinsonism induced by chronic manganese intoxication–an experience in Taiwan. *Chang Gung Med J*, 30(5):385–395, 2007.

[63] M. Yamada, S. Ohno, R. Okayasu, I. amd Okeda, S. Hatakeyama, H. Watanabe, K. Ushio, and H. Tsukagoshi. Chronic manganese poisoning: a neuropathological study with determination of manganese distribution in the brain. *Acta Neuropathol*, 70(3-4):273–278, 1986.

[64] H. Eriksson, J. Tedroff, K. A. Thuomas, S. M. Aquilonius, P. Hartvig, K. J. Fasth, P. Bjurling, K. G. Långström, B.and Hedström, and E. Heilbronn. Manganese induced brain lesions in Macaca fascicularis as revealed by positron emission tomography and magnetic resonance imaging. *Arch Toxicol*, 66(6):403–407, 1992.

[65] K. Erikson, C. John, S. Jones, and M. Aschner. Manganese accumulation in striatum of mice exposed to toxic doses is dependent upon a functional dopamine transporter. *Environ Toxicol Phar*, 20:390–394, 2005.

[66] H. Shinotoh, B. J. Snow, N. S. Chu, C. C. Huang, C. S. Lu, H. Lee, C. abd Takahashi, and D. B. Calne. Presynaptic and postsynaptic striatal dopaminergic function in patients with manganese intoxication: a positron emission tomography study. *Neurology*, 48(4):1053–1056, 1997.

[67] L. Normandin and A. S. Hazell. Manganese neurotoxicity: an update of pathophysiologic mechanisms. *Metab Brain Dis*, 17(4):375–387, 2002.

[68] C. E. Gavin, K. K. Gunter, and T. E. Gunter. Manganese and calcium transport in mitochondria: implications for manganese toxicity. *Neurotoxicology*, 20(2-3):445–453, 1999.

[69] A. S. Hazell. Astrocytes and manganese neurotoxicity. *Neurochem Int*, 41(4):271–277, 2002.

[70] J. A. Roth. Are there common biochemical and molecular mecha-

nisms controlling manganism and parkisonism. *Neuromolecular Med*, 11(4):281–296, 2009.

[71] K. Eriksson, A. W. Dobson, D. C. Dorman, and M. Aschner. Manganese exposure and induced oxidative stress in the rat brain. *Sci Total Environ*, 334-335:409–416, 2004.

[72] W. N. Sloot and J. B. Gramsbergen. Axonal transport of manganese and its relevance to selective neurotoxicity in the rat basal ganglia. *Brain Res*, 657(1-2):124–132, 1994.

[73] M. Morello, P. Zatta, P. Zambenedetti, A. Martorana, V. D'Angelo, G. Melchiorri, G. Bernardi, and G. Sancesario. Manganese intoxication decreases the expression of manganoproteins in the rat basal ganglia: an immunohistochemical study. *Brain Res Bull*, 74(6):406–415, 2007.

[74] W. Zheng, Q. Zhao, V. Slavkovich, M. Aschner, and J. H. Graziano. Alteration of iron homeostasis following chronic exposure to manganese in rats. *Brain Res*, 833(1):125–132, 1999.

[75] G. Cohen and R. E. Heikkila. The generation of hydrogen peroxide, superoxide radical, and hydroxyl radical by 6-hydroxydopamine, dialuric acid, and related cytotoxic agents. *J Biol Chem*, 249(8):2447–2452, 1974.

[76] F. S. Archibald and C. Tyree. Manganese poisoning and the attack of trivalent manganese upon catecholamines. *Arch Biochem Biophys*, 256(2):638–650, 1987.

[77] C. D. Garner and J. P. Nachtman. Manganese catalyzed auto-oxidation of dopamine to 6-hydroxydopamine in vitro. *Chem Biol Interact*, 69(4):345–351, 1989.

[78] V. Fitsanakis, C. Au, H. Erikson, and M. Aschner. The effects of manganese on glutamate, dopamine and γ-aminobutyric acid regulation. *Neurochemistry International*, 48:426–433, 2006.

[79] E. Bonilla. Increased GABA content in caudate nucleus of rats after chronic manganese chloride administration. *J Neurochem*, 31(2):551–552, 1978.

[80] P. K. Seth, J. S. Hong, C. D. Kilts, and S. C. Bondy. Alteration of cerebral neurotransmitter receptor function by exposure of rats to manganese. *Toxicol Lett*, 9(3):247–254, 1981.

[81] G. W. Lipe, H. Duhart, G. D. Newport, W. Slikker, and S. F. Ali. Effect of manganese on the concentration of amino acids in different regions of the rat brain. *J Environ Sci Health B*, 34(1):119–132, 1999.

[82] S. V. Chandra, K. M. Malhotra, and G. S. Shukla. GABAergic neurochemistry in manganese exposed rats. *Acta Pharmacol Toxicol (Copenh)*, 51(5):456–458, 1982.

[83] A. P. Pautler, R. G.and Koretsky. Tracing odor-induced activation in the olfactory bulbs of mice using manganese-enhanced magnetic resonance imaging. *Neuroimage*, 16(2):441–448, 2002.

[84] H. Tjälve, C. Mejàre, and K. Borg-Neczak. Uptake and transport of manganese in primary and secondary olfactory neurones in pike. *Pharmacol Toxicol*, 77(1):23–31, 1995.

[85] J. Tjälve, H. adn Henriksson, J. Tallkvist, B. S. Larsson, and N. G. Lindquist. Uptake of manganese and cadmium from the nasal mucosa into the central nervous system via olfactory pathways in rats. *Pharmacol Toxicol*, 79(6):347–356, 1996.

[86] F. Zhiqiang, Z. Peng, H. Fanheng, L. Peng, Z. Run, X. Ruxiang, W. Zhibo, and J. Xiaodan. Activity-induced manganese-dependent functional MRI of the rat visual cortex following intranasal manganese chloride administration. *Neuroscience Letters*, 481:110–114, 2010.

[87] I. Wilhelm, C. Fazakas, and I. A. Krizbai. In vitro models of the blood-brain barrier. *Acta Neurobiol Exp (Wars)*, 71(1):113–128, 2011.

[88] J. Laterra and G.W. Goldstein. *Principles of neural science*, chapter Appendix B, pages 1288–1301. Elsevier New York, 1991.

[89] O. Rabin, L. Hegedus, J. M. Bourre, and Q. R. Smith. Rapid brain uptake of manganese(II) across the blood-brain barrier. *J Neurochem*, 61(2):509–517, 1993.

[90] M. Aschner and M. Gannon. Manganese (Mn) transport across the rat blood-brain barrier: saturable and transferrin-dependent transport mechanisms. *Brain Res Bull*, 33(3):345–349, 1994.

[91] J. Crossgrove, D. D. Allen, B. L. Bukaveckas, S. S. Rhineheimer, and R. A. Yokel. Manganese distribution across the blood-brain barrier. I. Evidence for carrier-mediated influx of managanese citrate as well as manganese and manganese transferrin. *Neurotoxicology*, 24(1):3–13, 2003.

[92] M. Aschner. Manganese homeostasis in the CNS. *Environ Res*, 80:105–109, 1999.

[93] M. Knöpfel, G. Schulthess, F. Funk, and H. Hauser. Characterization of an integral protein of the brush border membrane mediating the transport of divalent metal ions. *Biophys J*, 79(2):874–884, 2000.

[94] V. Picard, G. Govoni, N. Jabado, and P. Gros. Nramp 2 (DCT1/DMT1) expressed at the plasma membrane transports iron and other divalent cations into a calcein-accessible cytoplasmic pool. *J Biol Chem*, 275(46):35738–35745, 2000.

[95] N. A. Bock, F. F. Paiva, G. C. Nascimento, J. D. Newman, and A.C. Silva. Cerebrospinal fluid to brain transport of manganese in a non-human primate revealed by MRI. *Brain Res*, 1198:160–170, 2008.

[96] C. Schmitt, N. Strazielle, P. Richaud, A. Bouron, and J.-F. Ghersi-Egea. Active transport at the blood-CSF barrier contributes to manganese influx into the brain. *J Neurochem*, 117(4):747–756, 2011.

[97] I. Aoki, Y.-J. Lin Wu, A.C. Silva, C. M. Lynch, and A.P. Koretsky. In vivo detection of neuroarchitecture in the rodent brain using manganese-enhanced MRI. *Neuroimage*, 22(3):1046–1059, 2004.

[98] J. H. Lee, A. C. Silva, H. Merkle, and A. P. Koretsky. Manganese-enhanced magnetic resonance imaging of mouse brain after systemic administration of MnCl2: dose-dependent and temporal evolution of T1 contrast. *Magn Reson Med*, 53(3):640–648, 2005.

[99] V.A. Murphy, K.C. Wadhwani, Q. R. Smith, and S.I. Rapoport. Saturable transport of managanese (II) across the rat blood brain barrier. *J Neurochem*, 57:948–954, 1991.

[100] P. Drapeau and D. A. Nachshen. Manganese fluxes and manganese-dependent neurotransmitter release in presynaptic nerve endings isolated from rat brain. *J Physiol*, 348:493–510, 1984.

[101] P. B. Simpson, R. A. Challiss, and S. R. Nahorski. Divalent cation entry

in cultured rat cerebellar granule cells measured using Mn^{2+} quench of fura 2 fluorescence. *Eur J Neurosci*, 7(5):831–840, 1995.

[102] R. G. Pautler. In vivo, trans-synaptic tract-tracing utilizing manganese-enhanced magnetic resonance imaging (MEMRI). *NMR Biomed*, 17(8):595–601, 2004.

[103] K. Narita, F. Kawasaki, and H. Kita. Mn and Mg influxes through Ca channels of motor nerve terminals are prevented by verapimil in frogs. *Brain Res*, 510:289–295, 1990.

[104] T. C. Hu, R. G. Pautler, G. A. MacGowan, and A. P. Koretsky. Manganese-enhanced MRI of mouse heart during changes in inotropy. *Magn Reson Med*, 46(5):884–890, 2001.

[105] R. G. Pautler, R. Mongeau, and R. E. Jacob. In vivo trans-synaptic tract tracing from the murine striatum and amygdala utilizing manganese enhanced MRI (MEMRI). *Magn Reson Med*, 50(1):33–39, 2003.

[106] R. G. Pautler, A. C. Silva, and A. P. Koretsky. In vivo neuronal tract tracing using manganese-enhanced magnetic resonance imaging. *Magn Reson Med*, 40(5):740–748, 1998.

[107] R. G. Pautler and S. E. Fraser. The year(s) of the contrast agent - micro-MRI in the new millennium. *Curr Opin Immunol*, 15(4):385–392, 2003.

[108] R. A. Yokel. Manganese flux across the Blood-Brain barrier. *Neuromolecular Med*, 11:297–310, 2009.

[109] A. Takeda, J. Sawashita, and S. Okada. Biological half-lives of zinc and manganese in rat brain. *Brain Res*, 695(1):53–58, 1995.

[110] F.C. Wedler, B.W. Ley, and A.A. Grippo. Manganese(II) dynamics and distribution in glial cells cultured from chick cerebral cortex. *Neurochem Res*, 14:1129–1135, 1989.

[111] R.E. London, G. Toney, S.A. Gabel, and A. Funk. Magnetic resonance imaging studies of the brains of anesthetized rats treated with manganese chloride. *Brain Research Bulletin*, 23:229–235, 1989.

[112] T. Watanabe, O. Natt, S. Boretius, J. Frahm, and T. Michaelis. In vivo 3D MRI staining of mouse brain after subcutaneous application of $MnCl_2$. *Magn Reson Med*, 48(5):852–859, 2002.

[113] Y. J. Lin and A. P. Koretsky. Manganese ion enhances T1-weighted MRI during brain activation: an approach to direct imaging of brain function. *Magn Reson Med*, 38(3):378–388, 1997.

[114] C. A. Massaad and R. G. Pautler. Manganese-enhanced magnetic resonance imaging (MEMRI). *Methods Mol Biol*, 711:145–174, 2011.

[115] T. Watanabe, J. Frahm, and T. Michaelis. Mapping of retinal projections in the living rat using high-resolution 3D gradient-echo MRI with Mn^{2+}-induced contrast. *Magn Reson Med*, 46(3):424–429, 2001.

[116] J.-W. Lee, J.-A. Park, J.-J. Lee, S.-J. Bae, S.-H. Lee, J.-C. Jung, M.-N. Kim, J. Lee, S. Woo, and Y. Chang. Manganese-enhanced auditory tract-tracing MRI with cochlear injection. *Magn Reson Imaging*, 25(5):652–656, 2007.

[117] A. V. D. Van der Linden, V. V. Van Meir, I. Tindemans, M. Verhoye, and J. Balthazart. Applications of manganese-enhanced magnetic resonance imaging (MEMRI) to image brain plasticity in song birds. *NMR Biomed*, 17(8):602–612, 2004.

[118] A. V. D. Van der Linden, M. Verhoye, V. V. Van Meir, I. Tindemans, M. Eens, P. Absil, and J. Balthazart. In vivo manganese-enhanced magnetic resonance imaging reveals connections and functional properties of the songbird vocal control system. *Neuroscience*, 112(2):467–474, 2002.

[119] I. Tindemans, M. Verhoye, J. Balthazart, and A. V. D. Van Der Linden. In vivo dynamic ME-MRI reveals differential functional responses of RA- and area X-projecting neurons in the HVC of canaries exposed to conspecific song. *Eur J Neurosci*, 18(12):3352–3360, 2003.

[120] Y. Golub, S. F. Kaltwasser, C. P. Mauch, L. Herrmann, U. Schmidt, F. Holsboer, M. Czisch, and C. T. Wotjak. Reduced hippocampus volume in the mouse model of Posttraumatic Stress Disorder. *J Psychiatr Res*, 45(5):650–659, 2011.

[121] A. Haapanen, U. A. Ramadan, T. Autti, R. Joensuu, and J. Tyynelä. In vivo MRI reveals the dynamics of pathological changes in the brains of cathepsin D-deficient mice and correlates changes in manganese-enhanced MRI with microglial activation. *Magn Reson Imaging*, 25(7):1024–1031, 2007.

[122] E. C. Henning, X. Meng, M. Fisher, and C. H. Sotak. Visualization of cortical spreading depression using manganese-enhanced magnetic resonance imaging. *Magn Reson Med*, 53(4):851–857, 2005.

[123] B. Grünecker, S. F. Kaltwasser, Y. Peterse, P. G. Sämann, M. V. Schmidt, C. T. Wotjak, and M. Czisch. Fractionated manganese injections: effects on MRI contrast enhancement and physiological measures in C57BL/6 mice. *NMR Biomed*, 23(8):913–921, 2010.

[124] I. J. Yu, J. Zou, J. S. Babb, G. Johnson, D. H. Sanes, and D. H. Turn-

bull. Statistical mapping of sound-evoked activity in the mouse auditory midbrain using Mn-enhanced MRI. *Neuroimage*, 39(1):223–230, 2008.

[125] J.-C. Weng, J.-H. Chen, P.-F. Yang, and W.-Y. I. Tseng. Functional mapping of rat barrel activation following whisker stimulation using activity-induced manganese-dependent contrast. *Neuroimage*, 36(4):1179–1188, 2007.

[126] P.-W. So, W.-S. Yu, Y.-T. Kuo, C. Wasserfall, G. Goldstein, J. D. Bell, and G. Frost. Impact of resistant starch on body fat patterning and central appetite regulation. *PLoS One*, 2(12):e1309, 2007.

[127] N. Singewald. Altered brain activity processing in high-anxiety rodents revealed by challenge paradigms and functional mapping. *Neurosci Biobehav Rev*, 31(1):18–40, 2007.

[128] M. J. Millan. The neurobiology and control of anxious states. *Prog Neurobiol*, 70(2):83–244, 2003.

[129] P. Muigg, S. Schreiber, P. Salchner, M. Bunck, R. Landgraf, and N. Singewald. Differential stress-induced neuronal activation patterns in mouse lines selectively bred for high, normal or low anxiety. *PLoS One*, 4(4):e5346, 2009.

[130] C. Belzung and P. Philippot. Anxiety from a phylogenetic persepective: Is there a qualitative difference between human and animal anxiety? *Neural Plasticity*, 2007, 2007.

[131] R.C. Kessler, M. Angermeyer, J.C. Anthony, R. de Graaf, K. Demyttenaere, I. Gasquet, G. de Girolamo, S. Gluzman, O. Gureje, J.M. Haro, N. Kawakami, A. Karam, D. Levinson, M.E.M. Mora, M.A.O. Browne, J. Posada-Villa, D.J. Stein, C.H.A. Tsang, S. Aguilar-Gaxiola,

J. Alonso, S. Lee, S. Heeringa, B.-E. Pennell, P. Berglund, M.J. Gruber, M. Petukhova, S. Chatterji, and T.B. on behalfof THE WHO WORLD MENTAL HEALTH SURVEY CONSORTIUM Üstün. Lifetime prevalence and age-of-onset distributions of mental disorders in the World Health Organization's World Mental Health Survey Initiative. *World Psychiatry*, 6:168–176, 2007.

[132] American Psychiatric Association, Washington D.C. *Diagnostic and statistical manual of mental disorders*, 4 edition, 1994.

[133] World Health Organization, Geneva. *International Statistical Classification of Diseases and Health Related Problems*, 2004.

[134] U.S. department of health and National Institutes of health human services. Anxiety disorders.

[135] D.C. Blanchard, G. Griebel, and R.J. Blanchard. Mouse defensive behaviors: pharmacological and behavioral assays for anxiety and panic. *Neuroscience & Biobehavioral Reviews*, 25:205–218, 2001.

[136] C. T. Wotjak. *Angststörungen-Klinik, Forschung, Therapie*, chapter Angst und Furcht im Tiermodell. Rupprecht, R. and Kellner M., 2011 in press.

[137] R. Landgraf, M. S. Kessler, M. Bunck, C. Murgatroyd, D. Spengler, M. Zimbelmann, M. Nussbaumer, L. Czibere, C. W. Turck, N. Singewald, D. Rujescu, and E. Frank. Candidate genes of anxiety-related behavior in HAB/LAB rats and mice: focus on vasopressin and glyoxalase-I. *Neurosci Biobehav Rev*, 31(1):89–102, 2007.

[138] R. Landgraf and A. Wigger. High vs low anxiety-related behavior rats:

an animal model of extremes in trait anxiety. *Behavior Genetics*, 32:301–314, 2002.

[139] G. Liebsch, A. Montkowski, F. Holsboer, and R. Landgraf. Behavioral profiles of two Wistar rat lines selectively bred for high or low anxiety-related behavior. *Behav Brain Res*, 94:301–310, 1998.

[140] L. Czibere. *Assessing the complex nature of behavior: Sequence-based and transcriptomic analyses in a mouse model of extremes in trait anxiety*. PhD thesis, Ludwig-Maximilians-Universität, Munich, 2008.

[141] S. A. Krömer, M. S. Kessler, D. Milfay, I. N. Birg, M. Bunck, L. Czibere, M. Panhuysen, B. Pütz, J. M. Deussing, F. Holsboer, R. Landgraf, and C. W. Turck. Identification of glyoxalase-I as a protein marker in a mouse model of extremes in trait anxiety. *J Neurosci*, 25(17):4375–4384, 2005.

[142] M. S. Kessler, C. Murgatroyd, M. Bunck, L. Czibere, E. Frank, W. Jacob, C. Horvath, P. Muigg, F. Holsboer, N. Singewald, D. Spengler, and R. Landgraf. Diabetes insipidus and, partially, low anxiety-related behaviour are linked to a SNP-associated vasopressin deficit in LAB mice. *Eur J Neurosci*, 26(10):2857–2864, 2007.

[143] P. Salchner, S. B. Sartori, C. Sinner, A. Wigger, E. Frank, R. Landgraf, and N. Singewald. Airjet and FG-7142-induced Fos expression differs in rats selectively bred for high and low anxiety-related behavior. *Neuropharmacology*, 50(8):1048–1058, 2006.

[144] A. Erhardt, L. Czibere, D. Roeske, S. Lucae, P. G. Unschuld, S. Ripke, M. Specht, M. A. Kohli, S. Kloiber, M. Ising, A. Heck, H. Pfister, P. Zimmermann, R. Lieb, B. Pütz, M. Uhr, P. Weber, J. M. Deussing, M. Gonik, M. Bunck, M. S. Keßler, E. Frank, C. Hohoff, K. Domschke, P. Krakowitzky, W. Maier, B. Bandelow, C. Jacob, J. Deckert,

J. Schreiber, S. amd Strohmaier, M. Nöthen, S. Cichon, M. Rietschel, T. Bettecken, M. E. Keck, R. Landgraf, B. Müller-Myhsok, F. Holsboer, and E. B. Binder. TMEM132D, a new candidate for anxiety phenotypes: evidence from human and mouse studies. *Mol Psychiatry*, 2010.

[145] R. Landgraf, A. Wigger, F. Holsboer, and I.D. Neumann. Hyper-reactive hypothalamo-pituitary-adrenocortical axis in rats bred for high anxiety-related behaviour. *J Neuroendocrinol*, 11:405–407, 1999.

[146] K. M. Lahti, C. F. Ferris, F. Li, C. H. Sotak, and J. A. King. Imaging brain activity in conscious animals using functional MRI. *J Neurosci Methods*, 82(1):75–83, 1998.

[147] R. N. S. Sachdev, G. C. Champney, R. R. Lee, H. abd Price, D. R. Pickens, V. L. Morgan, J. D. Stefansic, P. Melzer, and F. F. Ebner. Experimental model for functional magnetic resonance imaging of somatic sensory cortex in the unanesthetized rat. *Neuroimage*, 19(3):742–750, 2003.

[148] N. Salomé, P. Salchner, O. Viltart, H. Sequeira, A. Wigger, R. Landgraf, and N. Singewald. Neurobiological correlates of high (HAB) versus low anxiety-related behavior (LAB): differential Fos expression in HAB and LAB rats. *Biol Psychiatry*, 55(7):715–723, 2004.

[149] E. Frank, P. Salchner, J. M. Aldag, N. Salomé, N. Singewald, R. Landgraf, and A. Wigger. Genetic predisposition to anxiety-related behavior determines coping style, neuroendocrine responses, and neuronal activation during social defeat. *Behav Neurosci*, 120(1):60–71, 2006.

[150] M. H. Emmert and J. P. Herman. Differential forebrain c-fos mRNA induction by ether inhalation and novelty: evidence for distinctive stress pathways. *Brain Res*, 845(1):60–67, 1999.

[151] M. Kabbaj and H. Akil. Individual differences in novelty-seeking behavior in rats: a c-fos study. *Neuroscience*, 106(3):535–545, 2001.

[152] Mulders and Chan. Heat capacity measurements of 3He-4He mixtures in aerogel. *Phys Rev Lett*, 75(20):3705–3708, 1995.

[153] M. T. Wong-Riley. Cytochrome oxidase: an endogenous metabolic marker for neuronal activity. *Trends Neurosci*, 12(3):94–101, 1989.

[154] M. T. Wong-Riley, M. M. Merzenich, and P. A. Leake. Changes in endogenous enzymatic reactivity to DAB induced by neuronal inactivity. *Brain Res*, 141(1):185–192, 1978.

[155] M. Wong-Riley. Changes in the visual system of monocularly sutured or enucleated cats demonstrable with cytochrome oxidase histochemistry. *Brain Res*, 171(1):11–28, 1979.

[156] D. R. Riddle and M. E. Forbes. Regulation of cytochrome oxidase activity in the rat forebrain throughout adulthood. *Neurobiol Aging*, 26(7):1035–1050, 2005.

[157] A. Poremba, D. Jones, and F. Gonzalez-Lima. Classical conditioning modifies cytochrome oxidase activity in the auditory system. *Eur J Neurosci*, 10(10):3035–3043, 1998.

[158] N. A. Bock, A. Kocharyan, and A.C. Silva. Manganese-enhanced MRI visualizes V1 in the non-human primate visual cortex. *NMR Biomed*, 22(7):730–736, 2009.

[159] D. C. Dorman, M. F. Struve, C. U. Marshall, M.W. abd Parkinson, R.A. James, and B. A. Wong. Tissue manganese concentrations in young male rhesus monkeys following subchronic manganese sulfate inhalation. *Toxicol Sci*, 92(1):201–210, 2006.

[160] Y.-T. Kuo, A. H. Herlihy, P.-W. So, K. K. Bhakoo, K. Kishore, and J. D. Bell. In vivo measurements of T1 relaxation times in mouse brain associated with different mode of systemic administration of manganese chloride. *J Magn Reson Imaging*, 21:334–339, 2005.

[161] K. Franklin and G. Paxinos. The mouse brain in stereotaxic coordinates. *San Diego: Academic Press, Inc.*, 1997.

[162] F. F. Bock, N. A. Paiva and A.C. Silva. Fractionated manganese-enhanced MRI. *NMR Biomed*, 21(5):473–478, 2008.

[163] K. Chuang, A.C. Lee, J.H. abd Silva, L. Belluscio, and A.P. Koretsky. Manganese enhanced MRI reveals functional circuitry in response to odorant stimuli. *Neuroimage*, 44(2):363–372, 2009.

[164] K. Chuang, L. Belluscio, and A.P. Koretsky. In vivo detection of individual glomeruli in the rodent olfactory bulb using manganese enhanced MRI. *Neuroimage*, 49(2):1350–1356, 2010.

[165] A. C. Silva, J. H. Lee, C. W.-H. Wu, J. Tucciarone, G. Pelled, I. Aoki, and A. P. Koretsky. Detection of cortical laminar architecture using manganese-enhanced MRI. *J Neurosci Methods*, 167(2):246–257, 2008.

[166] T. Watanabe, J. Radulovic, J. Spiess, O. Natt, S. Boretius, J. Frahm, and T. Michaelis. In vivo 3D MRI staining of the mouse hippocampal system using intracerebral injection of $MnCl_2$. *NeuroImage*, 22:860–867, 2004.

[167] I. Cohen and R. Miles. Contributions of intrinsic and synaptic activities to the generation of neuronal discharges in in vitro hippocampus. *J Physiol*, 524:485–502, 2000.

[168] R.E. Fisher, R. Gray, and D. Johnston. Properties and distribution of single voltage-gated calcium channels in adult hippocampal neurons. *J Neurophys*, 64:91–104, 1990.

[169] S. J. Jackson, R. Hussey, M. A. Jansen, G. D. Merrifield, I. Marshall, Alasdair MacLullich, J. L. W. Yau, and T. Bast. Manganese-enhanced magnetic resonance imaging (MEMRI) of rat brain after systemic administration of $MnCl_2$: hippocampal signal enhancement without disruption of hippocampus-dependent behavior. *Behav Brain Res*, 216(1):293–300, 2011.

[170] O. Eschenko, S. Canals, I. Simanova, M. Beyerlein, Y. Murayama, and N. K. Logothetis. Mapping of functional brain activity in freely behaving rats during voluntary running using manganese enhanced MRI: Implication for longitudinal studies. *NeuroImage*, 49:2544–2555, 2010.

[171] S. F. Kaltwasser. *Volumetric manganese enhanced magnetic resonance imaging in mice*. PhD thesis, Ludwig-Maximilians-Universitaet, 2011.

[172] C. H. Kern, G. D. Stanwood, and D. R. Smith. Preweaning manganese exposure causes hyperactivity, disinhibition, and spatial learning and memory deficits associated with altered dopamine receptor and transporter levels. *Synapse*, 64(5):363–378, 2010.

[173] O. Eschenko, S. Canals, I. Simanova, and N. Logothetis. Behavioral, electrophysiological and histopathological consequences of systemic manganese administration in MEMRI. *Magn Reson Imaging*, 28(8):1165–1174, 2010.

[174] F. Gonzalez-Lima and A. Cada. Cytochrome oxidase activity in the auditory system of the mouse: A qualitative and quantitative histochemical study. *Neuroscience*, 63:559–578, 1994.

[175] W. M. Verhoeven, J. I. Egger, and H. J. Kuijpers. Manganese and acute paranoid psychosis: a case report. *J Med Case Reports*, 5:146, 2011.

[176] G. P. Layrargues, D. Shapcott, L. Spahr, and R. Butterworth. Accumulation of manganese and copper in pallidum of cirrhotic patients: role in the pathogenesis of hepatic encephalopathy? *Metab Brain Dis*, 10(4):353–356, 1995.

[177] S. Ikeda, Y. Yamaguchi, Y. Sera, H. Ohshiro, S. Uchino, Y. Yamashita, and M. Ogawa. Manganese deposition in the globus pallidus in patients with biliary atresia. *Transplantation*, 69(11):2339–2343, 2000.

[178] J. E. LeDoux. Emotion, memory and the brain. *Sci Am*, 270(6):50–57, 1994.

[179] J. H. Han, Y. H. Chung, J. D. Park, Y. K. Choong, S. O. Yang, H. S. Khang, H. K. Cheong, J. S. Lee, C. S. Ha, C. W. Song, I. H. Kwon, J. H. Sung, J. D. Heo, N.-Y. Kim, M. Huang, M. H. Cho, and I. J. Yu. Recovery from welding-fume-exposure-induced MRI T1 signal intensities after cessation of welding-fume exposure in brains of cynomolgus monkeys. *Inhal Toxicol*, 20(12):1075–1083, 2008.

[180] O. Y. Galvis-Alonso, A. M B Garcia, M. J. Orejarena, M. R. Lamprea, S. Botelho, C. A. Conde, S. Morato, and N. Garcia-Cairasco. A combined study of behavior and Fos expression in limbic structures after re-testing Wistar rats in the elevated plus-maze. *Brain Res Bull*, 81(6):595–599, 2010.

[181] G. E. Duncan, D. J. Knapp, and G. R. Breese. Neuroanatomical characterization of Fos induction in rat behavioral models of anxiety. *Brain Res*, 713(1-2):79–91, 1996.

[182] J. Menard and D. Treit. Lateral and medial septal lesions reduce anxiety in the plus-maze and probe-burying tests. *Physiol Behav*, 60(3):845–853, 1996.

[183] M. S. Fanselow and H.-W. Dong. Are the dorsal and ventral hippocampus functionally distinct structures? *Neuron*, 65(1):7–19, Jan 2010.

[184] A. N. Talalaenko, G. K. Krivobok, N. P. Bulgakova, and D. V. Pankrat'ev. Functional roles of the monoaminergic and aminoacidergic mechanisms of the dorsal pallidum in anxiety of different aversive origins. *Neurosci Behav Physiol*, 38(2):115–118, 2008.

[185] D. L. Walker, D. J. Toufexis, and M. Davis. Role of the bed nucleus of the stria terminalis versus the amygdala in fear, stress, and anxiety. *Eur J Pharmacol*, 463(1-3):199–216, 2003.

[186] M. Davis. *Neuropsychopharmacology: The Fifth Generation of Progress*, chapter 64, pages 931–951. Lippincott Williams and Wilkins Philadelphia, 2002.

[187] M.L. Brandão, J.M. Zanoveli, R.C. Ruiz-Martinez, L.C. Oliveira, and J. Landeira-Fernandez. Different patterns of freezing behavior organized in the periaqueductal gray of rats: association with different types of anxiety. *Behav Brain Res*, 188(1):1–13, 2008.

[188] M. L. Brandão, N.C. Coimbra, and P.C. Leao Borges. Effects of morphine and midazolam on reactivity to peripheral noxious and central aversive stimuli. *Neurosci Biobehav Rev*, 14:495–499, 1990.

[189] K.G. Borelli, M.J. Nobre, M. L. Brandão, and N. Coimbra. Effects of acute and chronic fluoxetine and diazepam on freezing behavior induced by electrical stuimulation of dorsolateral and lateral columns of

the periaqueductal gray matter. *Pharmacol, Biochem and Behavior*, 77:557–566, 2004.

[190] A. C. Troncoso, G. Cirilo-Júnior, G. Sandner, and M. L. Brandão. Signaled two-way avoidance learning using electrical stimulation of the inferior colliculus as negative reinforcement: effects of visual and auditory cues as warning stimuli. *Braz J Med Biol Res*, 31:391–398, 1998.

[191] J. H. Casseday and E. Covey. A neuroethological theory of the operation of the inferior colliculus. *Brain Behav Evol*, 47(6):311–336, 1996.

[192] M. Davis. The role of the Amygdala in fear and anxiety. *Annu Rev Neurosci*, 15:353–375, 1992.

[193] C. D. Balaban and J. F. Thayer. Neurological bases for balance-anxiety links. *J Anxiety Disord*, 15(1-2):53–79, 2001.

[194] Véronique M P Moers-Hornikx, Johan S H Vles, Sonny K H Tan, Kimberly Cox, Govert Hoogland, W. M Harry Steinbusch, and Yasin Temel. Cerebellar nuclei are activated by high-frequency stimulation of the subthalamic nucleus. *Neurosci Lett*, 2011.

[195] V. M. P. Moers-Hornikx, J. S. H. Vles, L. W. Lim, M. Ayyildiz, S. Kaplan, A. W. D. Gavilanes, G. Hoogland, H. W. M. Steinbusch, and Y. Temel. Periaqueductal grey stimulation induced panic-like behaviour is accompanied by deactivation of the deep cerebellar nuclei. *Cerebellum*, 10(1):61–69, 2011.

[196] A.B.M.A. Asad, S.Y. Tong, M. Wei, W. Han, and K.H. Chuang. Mapping CNS Response to Leptin by MEMRI. In *Proc. Intl. Soc. Mag. Reson. Med.*, 2011.

[197] F.R. Sharp, S.M. Sagar, K. Hicks, D. Lowenstein, and K. Hisanaga. c-fos mRNA, Fos, and Fos-related antigen induction by hypertonic saline and stress. *J Neurosci*, 11:2321, 1991.

[198] S. Canals, M. Beyerlein, A.L. Keller, Y. Murayama, and N.K. Logothetis. Magnetic resonance imaging of cortical connectivity in vivo. *Neuroimage*, 40(2):458–472, 2008.

[199] T. Watanabe, J. Frahm, and T. Michaelis. Functional mapping of neural pathways in rodent brain in vivo using manganese-enhanced three-dimensional magnetic resonance imaging. *NMR Biomed*, 17(8):554–568, 2004.

[200] D. N. Guilfoyle, V. V. Dyakin, J. O'Shea, G. S. Pell, and J. A. Helpern. Quantitative measurements of proton spin-lattice (T1) and spin-spin (T2) relaxation times in the mouse brain at 7.0 T. *Magn Reson Med*, 49(3):576–580, 2003.

Acknowledgements

Having completed this dissertation, I am deeply indebted to many people.

First, I would like to thank Dr. Michael Czisch, for giving me the opportunity to pursue an exciting and highly rewarding research topic in such a fruitful environment. You have always been a source of moral and scientific support throughout these years. Your extraordinary mentoring helped me to deal with the efforts and frustrations of scientific research.

I am also very grateful for the enormous support and mentoring from my thesis committee. Prof. Dr. Ziegler has guided me through the years of my Ph.D and offered precious advice on how to cope with the ups and downs of scientific research. Prof. Dr. Claus Zimmer always supported me and showed great interest in my work. PD Dr. Carsten Wotjak has guided me through these years as a mentor and always was an inspiration with his great enthusiasm and love for science. Thanks for all the support and interest in my work.

Further, special thanks belong to Sebastian Kaltwasser and Benedikt Bedenk, my officemates who became real friends. Thanks for being there whenever I needed you.

Furthermore I would like to thank the whole NMR research group. Victor and Philipp, thanks for trying to illuminate the statistical universe to me. AC, thanks for your patience in the search for errors in programs. Sara, Katia, Lisa, Martin, Roberto, Manuel, Boris, Brice, thanks for all your support and

the time spent during lunch and cakes. It is a very fortunate situation when one's colleagues are also one's friends.
Further thanks go the technical stuff of the NMR research group, Rosa, Reinhold, Elke, Ines, and Armin, who where always up for a chat.

Additionally, I would like to thank Caitlin Riebe, Katrin Henes, Jan Deussing, Claudia Kühne, Markus Nussbaumer, Prof. Dr. Rainer Landgraf, Mathias Schmidt, Bianca Mayer, Yorick Peterse and Youri Bicker for all their help and support during the years.

I also would like to thank the director of the MPI, Prof. Florian Holsboer, who gave me the opportunity to work at such a great institute.

Further, I want to thank my partner and best friend Matthias, thanks for always making me laugh when I was stressed and all your love and support.

I also want to thank my family. First of all my brothers Gregor, Matthias and Michael for being the best brothers in the world. Further I would like to thank my grandparents, Rita and Alfred, for their interest in my work and my progress.

Finally, no words can describe my gratitude towards my parents, Gerlinde and Wolfgang, without whom I would not be here. Thanks for always being there without questioning, your loving support and unconditional love.